NASA Contractor Report 156846

An Investigation of the Observability of Ocean-Surface Parameters Using GEOS-3 Backscatter Data

L.S. Miller and R.W. Priester

October 1978

NASA
National Aeronautics and Space Administration

Wallops Flight Center
Wallops Island, Virginia 23337
AC 804 824-3411

NASA Contractor Report 156846

An Investigation of the Observability of Ocean-Surface Parameters Using GEOS-3 Backscatter Data

L.S. Miller and R.W. Priester
Applied Science Associates, Inc.
105 East Chatham St.
Apex, NC 27502

Prepared Under Contract No. NAS6-2621

National Aeronautics and
Space Administration

Wallops Flight Center
Wallops Island, Virginia 23337
AC 804 824-3411

TABLE OF CONTENTS

TABLE OF CONTENTS (Cont'd.)

1.0 INTRODUCTION AND SUMMARY OF RESULTS

This report presents summaries of the analytical efforts and system studies conducted under Contract No. NAS6-2621, in connection with the GEOS-3 radar altimeter program. The main investigative areas reported herein are in sea state estimation and data processing related topics.

Section 2.0 discusses significant waveheight ($H_{1/3}$) estimation and the deconvolution of the waveheight probability density function (PDF). The algorithm presented herein differs from other estimators known to the writer in that the waveheight probability density function is not constrained to be a Gaussian. The algorithm shows good agreement with other $H_{1/3}$ algorithms, however, the ensuing density functions are at times found to be highly non-Gaussian. This result applies both to use of the standard GEOS-3 waveform data and use of time-realigned waveform data. The departures from Gaussanity are generally of the bimodal nature and, as such, cannot be adequately characterized by terms such as skewness or kurtosis. The bimodality resembles the theoretical solution given by Longuet-Higgins for a long-crested sea.

Section 3.0 examines the general problem of significant waveheight estimation and presents an analysis of the resolution available from any (unbiased) risetime-based estimator. This analysis shows the $H_{1/3}$ algorithm presented here and the one currently in use at Wallops Flight Center (WFC) provide performance which is close to the theoretical resolution limit. The principal inference of this result is that a sophisticated (waveform based) $H_{1/3}$ estimator does not exist which will yield significant improvement in resolution over the algorithm presently in use at WFC (developed by Hayne). This analysis also quantifies the increase in performance achievable with the WFC estimator when it is coupled with the time-realignment technique developed by Walsh. It should be emphasized that the performance analysis given in

Section 3.0 pertains to estimators based on changes in the leading edge of the waveform as a function of sea state. The $H_{1/3}$ performance analysis work given in Section 3.0 also leads to the development of a totally different, low waveheight, estimator termed the variance-based $H_{1/3}$ algorithm. This estimator is felt to offer potentially higher resolution in the low waveheight range compared to other waveform estimators since use of the variance behavior of the $H_{1/3}$ estimates introduces an additional modeling element into the problem. This estimator is presently being compared with buoy data - the results will be given in a later report. Appendix B contains information on another $H_{1/3}$ estimator which was investigated. In it, the autocovariance of the waveform plateau region was used as a wave-height sensitive parameter. The results were negative in that the covariance was found to be only weakly sensitive to sea-state changes.

Section 4.0 presents a discussion of GEOS-3 backscatter data for periods in which the radar cross-section (σ°) appears to increase markedly. These periods were observed early in the GEOS-3 program and were initially thought to be due to anomalous scattering conditions. Comparisons of theoretical and measured σ° values indicate that these periods represent relatively calm or swell-dominated sea conditions. This section also discusses the data periods in which <u>increases</u> in the attitude/specular gate have been observed. These increased values are shown to be due to ocean surface inhomogeneities. Comparisons between published σ° and those derived from the two available AGC calibrations are given. These comparisons show the "clutter" calibrations to be in considerably better agreement with published and theoretical values.

Section 5.0 covers work relating to system and data processing considerations. The items discussed comprise altitude data editing, sea state altitude bias effects, precipitation sensitivity of the radar altimeter, waveform sampler corrections, and tracking jitter correlation properties.

2.0 ESTIMATION OF SIGNIFICANT WAVEHEIGHT AND DECONVOLUTION OF THE WAVE-HEIGHT DENSITY FUNCTION

The GEOS-3 average backscattered waveform can be modeled as a repeated convolution of three functions, two of which describe the ocean surface features with the third representing altimeter effects. In mathematical form, the preceding may be written as follows:

$$y(t) = h(t)*p(t)*f(t) \tag{1}$$

where

- $y(t)$ represents the GEOS-3 average return waveform,
- $h(t)$ stands for the ocean surface roughness function,
- $p(t)$ is a function which incorporates altimeter waveshape and tracking jitter effects on the return waveform, here called point target response,
- $f(t)$ represents the ocean flat surface function,

and $*$ denotes convolution.

Combining $p(t)*f(t)$ into the single function $u(t)$ leads to the expression

$$y(t) = h(t)*u(t) \tag{2}$$

Given $y(t)$ and a model for $u(t)$, the problem is to estimate $h(t)$, the sea surface roughness function, by performing the deconvolution specified by equation (2). Determination of $h(t)$ is encumbered by the fact that $y(t)$ is available only in terms of sixteen noise-perturbed samples with nominal 6.25 nano sec. spacing and because $u(t)$ is not precisely known. Given the surface roughness function $h(t)$ it is possible to deduce significant waveheight, $H_{1/3}$, by interpreting $h(t)$ as a surface roughness probability density function.

An attempt has been made to formulate and solve this problem in a general manner. To this end the following developmental guide lines were followed:

(a) Points in time at which y(t) is sampled are not constrained

(b) The only restriction placed upon h(t) is that its Laplace transform, H(s), be rational in s.

In the sequel the following steps will be taken so that, using the model defined by equation (2), h(t) may be determined from experimental data:

(a) Apply the Laplace transformation to equation (2) and linearize the resulting expression using quasilinearization.

(b) Inverse transform the linearized model and discretize the resulting time-domain equation in order to account for the sampled nature of the problem.

(c) Develop equations which enable specification of the constants in the rational function H(s) from measurements of $y(t_k)$.

(d) Utilize h(t) to compute significant waveheight.

2.1 Linear System Model and Algorithm for Determination of h(t)

As already mentioned it is necessary to approximate u(t) which is used to model the effects of the GEOS-3 altimeter point target response and the ocean flat surface function. In the present study, the ocean flat surface function is represented by a unit step function with transition at the time origin. On the other hand, the GEOS-3 altimeter point target response, which has, roughly speaking, a Gaussian shape, is approximated with a truncated, raised cosine function. Thus

$$U(s) = L[u(t)]$$

$$= \frac{1}{s} \cdot \frac{1}{2T} \left[\frac{1}{s} - \frac{s}{s^2+\omega^2} \right] \left[1 - e^{-s2T} \right] \qquad (3)$$

where

$$\omega = \frac{\pi}{T}$$

T = one half the pulse width of the altimeter point target function

$\frac{1}{s}$ represents the transform of the ocean flat surface response function, and

$$\left[\frac{1}{2T} \quad \frac{1}{s} - \frac{s}{s^2+\omega^2}\right]\left[1 - e^{-s2T}\right]$$

is the transform of the point target function approximation. The general shape of u(t) is illustrated in Figure 2.1. In equation (3), T is selected so as to reflect the entire altimeter point target response function, including jitter, according to the expression

$$\sigma_{pt} = 0.362\,T$$

where σ_{pt} is the standard deviation of the altimeter point target function.

Taking the transform of equation (2), the time-continuous GEOS-3 return waveform can be expressed as

$$Y(s) = H(s)\,U(s)$$
$$= (N(s)/D(s))\,U(s) \qquad (4)$$

where $N(s) = a_o s^n + a_1 s^{n-1} + \ldots + a_n$

$$D(s) = s^n + b_1 s^{n-1} + \ldots + b_n \quad .$$

The problem is to determine $\{a_j, b_j\}$. In order to obtain a computational algorithm for solution of this problem, it is convenient to convert the highly nonlinear form represented by equation (4) into an iterative linear problem.

Applying quasilinearization [1], a Taylor-series-like functional expansion, to equation (4) results in the following relation

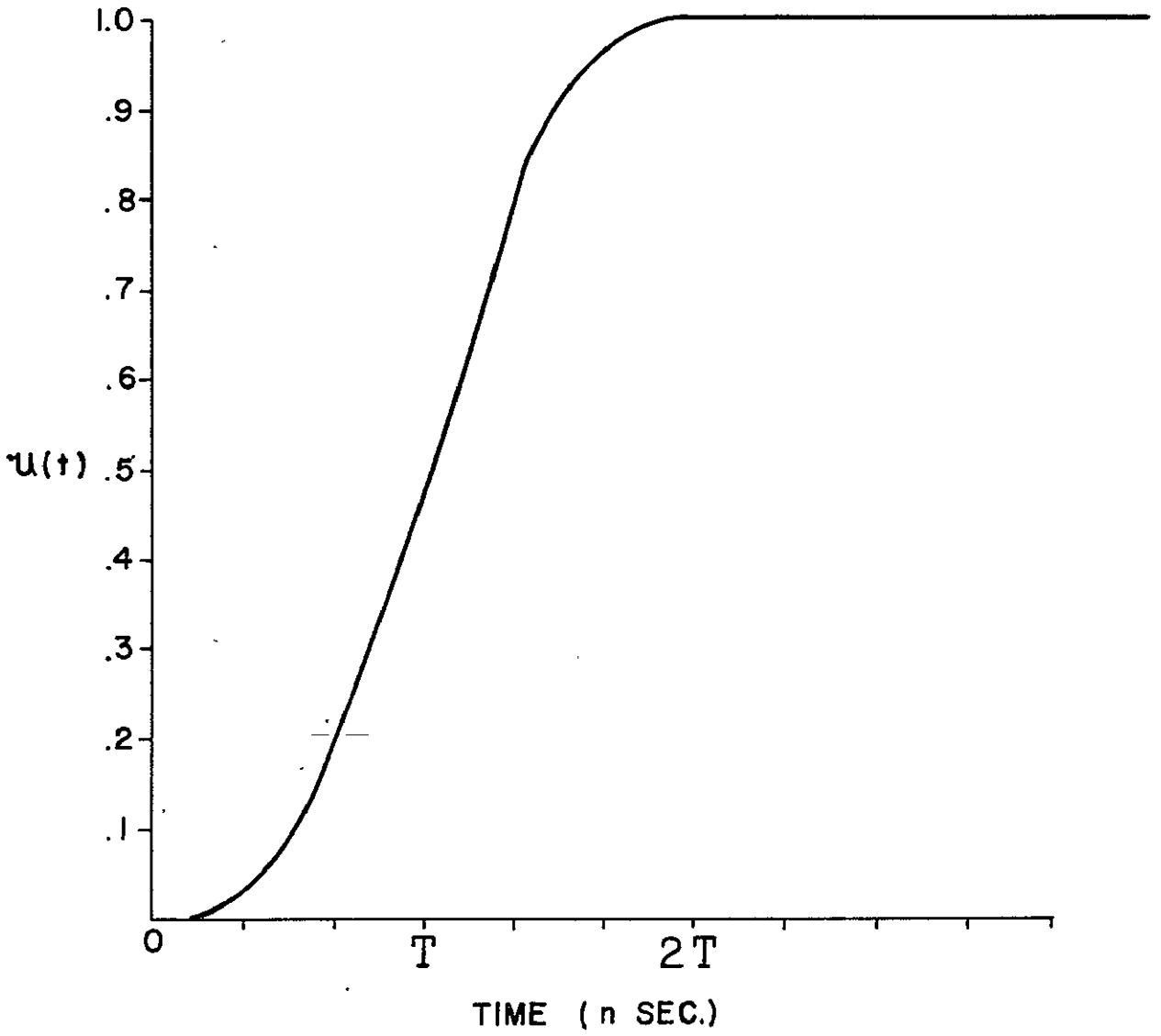

Figure 2.1. Illustration of general shape of system model input function.

$$Y_m^{i+1}(s) = Y_m^i(s) + (N^{i+1}(s)/D^i(s))\ U(s) - (D^{i+1}(s)/D^i(s))\ Y_m^i(s) \qquad (5)$$

where

$$N^i(s) = a_1^i s^{n-1} + a_2^i s^{n-2} + \ldots + a_n^i$$

$$D^i(s) = s^n + b_1^i s^{n-1} + \ldots + b_n^i$$

$Y_m^i(s)$ = model of GEOS-3 average return waveform determined for $i^{\underline{th}}$ iteration

i = iteration number = 0,1,2,...

As shown in reference [2], the model response function $Y_m^{i+1}(s)$ can be expressed in the time domain, using vector-matrix notation. For example, applying the referenced procedure to equation (4) leads to the following result

$$\left.\begin{aligned} \dot{x}(t) &= Ax(t) + Bu(t) \\ y(t) &= P_p x(t) + a_o u(t) \end{aligned}\right\} \qquad (6)$$

where

$$A = \begin{bmatrix} 0 & \vdots & I_{n-1} \\ \cdots & \vdots & \cdots \\ -b_n & \vdots & -b_{n-1} \ \ldots \ -b_1 \end{bmatrix}$$

$$B = (0,0,\ldots,1)'$$

$$P_p = \left[(a_n - b_n a_o), (a_{n-1} - b_{n-1} a_o), \ldots, (a_1 - b_1 a_o)\right]$$

I_{n-1} = $(n-1)x(n-1)$ identity matrix

$\dot{x}(t)$ = time derivative of system state vector,

and prime denotes matrix transposition.

In developing equation (6) from equation (4), initial conditions are assumed to be zero. Applying to equation (5) the above procedure which led to

equation (6) results in the following representation of model output:

$$y_m^{i+1}(t) = x_I'(t)\, P_a^{i+1} + x_{II}'(t)\, P_b^{i+1} - x_{II}'(t)\, P_b^{i} \qquad (7)$$

with $P_a^{i+1} = (a_n^{i+1}, a_{n-1}^{i+1}, \ldots, a_1^{i+1})'$

$P_b^{i+1} = (-b_n^{i+1}, -b_{n-1}^{i+1}, \ldots, -b_1^{i+1})'$

$x_I(t)$ = state vector corresponding to $H_I(s) = N^{i+1}(s)/D^i(s)$

$x_{II}(t)$ = state vector corresponding to $H_{II}(s) = D^{i+1}(s)/D^i(s)$

Denoting the average observed (i.e. experimental) GEOS-3 return waveform by $y_o(t)$, the error between model and observation can be written as

$$\varepsilon^{i+1}(t) = y_o(t) - y_m^{i+1}(t) \qquad (8)$$

which can be interpreted as shown in Figure 2.2. From the figure it is noted that $H_I(s)$, corresponding to $x_I(t)$, is forced by $U(s)$ while $H_{II}(s)$, corresponding to $x_{II}(t)$, is forced by $Y_m^i(s)$. Selecting an index of performance for objectively evaluating the goodness of fit provided by $y_m^{i+1}(t)$ to $y_o(t)$ and solution of the resulting optimization problem enables one to determine the $\{a_j, b_j\}$. In obtaining the solution note that at convergence (i.e. $|\varepsilon^{i+1} - \varepsilon^i| \to 0$) equation (7) reduces to

$$y_m(t) = x_I'(t)\, P_a \quad .$$

Thus at convergence $H_I(s)$ represents the desired system function while the effect of $H_{II}(s)$ vanishes from the model.

Since $y_o(t)$ is known only for $t = t_k$ (k=1,2,...,16), discretization of equations (7) and (8) is required. Thus

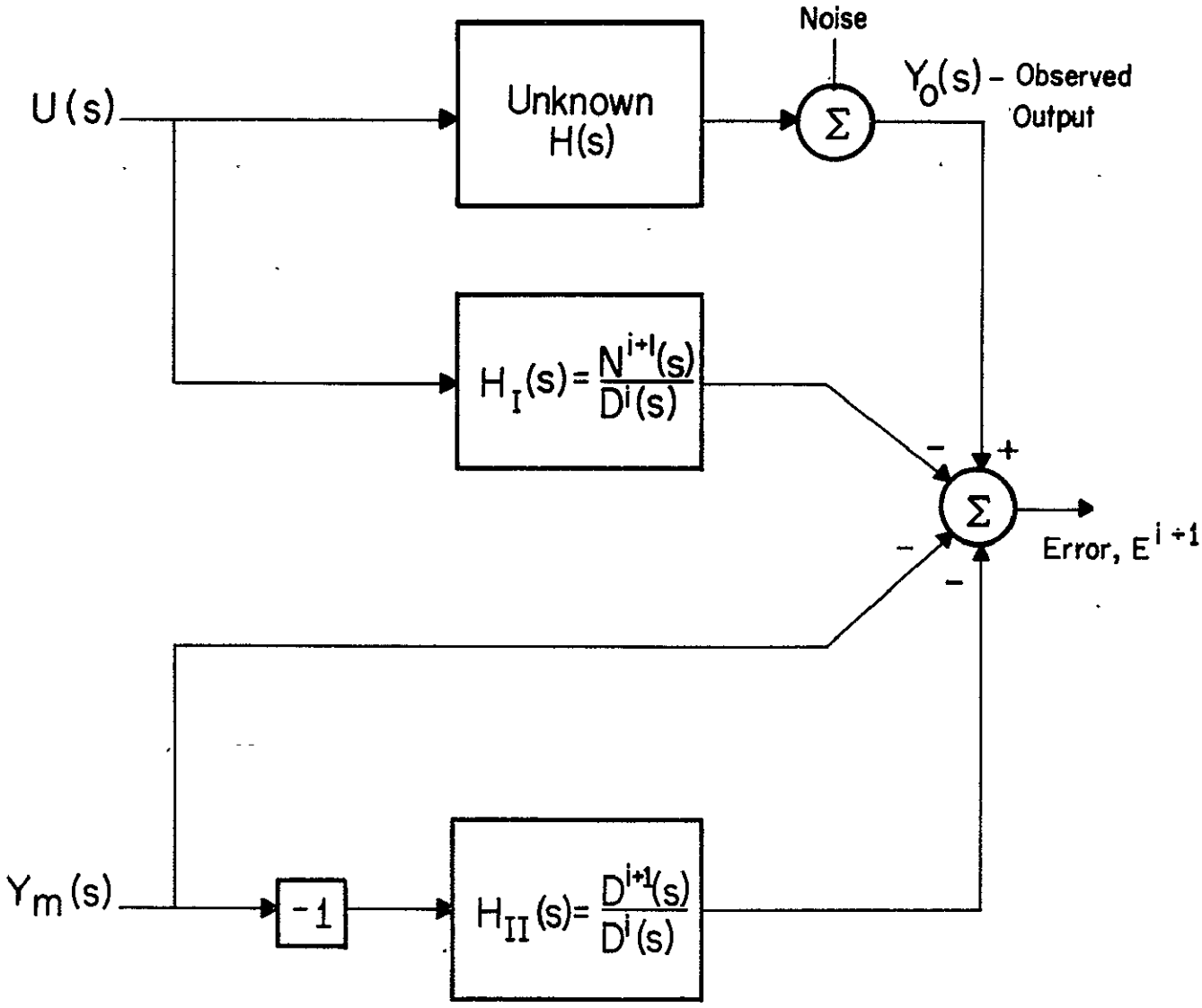

Figure 2.2. Block diagram interpretation of iterative equations.

$$y_m^{i+1}(t_k) = x_I'(t_k)\ P_a^{i+1} + x_{II}'(t_k)\ P_b^{i+1} - x_{II}'(t_k)\ P_b^{i} \quad , \tag{9}$$

$$\varepsilon^{i+1}(t_k) = y_o(t_k) - y_m^{i+1}(t_k) \quad , \tag{10}$$

$$k = 1,2,\ldots,16 \quad .$$

Assuming that u(t) and $y_m^i(t)$ change linearly between t_{k+1} and t_k, it can be shown that $x_I(t_k)$ and $x_{II}(t_k)$ in equation (9) can be written as follows:

$$x_I(t_{k+1}) = \Phi^i(\Delta_k)x_I(t_k) + \Theta^i(\Delta_k)B\ u(t_k) + (A^i)^{-1}\left[\Theta^i(\Delta_k) - \Delta_k I\right]B\ \frac{\left[u(t_{k+1}) - u(t_k)\right]}{\Delta_k} \tag{11}$$

$$x_{II}(t_{k+1}) = \Phi^i(\Delta_k)x_{II}(t_k) + \Theta^i(\Delta_k)B\ y_m(t_k) + (A^i)^{-1}\left[\Theta^i(\Delta_k) - \Delta_k I\right]B\frac{\left[y_m^i(t_{k+1}) - y_m(t_k)\right]}{\Delta_k} \tag{12}$$

where

$$\Delta_k = t_{k+1} - t_k$$

$\Phi^i(\Delta_k)$ = state transition matrix corresponding to

$$H_I(s) = N^{i+1}(s)/D^i(s)$$

$$\Theta^i(\Delta_k) = (A^i)^{-1}\left[\Phi^i(\Delta_k) - I_n\right]$$

$$A^i = \begin{bmatrix} 0 & \vdots & I_{n-1} \\ \cdots & \vdots & \cdots \\ -b_n^i & \vdots & -b_{n-1}^i \ \cdots\ -b_1^i \end{bmatrix}$$

and B is as previously defined. Note that the assumption of linear variation of $y_m(t)$ between t_{k+1} and t_k, while it might affect convergence rate will not influence the approximation of $y_o(t)$.

Combining equations (9) and (10) results in the vector error expression

$$\varepsilon^{i+1} = Y_o - \bar{X} P^{i+1} \tag{13}$$

where

$$\bar{X} = \begin{bmatrix} x_I'(t_1) & x_{II}'(t_1) \\ \vdots & \vdots \\ x_I'(t_{16}) & x_{II}'(t_{16}) \end{bmatrix}$$

$$Y_o = \begin{bmatrix} y_o(t_1) + x_{II}'(t_1) P_b^i \\ \vdots \\ y_o(t_{16}) + x_{II}'(16) P_b^i \end{bmatrix}$$

$$P^{i+1} = \begin{bmatrix} P_a^{i+1} \\ - - \\ P_b^{i+1} \end{bmatrix}$$

and ε^{i+1} is a column vector of errors between observation and model.

Selecting the performance index as minimization of the sum squared error, $(\varepsilon^{i+1})' \cdot \varepsilon^{i+1}$, results in the parameter estimate

$$\hat{P}^{i+1} = (\bar{X}'\bar{X})^{-1}\bar{X}' Y_o \tag{14}$$

where $\hat{P}^{i+1} = \begin{bmatrix} \hat{P}_a^{i+1} \\ - \\ P_b^{i+1} \end{bmatrix}$

Given initial values for $\{b_j^o\}$, it is feasible to evaluate equations (9) and (10), using (11) and (12), and to update the starting estimate of the unknown parameter vector, $\hat{P}^i$, by evaluating equation (14).

The computational algorithm for evaluating equation (14) can be initialized by specifying $\{b_j^o\}$ and $y_m^o(t_k)$ or, equivalently, by specifying $\{a_j^o, b_j^o\}$. The initialization procedure that was used to compute the results presented in paragraph 2.4 consists of setting $\{b_j^o\}$ equal to coefficients which define the all pole maximally flat, unit delay approximation discussed in [3]. Also since $y_m^{i+1}(t_k)$ must approximate $y_o(t_k)$, the iterations are started under the conditions $y_m^i(t_k) = y_o(t_k)$ until the computation stabilizes at which time use of $y_m^i(t_k)$ can be made for the (i+1)th iteration. Stopping criteria for the algorithm described above are readily formulated. A simple stopping criteria would be

$$\left|(\varepsilon^{i+1})'\varepsilon^{i+1} - (\varepsilon^{i})'\varepsilon^{i}\right| \begin{cases} > \delta \text{ , continue} \\ \leq \delta \text{ , stop iterations} \end{cases}$$

where δ is an appropriately chosen small positive number.

2.2 Alternate Interpretation of Model

By manipulating equation (3) the model developed in paragraph 2.1 can be modified such that ideal altimeters (i.e. point target response equal to the Dirac delta function) may be represented. Consider the limit of equation (3) as $T \to 0$, i.e.

$$U_I(s) = \lim_{T \to 0} U(s)$$

$$= \frac{1}{s} \quad . \tag{15}$$

Therefore, all of the equations developed in paragraph 2.1 apply to the present situation provided

$$u(t) = \mu(t) \quad ,$$

that is, $u(t)$ is set equal to the unit step function $\mu(t)$. This form of the model has been used and results from its application will be presented in paragraph 2.4.

Another interpretation results upon combining equations (3) and (4) to write

$$Y(s) = H(s)\,\frac{1}{2Ts}\left[\frac{1}{s} - \frac{s}{s^2+\omega^2}\right]\left[1 - e^{-s2T}\right]$$

Assuming zero initial conditions

$$\frac{dy(t)}{dt} = L^{1}\left[sY(s)\right]$$

$$= L^{-1}\left\{\frac{H(s)}{2T}\left[\frac{1}{s} - \frac{s}{s^2+\omega 2}\right]\right\}$$

$$- L^{-1}\left\{\frac{H(s)}{2T}\left[\frac{1}{s} - \frac{s}{s^2+\omega^2}\right]\right\}\mu(t-2T)$$

By normalizing dy(t)/dt such that the curve defines unit area, this result can be interpreted as the surface roughness probability density function (it is assumed that y(t) is monotone nondecreasing). A somewhat similar result follows if the altimeter point target response is approximated with a rectangular pulse.

2.3 Analytic Evaluation of Surface Roughness from H(s)

The function h(t) (or $h(t_k)$) can be interpreted as the unnormalized surface roughness density function. Define

$$\hat{h}(t) = \frac{1}{a}\,h(t)$$

where

$$a = \int_0^{Tg} h(t)dt$$

and Tg is the time expanse of the GEOS-3 waveform sampling gates. Then

$$\sigma^2 = m_2 - m_1^2 \qquad (16)$$

where

$$m_k = \frac{1}{a} \int_0^{Tg} t^k \, h(t)dt$$

In the context of paragraph 1.1

$$m_2 = \frac{P'_a A^{-1}}{a} \left\{ \Phi(Tg)Tg^2 - 2TgA^{-1}\Phi(Tg) + 2A^{-1}\Theta(Tg) \right\} B$$

and

$$m_1 = \frac{P'_a A^{-1}}{a} \left\{ \Phi(Tg)Tg - \Theta(Tg) \quad B \right\}$$

2.4 Computer Implementation and Simulated Results

The algorithm for determination of H(s), presented in paragraph 2.1, has been programmed and tested using GEOS-3 frame-averaged gate data. Details relating to use of the computer program are contained in Appendix A . Application to computation of surface roughness density, $\hat{h}(t)$, is the topic considered in paragraph 2.4.1 while its use as an estimator of $H_{1/3}$ is treated in paragraph 2.4.2.

2.4.1 Computation of Surface Roughness Density Function

The algorithm developed in paragraph 2.1 computes $\hat{h}(t)$, the surface roughness density function, given the frame-averaged GEOS sample gate data. This is an inverse problem for which numerical computations can be unstable due to noise and modeling error effects in the solution technique employed. The method used herein avoids explicit numerical deconvolution since $\hat{h}(kT)$, $k = 0,1,2,\ldots,N$, is not computed directly in terms of the measured or experimental data. Rather, $\hat{h}(t)$ is obtained (in terms of a small number of parameters)

by applying system identification techniques.

Typical results obtained from applying the algorithm will be presented at this time. All results shown were obtained with u(t) (see equation (2)) defined as a linear ramp starting from zero at gate one, extending over four gate intervals, and equal to unity thereafter. Figure 2.3 shows the sampling gate waveforms for three consecutive frames of Rev. 6893. In this figure, the vertical scale reflects the measured values of frame 103 and frames 104 and 105 were adjusted such that their normalized response asymptotes (see discussion in Appendix A) were equal to that of frame 103. This enables a relative comparison of the rates at which the three response curves rise. The deconvolved surface roughness probability density functions corresponding to the return waveforms of Figure 2.3 are shown in Figure 2.4. Note that the tendency of frames 104 and 105 to rise early relative to frame 103 is reflected in the probability density curves of Figure 2.4. In particular the two-step shape of frame 105 (Figure 2.3) results in a bimodal density function. The $H_{1/3}$ values shown in Figure 2.4 were computed using Hayne's [4] algorithm. $H_{1/3}$ values computed from the probability density curves shown are placed inside parentheses.

Bimodal densities have been observed in a number of instances for large sea state conditions ($H_{1/3} > 7.0$ meters). It is natural to question whether or not this shape might be due, at least partially, to tracking loop jitter effects. Figures 2.5 and 2.6 present results obtained from processing both time realigned (dashed curves) and unrealigned data (solid curves). In the case of Figure 2.5, time realignment resulted in the attenuation of the tendency toward bimodal behavior. In contrast, however, Figure 2.6 shows that an approximately trapezoidal shape reverts to bimodal nature upon application of time realignment. This result is interesting if it is noted that after time realignment both the shape of the density function and the value of $H_{1/3}$ are

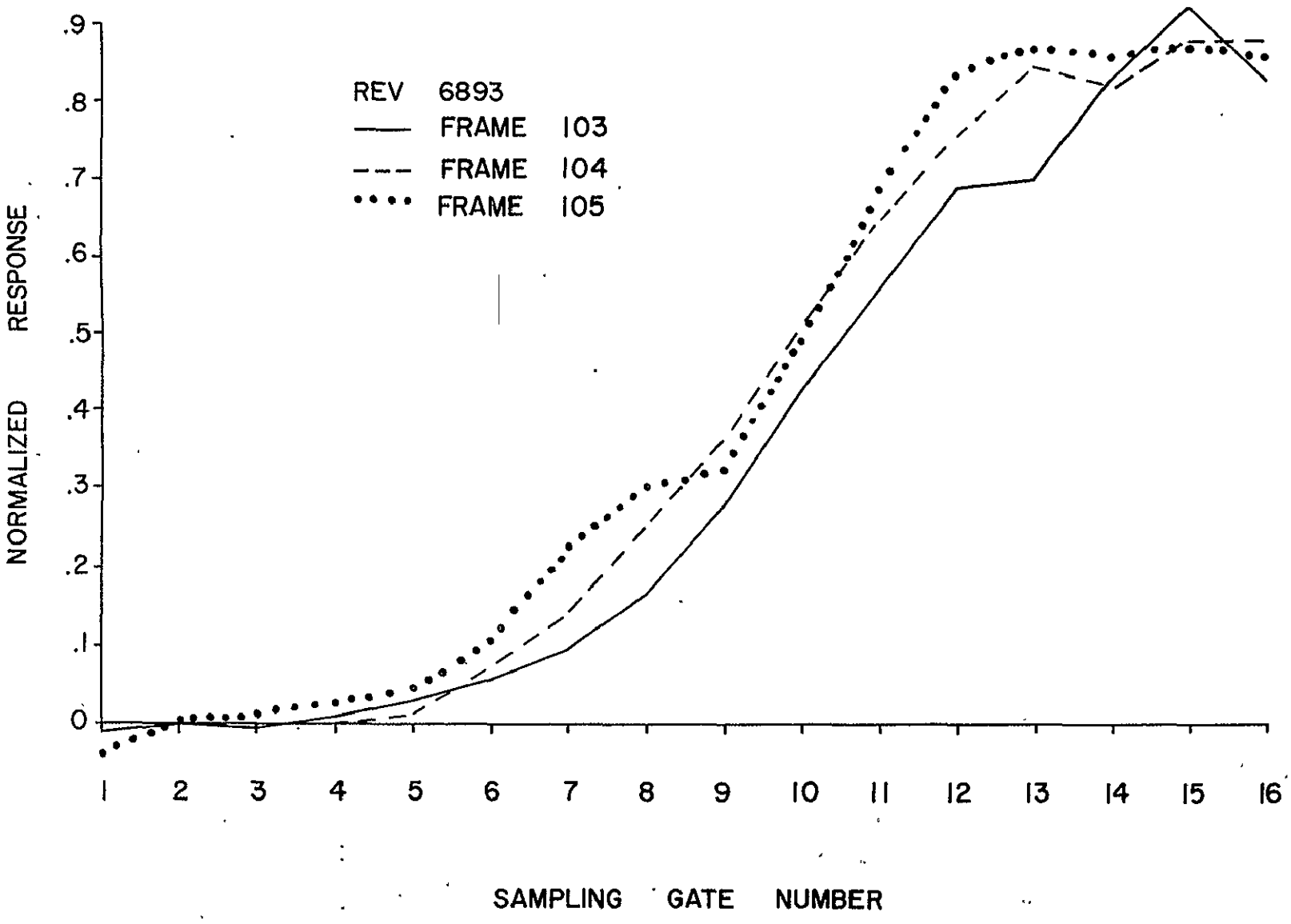

Figure 2.3. GEOS-3 Sample Gate waveforms corresponding to the surface roughness density functions illustrated in Figure 4.

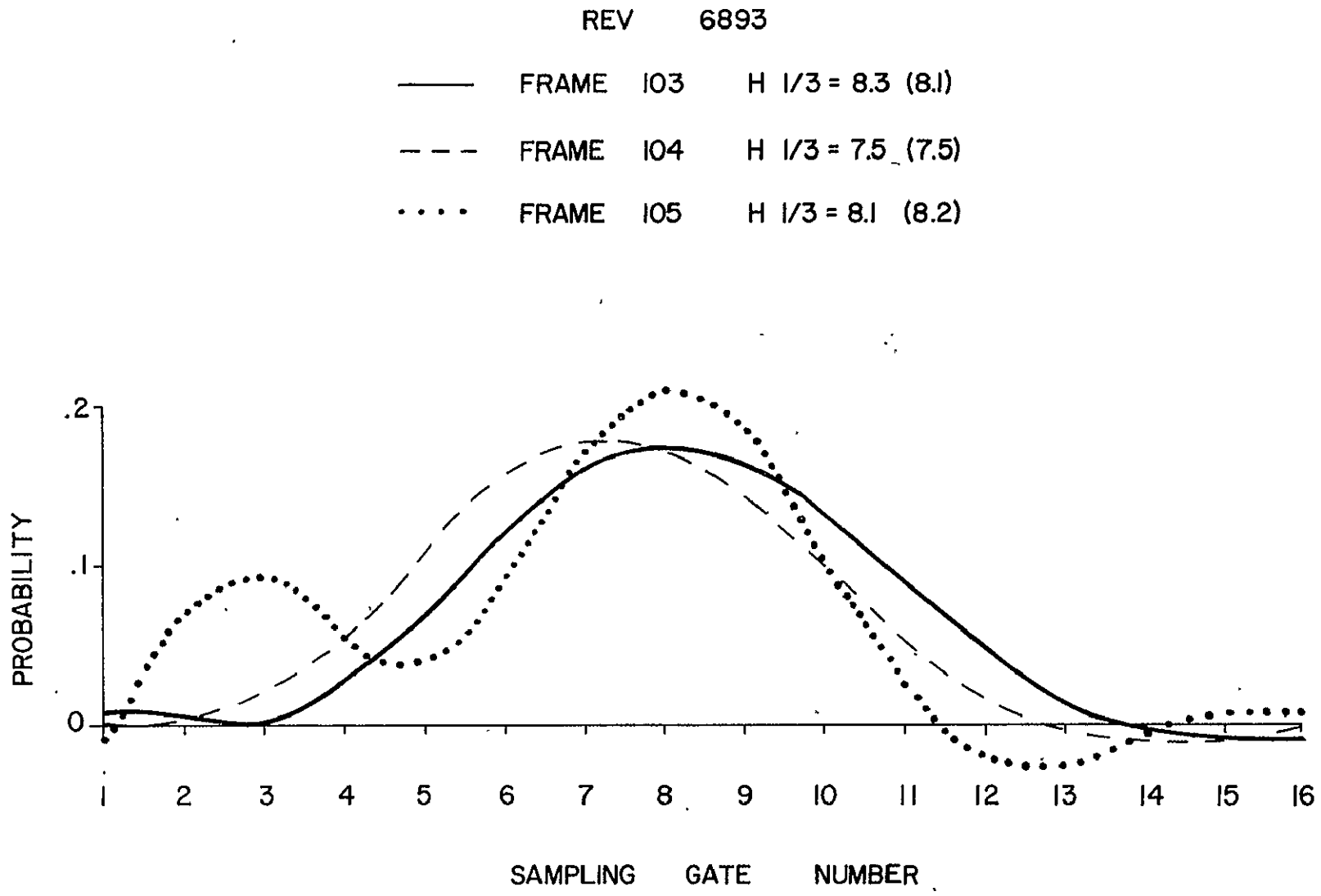

Figure 2.4. Surface roughness density functions corresponding to the waveforms of Figure 4.

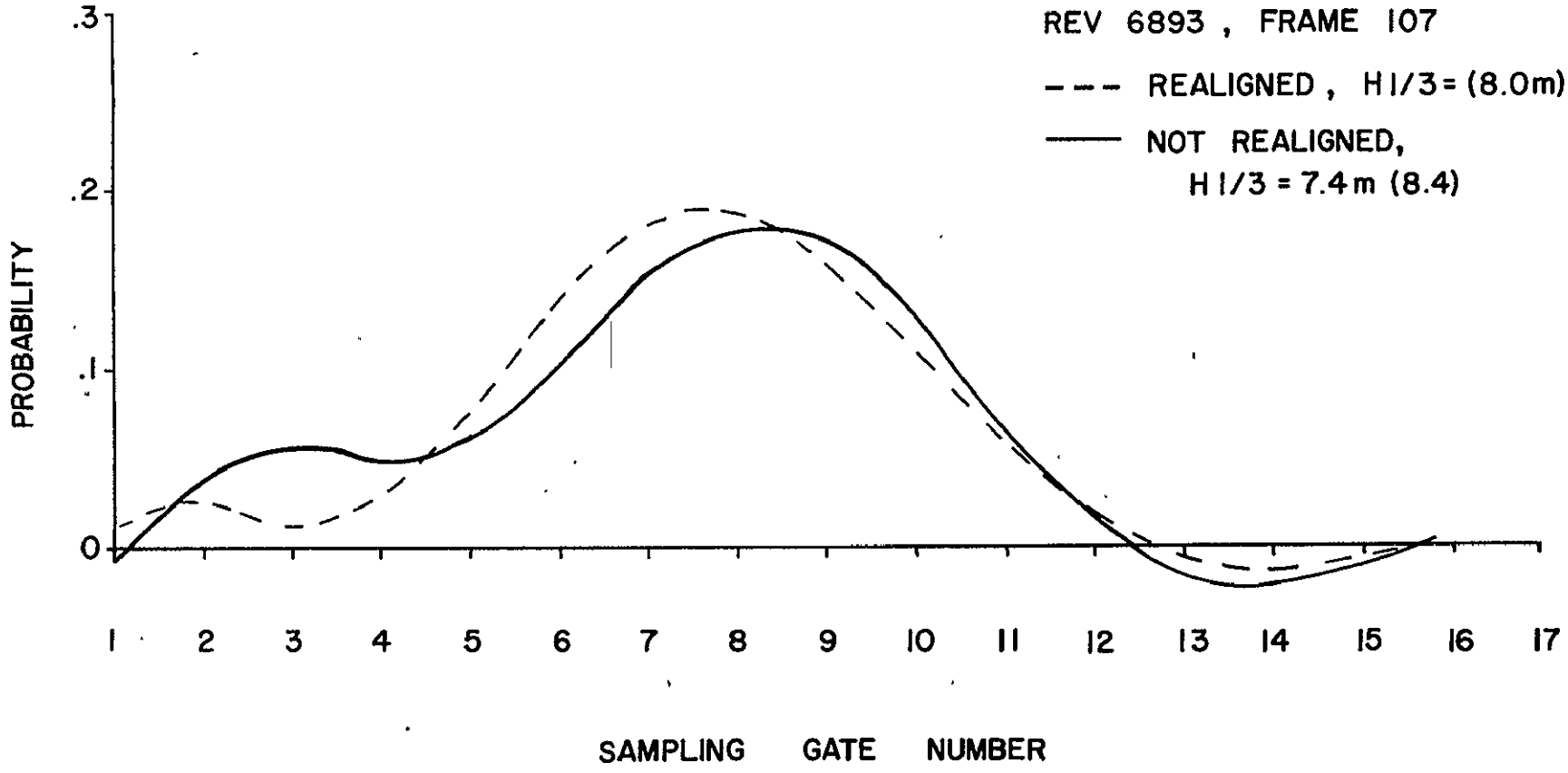

Figure 2.5. An illustration of the effect of time realignment on the surface roughness density function.

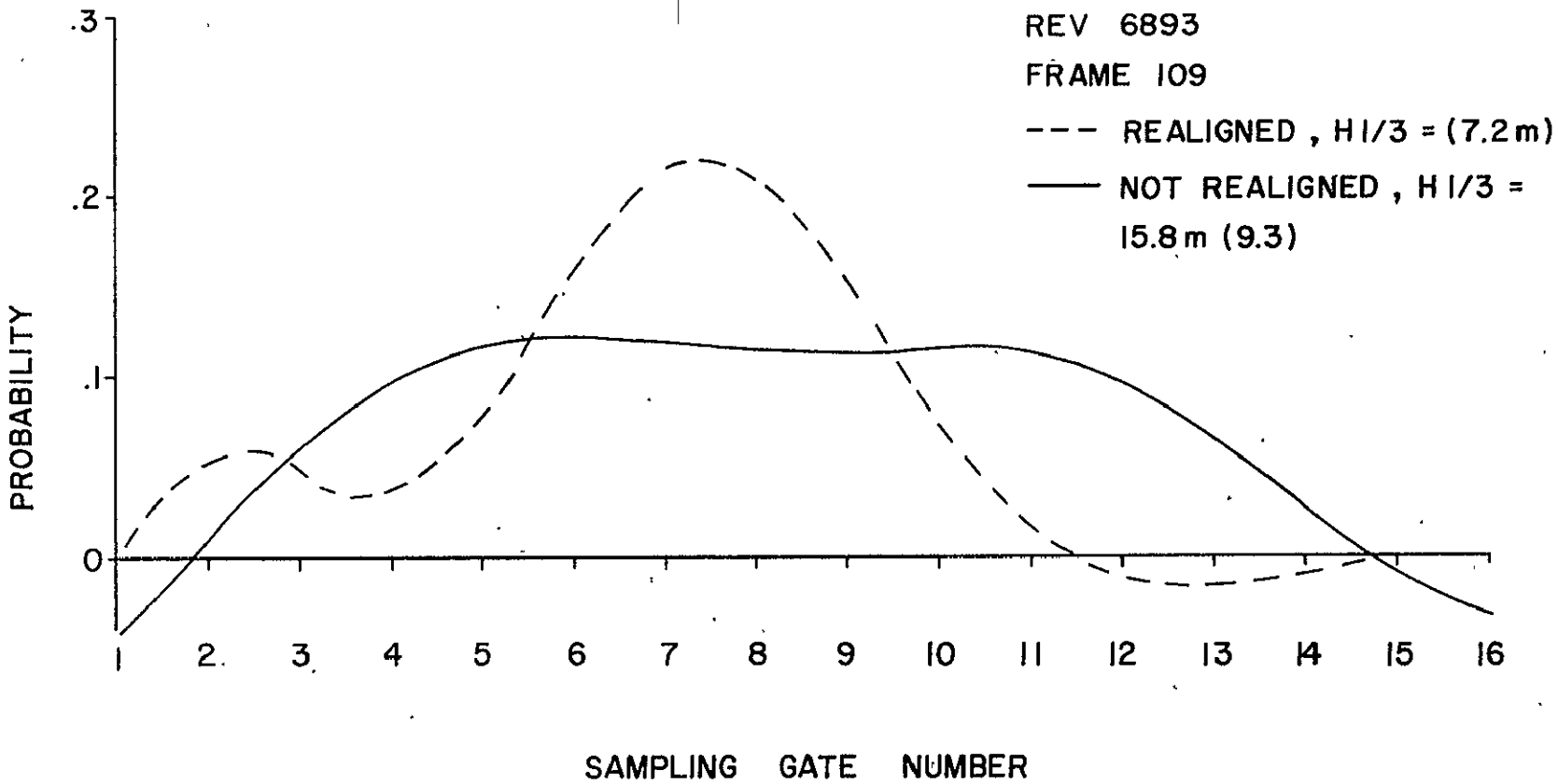

Figure 2.6. An illustration of the effect of time realignment on the surface roughness density function.

more consistent with results from neighboring frame data than is the unrealigned data.

In its present form the algorithm cannot cope with $\hat{h}(t)$ functions encountered when $H_{1/3} < 4.0$ meters. In this range of sea state values $\hat{h}(t)$ begins to approach the Dirac delta function (in the limit as $H_{1/3} \to 0$ it is equal to the delta function) which cannot be approximated by a finite rational function. Figure 2.7 is an illustration of this effect. Note the increased tendency to oscillation displayed by the density function plotted. This behavior is a result of the approximation problem mentioned above.

Another characteristic of the approximation technique is that the shape of $\hat{h}(t)$ is dependent upon the order chosen for the approximating system. For convenience let the respective orders of numerator and denominator polynomials of H(s) be denoted by (m-1,n) where

$$0 \leq m-1 < n$$

$$1 < n \leq 5 \quad .$$

Figure 2.8 illustrates the effect of model order upon the resulting probability function. In this figure, the notation (3,4), (2,3) should be interpreted to mean that the resultant curve was obtained as the arithmetic mean of two identification procedures - one for which H(s) had polynomial orders (3,4) and the other for which the orders were (2,3). The example in Figure 2.8 shows that the average density produced by (3,4),(2,3) is somewhat different from that realized when (2,3),(1,2) is used. All of the curves presented in this section were computed as an average of two model fits to the sampled gates. In all cases, either (3,4),(2,3) or (2,3),(1,2) combinations were used in obtaining $\hat{h}(t)$. Use of the combination (m-1,n) = (4,5) frequently resulted in highly oscillatory $\hat{h}(t)$ and experience indicates that it can only rarely be used.

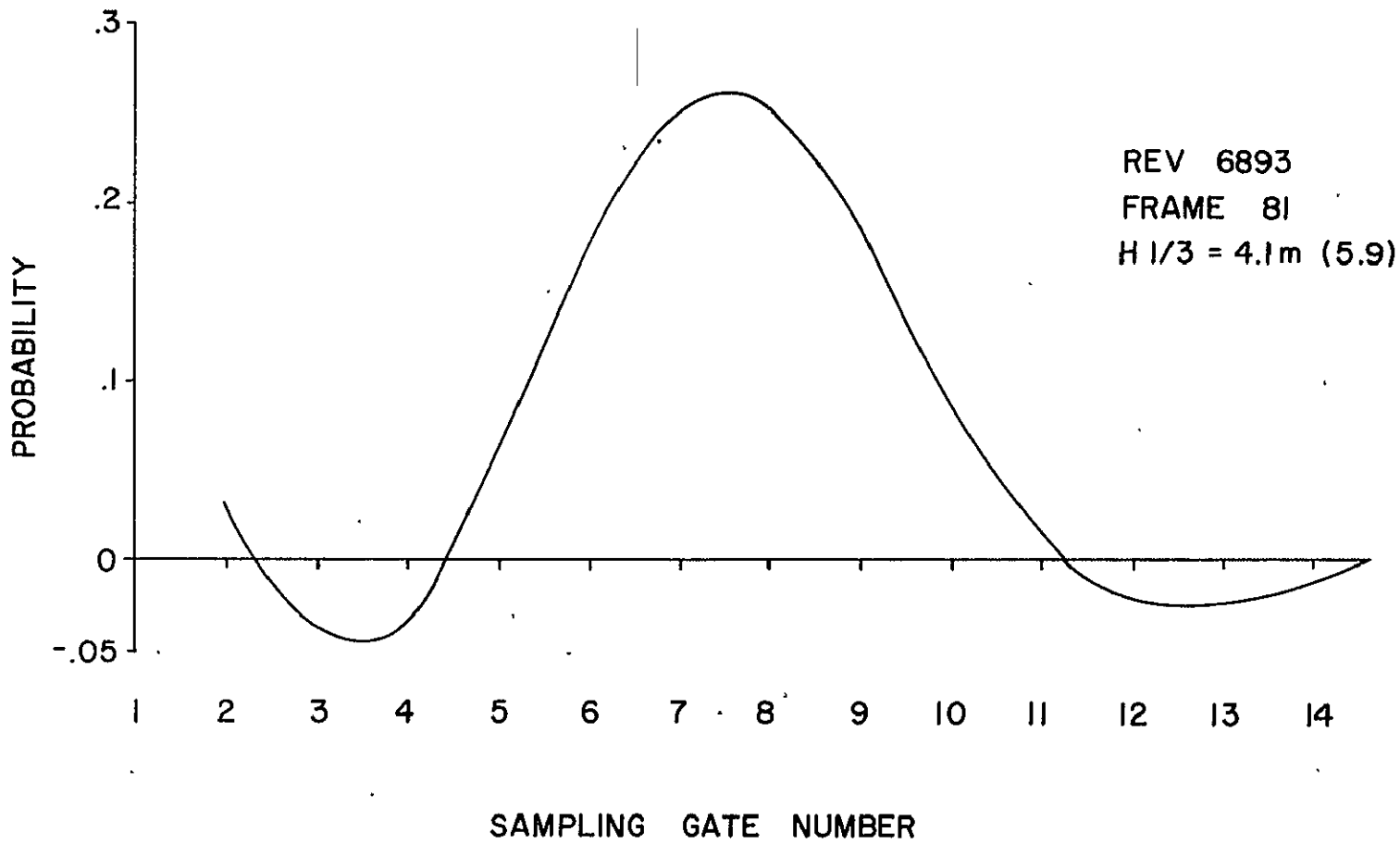

Figure 2.7. Estimated density function for $H_{1/3} \simeq 4.0$ m.

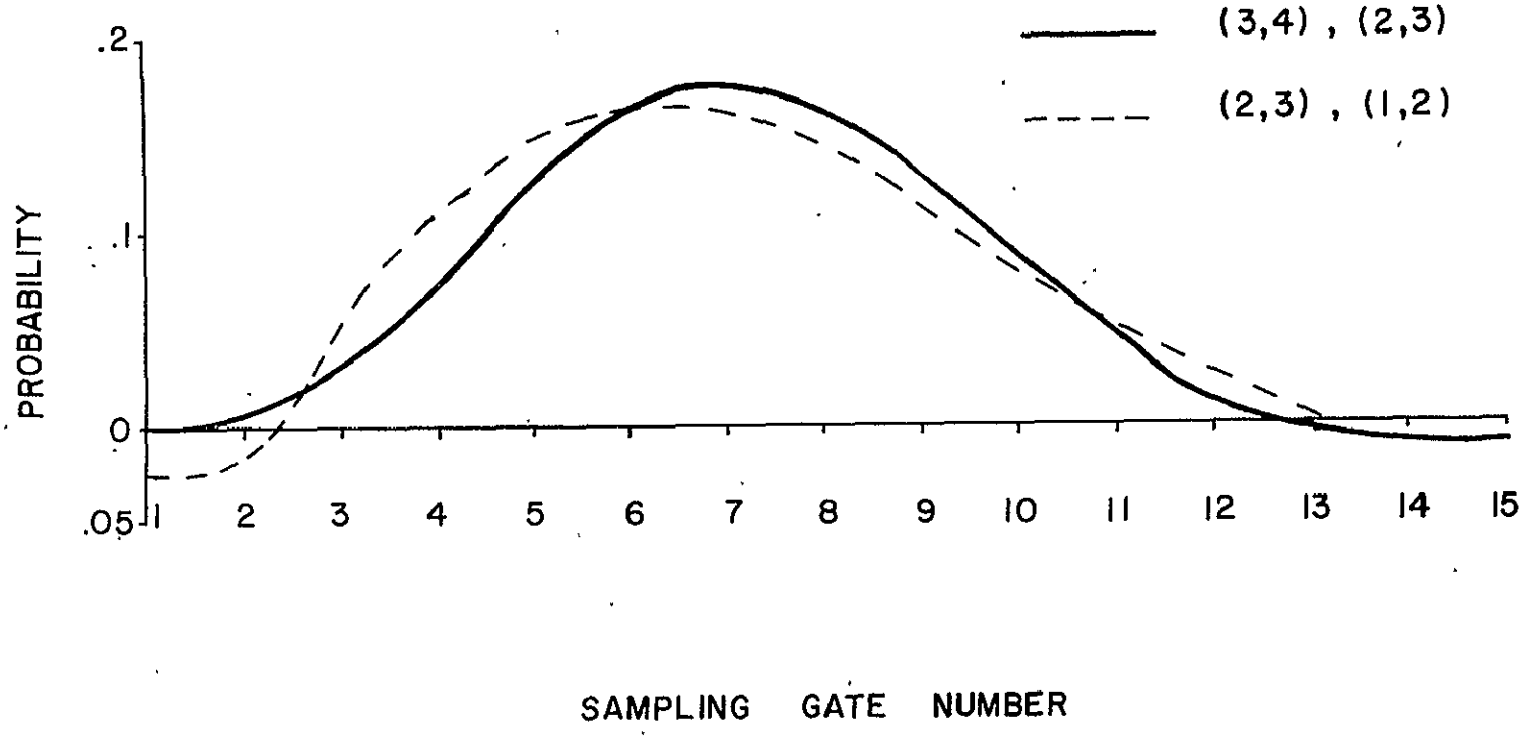

Figure 2.8. Illustration of the effect of model order upon approximation to surface roughness density function.

2.4.2 Estimation of Sea State

The algorithm developed in paragraph 2.1 can, of course, be used to estimate sea state for all values of $H_{1/3}$ if u(t) in equation (2) is made equal to the unit step function. This redefinition of u(t) avoids the approximation problem discussed in paragraph 2.4.1 as $H_{1/3} \to 0$. Therefore, the results presented in this paragraph were obtained under the following assumptions:

(a) u(t) is the unit step function

(b) Only frame averaged (3.2 second average) data is to be processed

(c) (m-1,n) = (2,3) was used in obtaining all results presented.

Given that u(t) is the unit step function in equation (2), $H_{1/3}$ may be computed from the expression

$$H_{1/3} = 0.6 \sqrt{|\sigma^2 - \sigma_{pt}^2|} \cdot \text{Signum}\left(\sigma^2 - \sigma_{pt}^2\right) \qquad (17)$$

where σ^2 is given by equation (16)

and σ_{pt}^2 = altimeter point target function. (including jitter) .

A sample of the computational results obtained from simulations is presented in Figure 2.9 where they have been compared, in the form of a scatter plot, with the results produced by Hayne's algorithm [4]. It is noted from the figure that for $H_{1/3} > 2.5$ meters, the two approaches produce results that are generally in good agreement; however for smaller $H_{1/3}$ the disparity is significant.

2.5 Development of a Constrained Estimator of Significant Waveheight

This paragraph describes a method which provides least square estimates

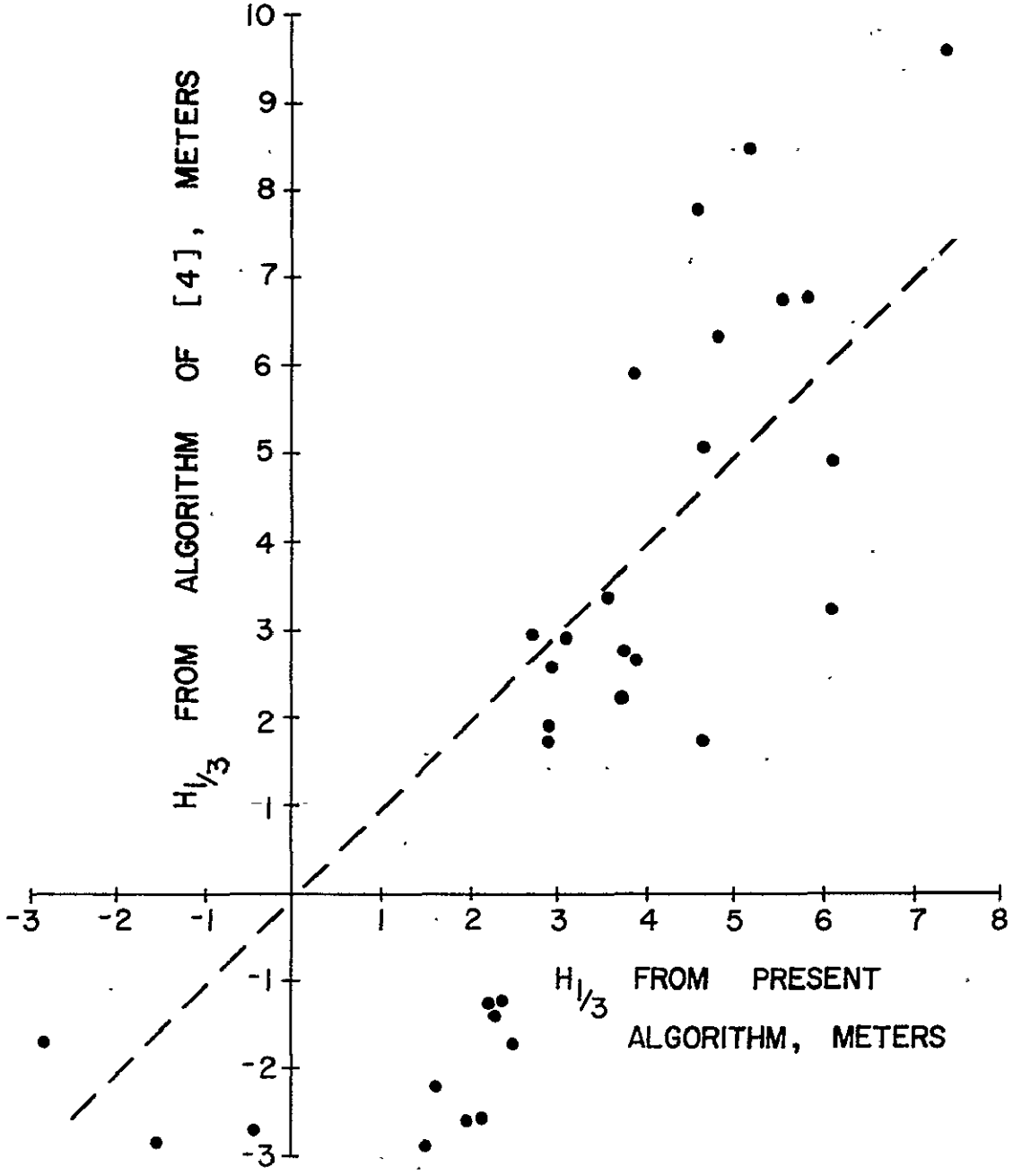

Figure 2.9. Scatter plot comparing present algorithm with that of [4].

of $H_{1/3}$ under the constraint that $H_{1/3} \geq 0$. Development of the algorithm is made under the assumption of Gaussian statistics. Utilizing notation introduced in paragraph 2.1, the model of the GEOS-3 average return waveform can be expressed in transform notation as

$$Y_m(s) = H_n(s)U(s) \tag{18}$$

where

$$H_n(s) = \left(\frac{1 - e^{-s\tau}}{s\tau}\right)^n e^{-sT_o} \qquad \text{by definition,}$$

T_o = a time-domain shift parameter,

τ = parameter related to surface roughness.

Here $H_n(s)$ represents an n^{th} order convolutional approximation to a Gaussian probability density function as discussed in [6] with n=1,2,... . The basic function used in generating the Gaussian density is a uniform density of width τ nano sec. with leading edge displaced T_o from the origin. For U(s) as specified in equation (3) of paragraph 2.1 and with n = 3, the discretized model output in the time domain is given by

$$y_m(t) = \sum_{i=0}^{3} \frac{\mu(z_i)}{2T\tau^3}\left\{\frac{z_i^4}{24} - \frac{1}{\omega^2}\left[\frac{z_i^3}{6} - \frac{1}{\omega^3}(\omega z_i - \operatorname{Sin}\omega z_i)\right]\right\}$$

$$- \sum_{i=1}^{3} \frac{\mu(w_i)}{2T\tau^3}\left\{\frac{w_i^4}{24} - \frac{1}{\omega^2}\left[\frac{w_i^3}{6} - \frac{1}{\omega^3}(\omega w_i - \operatorname{Sin}\omega w_i)\right]\right\} \tag{19}$$

where

$z_i = t - T_o - i\tau$, $t = 0,1,2,\ldots,15$

$w_i = t - 2T - T_o - i\tau$

$\mu(\cdot)$ = unit step function

$\omega = \frac{\pi}{T}$

and T is selected to approximate the altimeter point target response function. Note that in the discretization specified in equation (19) that the time axis is scaled in units of 6.25 nano sec.

Defining the approximation error as

$$\varepsilon^2 = \sum_{t=0}^{15} \left(y_o(t) - y_m(t)\right)^2 \tag{20}$$

the problem is to find T_o^* and τ^* which minimize ε^2 such that $\tau^* \geq 0$.

For this particular formulation it is straightforward to find approximate T_o^* and τ^* by implementing an exhaustive two-parameter search procedure. Given τ^*, the standard deviation of surface roughness can be calculated as

$$\sigma = 6.25\left(\frac{\tau^*}{2}\right) \quad \text{nano sec.}$$

Therefore, significant waveheight is given by

$$H_{1/3} = .6\ \sigma$$

$$= 1.875\ \tau^* \quad \text{meters.}$$

A computer program based upon the procedure described above was written and used to compute $H_{1/3}$ from frame averages of GEOS-3 return waveforms. Before computing τ^*, the return waveform was preprocessed as follows:

$$\bar{y}_o = \left(\sum_{t=0}^{3} y_o(t)\right) / 4$$

$$\bar{\bar{y}}_o = \left(\sum_{t=14}^{16} y_o(t)\right) / 3$$

$$y_o(t) \leftarrow \left[y_o(t) - \bar{y}\right] \Big/ \left[\bar{\bar{y}}_o - \bar{y}_o\right] \qquad t = 0,1,\ldots 15\ .$$

where $\leftarrow$ is used to indicate a redefinition of $y_o(t)$. This preprocessing is performed so that the fitted function approximates a cumulative distribution, but could be avoided by introducing an unknown multiplier into equation (18) and performing a three-parameter search.

Computational results from application of this algorithm are presented in Figure 2.10 which again makes use of results obtained from applying the technique described in [4]. So long as $H_{1/3}$, as computed using the method of [4], is greater than about 2 meters the two results are in general agreement. Again, for $H_{1/3} < 2$ meters the correspondence is not good.

2.6 Summary and Conclusions

The results obtained from application of the algorithms developed herein lead to the conclusion that linear system theory concepts can be successfully applied to significant waveheight estimation. If the estimated sea state exceeds approximately 2.5 meters, both of the algorithms presented herein produce results that are in satisfactory agreement with the method developed by Hayne [4]; however, for $H_{1/3}$ less than 2.5 meters erratic performance of the estimators was noted. It will be shown in Section 3.0 that estimation of sea state for calm sea conditions (i.e. $H_{1/3} \rightarrow 0$) is a very unstable problem for which the variance of any unbiased estimator can be very large, for data rates prescribed by GEOS-3 operational parameters.

Attempts to determine surface roughness probability density functions has been successful provided that the associated $H_{1/3} > 4.0$ m. Since the algorithm can be extended so as to cope with instability encountered as $H_{1/3} \rightarrow 0$, the approach used appears to be capable of describing surface roughness probability density for a wide range of $H_{1/3}$ values.

The algorithm of paragraph 2.1 has been used to compute $H_{1/3}$ and comparison shows good agreement with results obtained from an existing method

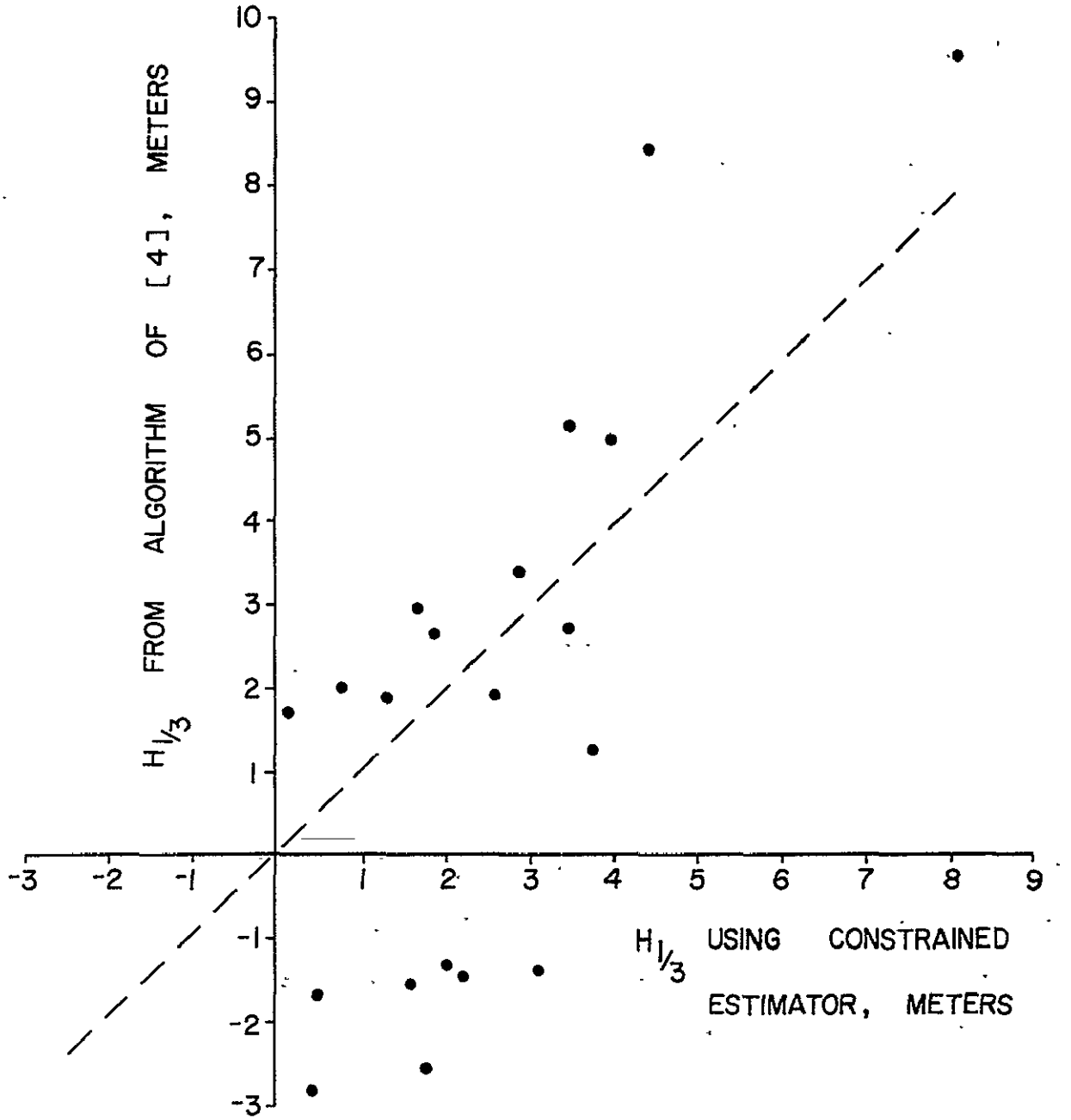

Figure 2.10. Scatter plot comparing constrained estimator with that of [4].

[4] so long as $H_{1/3} > 2.5$ m.

The constrained estimator of paragraph 2.5 performs satisfactorily and is intuitively appealing since negative $H_{1/3}$ is physically meaningless. However, the important question of bias induced by this estimator is a matter of concern. By resorting to Monte Carlo simulations, this question could be resolved but such a study falls outside the scope of the present investigation. This algorithm might be generalized to enable fine structure identification by utilizing the sum of Gaussian-shaped densities. In this more general setting it is doubtful if a multidimensional search approach as employed here would remain a viable computational approach.

REFERENCES

[1] Bellman, R. E.; and Kalaba, R. E.: Quasilinearization and Nonlinear Boundary-Value Problems, American Elsevier Publishing Co., New York, 1965.

[2] Ogata, K.: State Space Analysis of Control Systems, Prentice Hall, 1967.

[3] Van Valkenburg, M. E.: Introduction to Modern Network Synthesis, John Wiley and Sons, 1960.

[4] Hayne, G. S.: Initial Development of a Method of Significant Waveheight Estimation for GEOS-III, NASA CR-141425, August, 1977.

[5] Walsh, E. J.: personal communication.

[6] Papoulis, A.: Probability, Random Variables, and Stochastic Processes, McGraw Hill, pp. 266-268, 1965.

3.0 ASSESSMENT OF PERFORMANCE LIMITATIONS OF GEOS-3 SIGNIFICANT WAVEHEIGHT ESTIMATORS

A number of algorithms have been developed for estimating ocean significant waveheight by analysis of the GEOS-3 altimeter average return waveform. The results of limited comparisons of three such algorithms is presented in Section 2.0 of this report, from which it is concluded that acceptable agreement exists between the algorithms for $H_{1/3}$ greater than about two meters. However, if the estimated $H_{1/3}$ is less than two meters the estimators all show that $H_{1/3}$ resolution degrades rapidly as $H_{1/3} \to 0$ (this result was anticipated by Miller and Brown [1]). The purpose of this report is to evaluate the performance limitations encountered by any estimator of $H_{1/3}$ which uses the GEOS-3 models for average return waveform and noise. The Cramer-Rao inequality will be used to establish estimator performance bounds.

The objective of this study is to determine $H_{1/3}$ estimator performance limitations and to qualitatively assess the degree to which the present GEOS-3 $H_{1/3}$ algorithm [2] approaches the resulting bound. The Cramer-Rao bound is selected for this investigation because (1) compared with other bounds (e.g. Baranken, Ziv-Zakai, etc.) it is easy to apply and (2) the resulting bound is an upper bound on performance in that other tighter bounds show that this upper bound cannot be achieved in practice (see Seidman [3]). In the above context, then, the Cramer-Rao bound represents a relatively easily applied, yet severe, test of algorithm performance.

3.1 The Cramer-Rao Inequality

Development of the Cramer-Rao inequality is readily available (see for example [4], [5] and [6]) and states that any unbiased estimator must satisfy the following relation

$$E\left[(\hat{\theta}-\theta)^2\right] \geq \frac{1}{E\left\{\left[\frac{\partial}{\partial\theta}\,\ell np(x_1,x_2,\ldots x_n|\theta_1,\theta_2)\right]^2\right\}} \tag{21}$$

where $\theta_2 = \theta_2(\theta)$, a function of θ

θ and θ_1 are unknown constants to be estimated from experimental data

$p(x_1,x_2,\ldots x_n|\theta_1,\theta_2)$ denotes the probability density function of measured data $x_1,x_2,\ldots x_n$ given θ_1 and θ_2

$\hat{\theta}$ is an estimate of parameter θ

and E denotes expectation.

In this analysis $p(x_1,x_2,\ldots x_n|\theta_1,\theta_2)$ is assumed to follow the Gaussian law since the experimental data from which significant waveheight is estimated is obtained by linearly combining a large number of individual noisy return signals.

3.2 Analysis

For purposes of this analysis the ideal, normalized GEOS-3 average return waveform is assumed to be specified by [7]*

$$y(t) = y(t,\theta_1,\theta_2) = \frac{1}{\sqrt{2\pi}} \int_{-\infty}^{v} e^{-u^2/2}\,du \tag{22}$$

where $v = (t-\theta_1)/\sqrt{\theta_2}$,

θ_1 = constant ,

$\theta_2 = \sigma_{tt}^2 + (H_{1/3}/2c)^2$,

σ_{tt}^2 represents altimeter point target effects,

*A similar analysis is given in [7], however, the Cramer-Rao bound relating to rise-time not $H_{1/3}$ was used.

$H_{1/3}$ is significant waveheight ,

and c is the speed of light in units of meter/nanosec.

The time-averaged GEOS-3 return waveform at the output of the sampling gates is represented by the following model [7]

$$x(t_n) = y(t_n,\theta_1,\theta_2) + z(t_n) \quad , \quad n = 1,2,\ldots,N_1 \tag{23}$$

$$\text{with} \quad \sigma_z^2(t_n) = \text{Var}[z(t_n)] = \frac{1}{F^2}\left[y(t_n,\theta_1,\theta_2) + \frac{1}{\left(\frac{S}{N}\right)^2} \right]$$

S/N = altimeter IF signal to noise ratio

F^2 = a system constant which for a 1-second averaging period is equal to 200

$N_1 = 16$

$x(t_n)$ = observed signal at n^{th} sample gate

$y(t_n,\theta_1,\theta_2)$ = observed signal in absence of noise

$z(t_n)$ = additive, independent Gaussian noise

$t_{n+1} - t_n = 6.25$ nano sec, $n = 1,2,\ldots N_1$.

In this model $y(\cdot)$ represents the true received waveshape and $z(\cdot)$ the noise which arises mainly from the fluctuating nature of the received signal. For substantial averaging periods $z(\cdot)$ is Gaussian by the central limit theorem. The present study will be concerned only with the high signal-to-noise case so the term $(S/N)^{-2}$ in the noise model will be dropped.

For the above model assumptions, the likelihood probability function for observing $x(t_1),x(t_2),\ldots x(t_n)$ given θ_1 and $H_{1/3}$ is, since the noise is independent and Gaussian distributed

$$L(x_1,x_2,\ldots x_n|\theta_1,H_{1/3}) = K \prod_{n=1}^{N_1} \frac{1}{\sigma_z(t_n)} \exp\left\{\frac{-\left[x(t_n) - y(t_n)\right]^2}{2\sigma_z^2(t_n)}\right\}$$

Therefore, the likelihood equation is

$$\ell(x_1,x_2,\ldots x_n|\theta_1,H_{1/3}) = K_1 - \sum_{n=1}^{N_1} \ell n\, \sigma_z(t_n) - \sum_{n=1}^{N_1} \frac{\left[x(t_n) - y(t_n)\right]^2}{2\sigma_z^2(t_n)} \qquad (24)$$

where $K_1 = \ell nK$ = constant.

Taking the partial derivative of ℓ with respect to model parameter q_i ($q_1 = \theta_1$, $q_2 = H_{1/3}$) gives

$$\frac{\partial \ell}{\partial q_i} = \sum_{i=1}^{N_1} \frac{1}{\sigma_z(t_n)} \frac{\partial \sigma_z(t_n)}{\partial q_i}$$

$$+ \frac{1}{2} \sum_{i=1}^{N_1} \left\{ \frac{2\left[x(t_n) - y(t_n)\right]}{\sigma_z^2(t_n)} \frac{\partial y(t_n)}{\partial q_i} \right.$$

$$\left. - \frac{\left[x(t_n) - y(t_n)\right]^2}{\sigma_z^4(t_n)} \frac{\partial \sigma_z^2(t_n)}{\partial q_i} \right\} \; ; \; i = 1,2 \; . \qquad (25)$$

After taking the derivatives indicated in equation (25), substituting for $\sigma_z^2(t_n)$, squaring the result, neglecting all terms divided by F^2 or F^4 and taking the expectation there results

$$E\left[\left(\frac{\partial \ell}{\partial q_i}\right)^2\right] = \sum_{n=1}^{N_1} \frac{1}{\sigma_z^2(t_n)} \left(\frac{\partial y(t_n)}{\partial q_i}\right)^2 \; ; \quad i = 1,2 \qquad (26)$$

From section 3.1 the Cramer-Rao inequality states that

$$E\left[(\hat{q}_i - q_i)^2\right] \geq \left[\sum_{n=1}^{N_1} \frac{1}{\sigma_z^2(t_n)} \cdot \left(\frac{\partial y(t_n)}{\partial q_i}\right)^2\right]^{-1} \qquad (27)$$

where $q_1 = \theta_1$ and $q_2 = H_{1/3}$.

Equation (27) can be optimistic when more than one parameter must be estimated. For the case at hand both θ_1 and $H_{1/3}$ must be determined; therefore, as discussed in [6] the Fisher's information matrix is appropriate and leads to the following definitions

$$J = (J_{ij}) = \text{Fisher Information matrix}$$

with elements

$$J_{ij} = E\left[\frac{\partial \ell}{\partial q_i} \quad \frac{\partial \ell}{\partial qj}\right] \quad ; \quad i,j = 1,2 \quad .$$

In the multidimensional case the Cramer-Rao inequality takes the following form [6]:

$$E\left[(\hat{q}_i - q_i)^2\right] \geq \left(J^{-1}\right)_{ii} \quad ; \quad i = 1,2 \quad . \qquad (28)$$

With the aid of Leibnetz's rule the derivatives required for the Fisher information matrix can be evaluated and are

$$J_{11} = E\left[\left(\frac{\partial \ell}{\partial \theta_1}\right)^2\right] = \frac{100}{\pi\theta_2} \sum_{n=1}^{N_1} \frac{e^{-w}}{y(t_n,\theta_1,\theta_2)} \qquad (29a)$$

$$J_{22} = E\left[\left(\frac{\partial \ell}{\partial \theta_2} \quad \frac{\partial \theta_2}{\partial H_{1/3}}\right)^2\right] = \frac{100\, H_{1/3}^2}{\pi(2c)^4\theta_2^3} \sum_{n=1}^{N_1} \frac{(t_n-\theta_1)^2\, e^{-w}}{y(t_n,\theta_1,\theta_2)} \qquad (29b)$$

$$J_{12} = E\left[\left(\frac{\partial \ell}{\partial \theta_1}\right)\left(\frac{\partial \ell}{\partial H_{1/3}}\right)\right] = J_{21} = \frac{-25\, H_{1/3}}{2c\pi\theta_2^2} \sum_{n=1}^{N_1} \frac{(t_n - \theta_1)\, e^{-w}}{y(t_n, \theta_1, \theta_2)} \qquad (29c)$$

$$\text{where} \quad w = \frac{\left[2c(t_n - \theta_1)\right]^2}{(2c\,\sigma_{tt})^2 + H_{1/3}^2}$$

For $J_{12} \neq 0$ (i.e. non-zero correlation between θ_1 and $H_{1/3}$) it follows that (see [6]) the variance of the estimator $\hat{H}_{1/3}$ satisfies the expression

$$\sigma^2_{\hat{H}_{1/3}} > \frac{1}{J_{22}} = \frac{\pi(2c)^4\theta_2^3}{100\, H_{1/3}^2} \quad \frac{1}{\sum_{n=1}^{N_1} \frac{(t_n - \theta_1)^2}{y(t_n, \theta_1, \theta_2)}\, e^{-w}} \qquad (30)$$

As $H_{1/3} \to 0$, note the asymptotically unbounded nature of estimator variance $\sigma^2_{\hat{H}_{1/3}}$. Thus for calm sea conditions, any minimum variance unbiased estimator can be expected to display poor performance. The three estimators discussed in Section 2 of this report are characterized by erratic performance as $H_{1/3} \to 0$. In Section 3.4 the Cramer-Rao bound for GEOS-3 $H_{1/3}$ estimators will be presented from results obtained via a numerical evaluation of the inverse of Fisher's information matrix, equation (29).

3.3 Modeling Altimeter Tracking Loop Jitter

In the foregoing analysis the model employed in the development leading to equations (29) did not consider altimeter tracking loop jitter effects. Since this is an important effect the resulting Cramer-Rao bound must reflect its presence. Brown [8] studied jitter effects on the Skylab S-193 altimeter performance. In this section results from the analysis in [8] will be adapted, using approximations, for use in the present study. In effecting this

adaptation the goal is to achieve a closed form, easily evaluated result from inductive arguments based upon assumptions.

Tracking loop jitter manifests itself in two distinct ways:

(a) Introduction of a smearing effect on the average ideal return waveform $y(t,\theta_1,\theta_2)$, and

(b) Enhancement of the altimeter noise process $\sigma_z^2(t)$.

With respect to (a), jitter will be modelled as an effectively increased point target function which combines in a root sum square sense. That is, with jitter included, the point target function is

$$\sigma_{tt}\Big)_j = \left(\sigma_{tt}^2 + \sigma_j^2\right)^{1/2} \quad \text{nano sec.} \tag{31}$$

where $\sigma_j = 4.0$ as determined from experiment.

Noise enhancement, (b) above, as shown by Brown [8], can be described by the following convolutional sums (using notation of this chapter)

$$E[z(t)] = K_o \sum_{m=-\infty}^{\infty} p_m y(t+m\tau) \tag{32a}$$

and

$$E\left[z^2(t)\right] = K_o^2 \sum_{m=-\infty}^{\infty} p_m \left\{ \left[y(t+m\tau) + \left(\frac{N}{S}\right)\right]^2 + y^2(t+m\tau)\right\} \tag{32b}$$

where K_o = a system constant

E is expectation operator

p_m = probability masses of the discrete jitter probability density function

S/N = IF signal to noise ratio

τ = time quantization parameter of the altimeter tracking loop

$z(\cdot)$ = average return waveshape with jitter included.

Assuming for the moment that a hypothetical radar average return pulse is a step function (i.e. transmitted pulse is the Dirac delta function), that time quantization is small (i.e. $\tau \to 0$), and $S/N \to \infty$ equation (32) can be expressed as follows

$$E[z(t)] = K_o \int_{-\infty}^{\infty} p_m(v)\ y_\mu(t+v)\ dv \tag{33a}$$

$$E[z^2(t)] = K_o^2 \int_{-\infty}^{\infty} 2p_m(v)\ y_\mu(t+v)\ dv \tag{33b}$$

with $y_\mu(\cdot)$ a unit step function.

Thus the average noise effect of jitter, for the special case considered, can also be described by a spreading effect on the average return waveform coupled with a nonlinear combination. Assuming an identical phenomenological noise effect in the non-ideal GEOS-3 altimeter results in an increased noise level given by the relation

$$\sigma^2_{z(t)} = E[z^2(t)] - [Ez(t)]^2$$

$$= 2y(t,\theta_1,\theta_2) - y^2(t,\theta_1,\theta_2) > 0 \tag{34}$$

where now $\theta_2 = \sigma^2_{tt}\Big)_j + \left(H_{1/3}/2c\right)^2$.

3.4 Computational Results

To evaluate the Cramer-Rao bound a computer program was written and used to compute the elements of Fisher's information matrix (equation (29)). The results are shown in graphic form in Figure 3.1 where three curves have been plotted with (1) jitter effects totally omitted, (2) partial jitter effects resulting from effective increase in point target response, and (3) including total jitter effects (i.e. both effects (a) and (b) of Section 3.3). It is emphasized that the estimator performance curves plotted in Figure 3.1, under the model employed, define performance limits which cannot be surpassed by any unbiased estimator. Also, the severe degradation of estimator performance for $H_{1/3} < 3$ meters is significant and has been observed in the analysis of GEOS-3 data.

In obtaining the data for use in Figure 3.1, θ_1 was used as a parameter to verify that the resulting bounds were, for all practical purposes, not affected by the position, in the GEOS-3 sampling gate set, of the return signal.

Figure 3.2, shown for comparison with Figure 3.1, illustrates two Cramer-Rao performance limits curves for $H_{1/3}$ estimators since jitter effects were ignored altogether and it was further assumed that $y(t,\theta_1,\theta_2)$ was available in continuous form. The dashed curve of this figure is an estimate of performance achieved by the $H_{1/3}$ estimator presently used for GEOS-3 computations [2]. Referring to Figure 3.1, it can be seen that the GEOS-3 $H_{1/3}$ estimator closely approaches the Cramer-Rao bound.

The GEOS-3 performance limit curve shown in Figure 3.2 was drawn from the relation

$$E\left[\left(\hat{H}_{1/3} - H_{1/3}\right)^2\right] \geq \frac{64\sqrt{\pi}\, c^4\, \theta_2^{3/2}\, \sigma_N^2}{H_{1/3}^2} \tag{35}$$

which following [4] was derived under the assumptions of continuous measurements

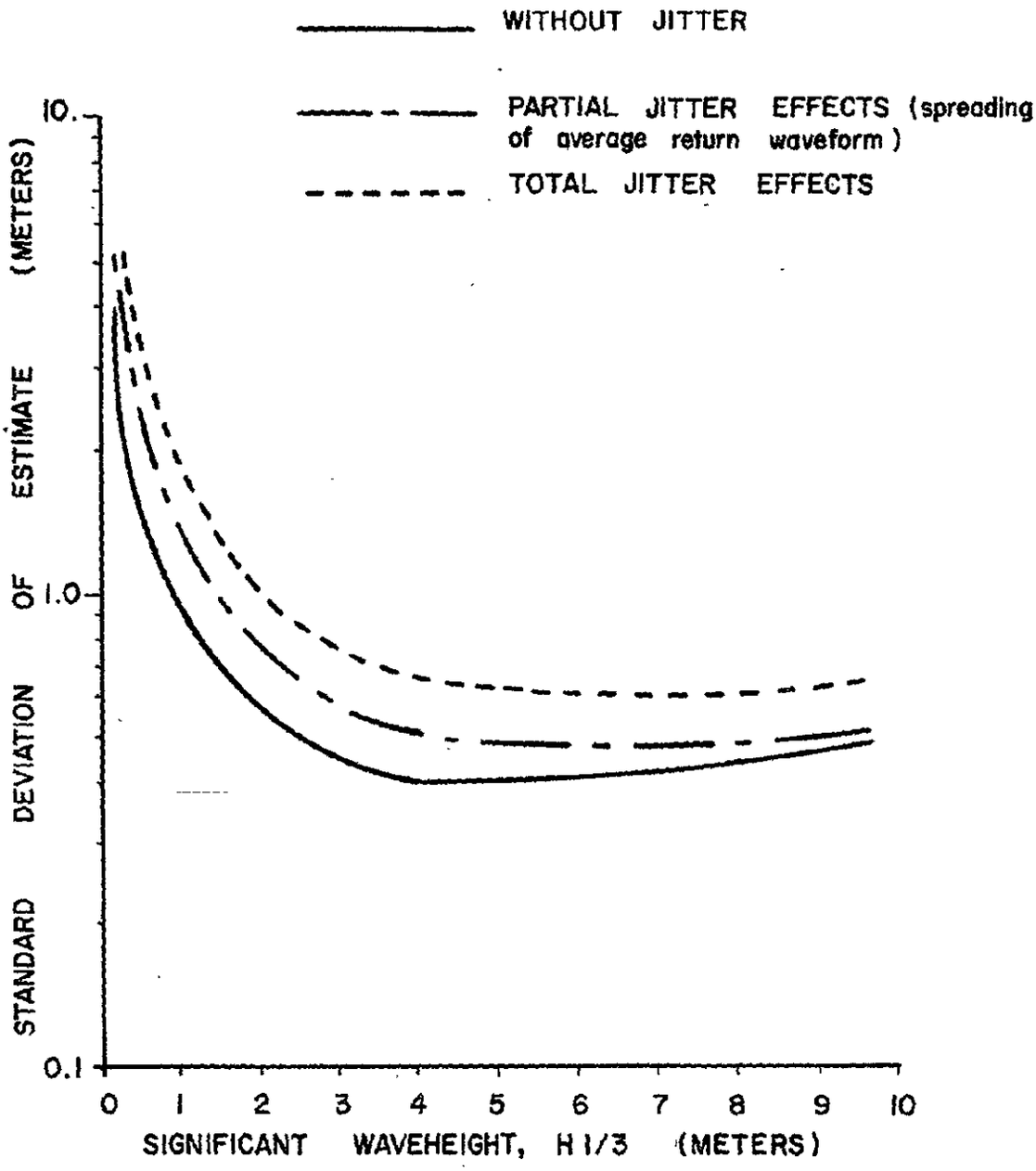

Figure 3.1. Calculated GEOS-3 $H_{1/3}$ resolution.

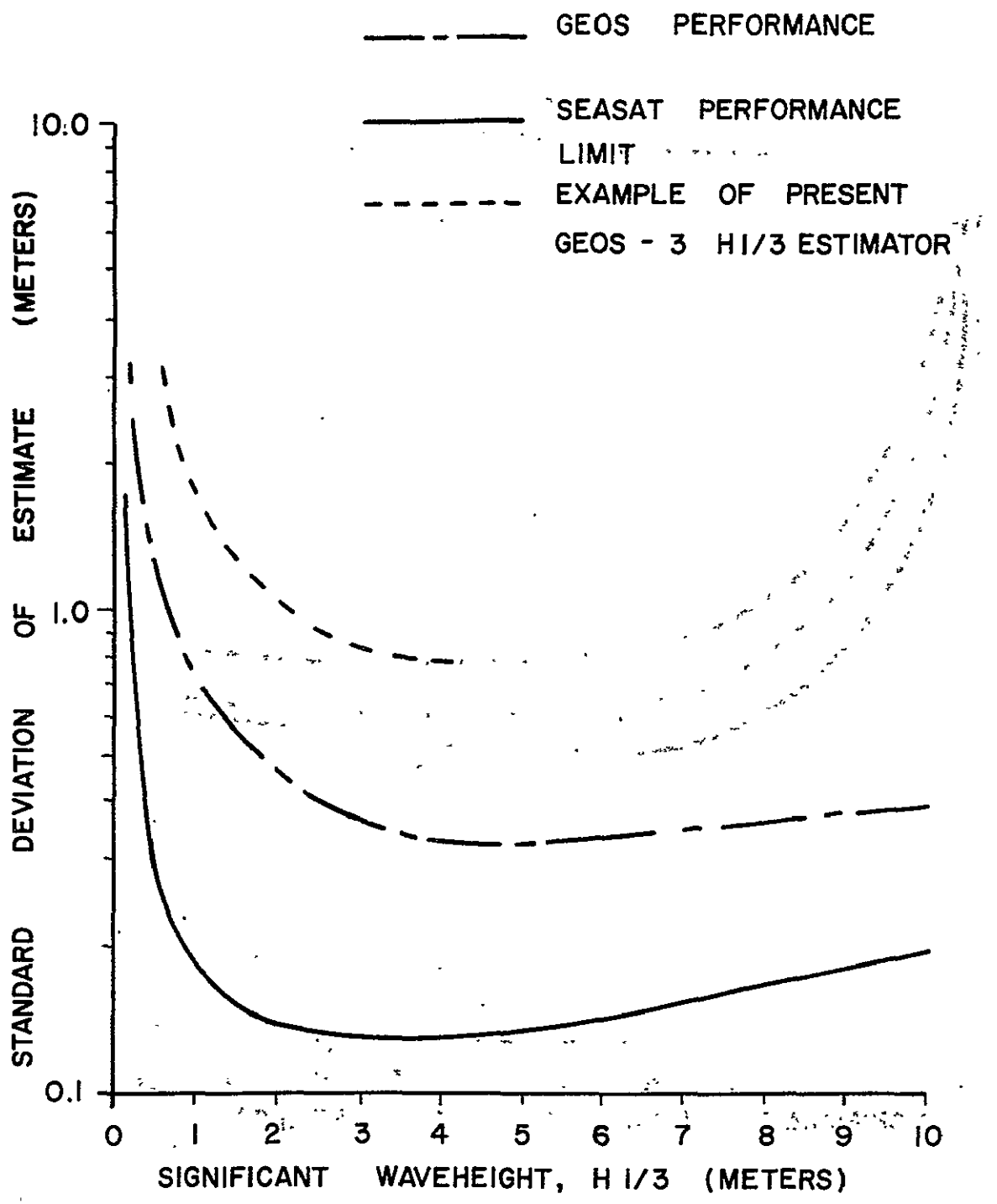

Figure 3.2. Calculated and measured GEOS-3 $H_{1/3}$ resolution compared to the calculated SEA SAT resolution.

perturbed by white noise with $\sigma_N = 0.06$. SEASAT performance limitation was obtained from equation (35) assuming a point target standard deviation of 3.0 nano sec. and a pulse repetition frequency ten times that of GEOS-3.

3.5 Variance-Based $H_{1/3}$ Algorithm

The above discussed bounds indicate an interesting paradox - variance of the estimate appears to be a very sensitive parameter for $H_{1/3}$ values between 0 - 3 meters. This behavior suggests the possibility of merging an estimate based on waveform data with one based on variance behavior. This possibility is explored in the next few paragraphs.

Computation of waveheight data based on variance or standard deviation values was first suggested by the waveheight resolution analysis given in [1]. For this reason, the algorithm to be given is based on a curve-fit using the functional form

$$\sigma^2_{H_{1/3}} = \frac{.042\left(7.66\ H^2_{1/3} + T^2\right)^2 + .546\ \sigma_j^2\left(7.66\ H^2_{1/3} + T^2\right)}{H^2_{1/3}\, R\, t}$$

where

$H_{1/3}$ = significant waveheight in meters

σ_j = altitude tracking jitter in n.s.

T = 3 dB post detection pulse width in n.s.

t = smoothing interval in sec.

R = variance reduction factor

The above equation was written as $H_{1/3}$ versus variance and the R factor empirically determined by curve filtering to a scatter-plot of $H_{1/3}$ values (as determined by the waveform algorithm) versus NOAA/SMG ground-truth data. The numerical values of the parameters were $\sigma_j = 3$ n.s. and T = 10 n.s. The fitted

curve was previously shown in Figure 3.2.

Computation of waveheight values using the variance relationship involves the following steps:

1. Six frame estimates of mean and standard deviation are first computed using per-frame $H_{1/3}$ numbers (in meters) as input values
2. The standard deviation (σ) value is then tested to determine if it is $\geq .815$; if not the 6 frame mean values computed in the first step are used as $H_{1/3}$ values
3. If $\sigma \geq .815$ the variance algorithm is used in the form

$$H_{1/3} = \left\{ \left(63.03\ \sigma^2 - 20.72\right) - \sqrt{\left(63.03\ \sigma^2 - 20.72\right)^2 - 370.59} \right\}^{1/2}$$

A comparison of the $H_{1/3}$ values obtained using the two algorithms is shown in Figures 3.3 and 3.4. In each figure, $H_{1/3}$ values obtained using the waveheight algorithm is shown as the solid line and values from the variance algorithm is shown as the dashed line; any discontinuities in the dashed line indicate that the computed waveheights exceeded 3.5 meters according to the condition $\sigma < .815$. These figures also show NOAA/SMG estimates of waveheight; additionally, Figure 3.3 gives the $H_{1/3}$ value measured by the laser profilometer. Examination of the data shown in these figures indicates the variance-derived estimate to be in better agreement with the available ground truth data. The rapid changes in the dashed curve near the end of the data-span in Figure 3.3 is thought to be due to non-stationarity of input values rather than to real waveheight changes. Additional ground truth data is needed to fully evaluate the variance algorithm - note that the one available measured value (from the profilometer) is in very good agreement with the algorithm.

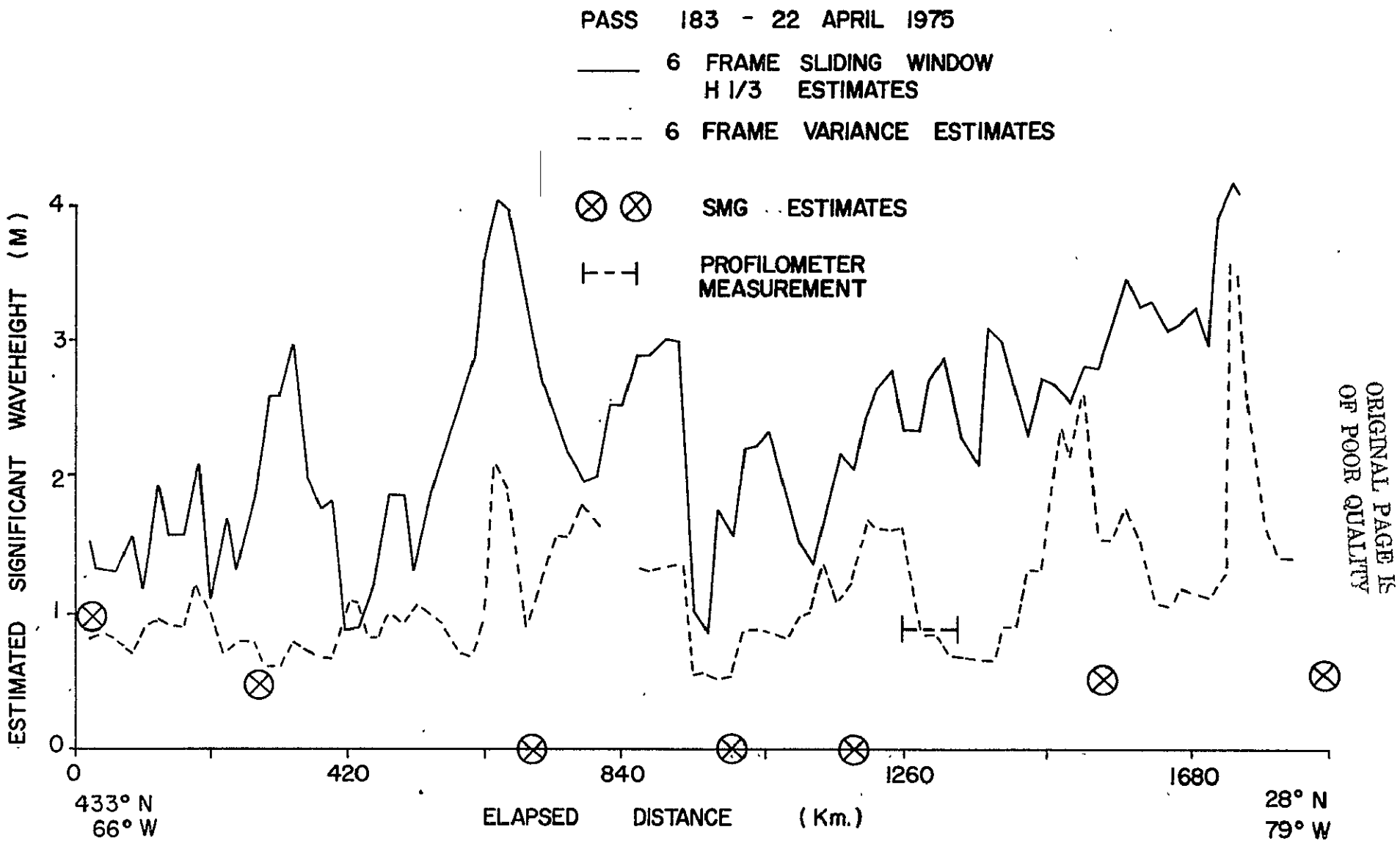

Figure 3.3. Comparison of $H_{1/3}$ values obtained from the WFC algorithm (solid curve) and from the variance-based algorithm (dashed curve), SMG and profilometer $H_{1/3}$ values are also shown.

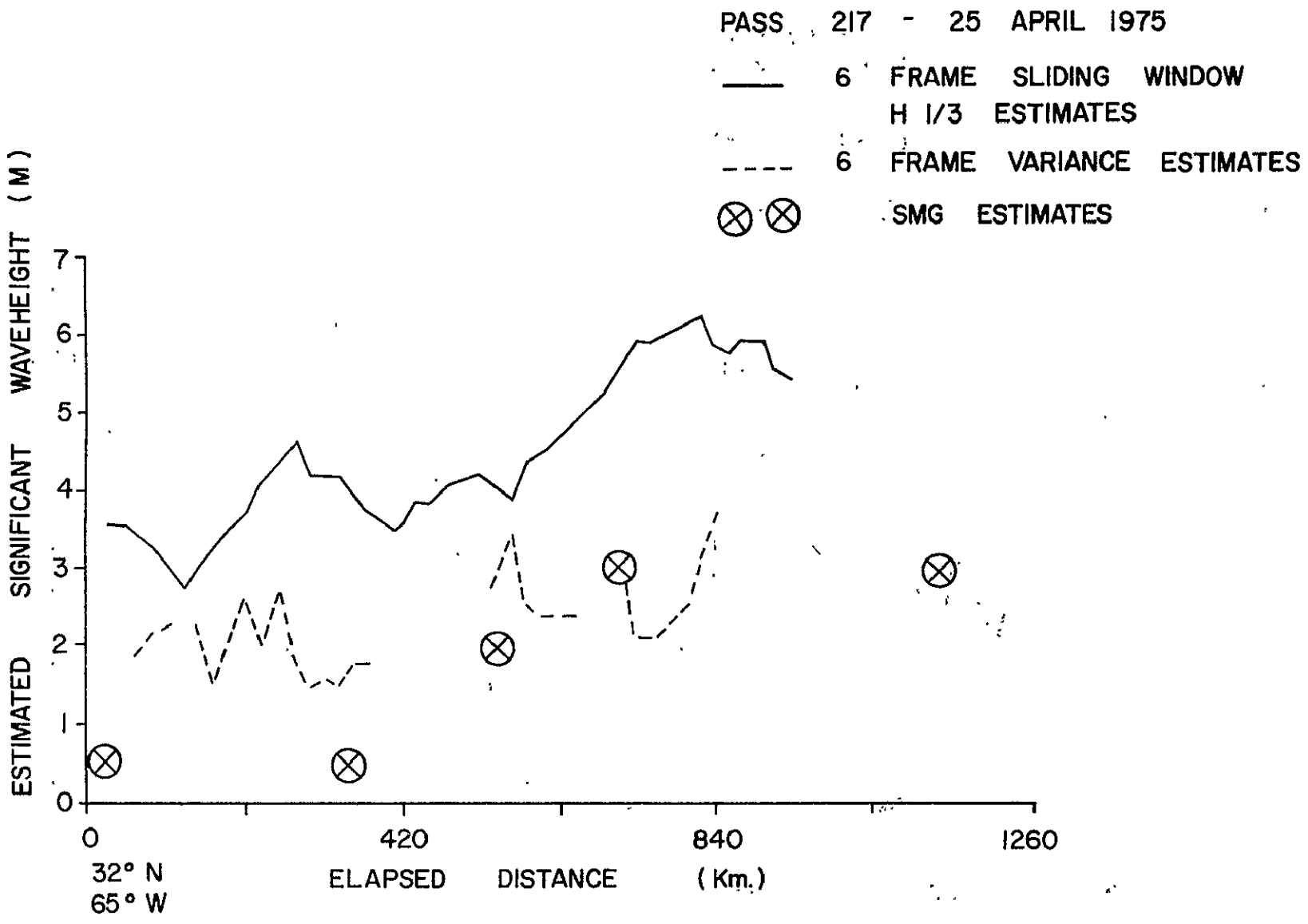

Figure 3.4. Comparison of $H_{1/3}$ values obtained from the WFC algorithm (solid curve) and from the variance-based algorithm (dashed curve).

3.6 Conclusions

The GEOS-3 $H_{1/3}$ estimator currently in use closely approximates the performance bound developed from the model presented. $H_{1/3}$ computation is a highly nonlinear problem which for GEOS-3 is solved by conversion to a linearized model which is iterated to convergence [2]. It has been shown that such linearized estimators, under appropriate conditions, are unbiased [9,10]. This implies that the current GEOS-3 $H_{1/3}$ estimator, while a suboptimal one, achieves near-optimal performance.

A significant result of the analysis is that under calm-sea conditions (i.e. $H_{1/3} \to 0$) the performance of any estimator of $H_{1/3}$ can be expected to exhibit marked degradation. Two obvious techniques for combating this problem are (a) use of higher pulse repetition frequencies and (b) reduction of point target effects, σ_{tt}. Of course neither of these options is applicable to GEOS-3.

There is a theoretically optimum $H_{1/3}$, in the sense that estimates of this one particular value will have minimum variance compared to that of all other values of $H_{1/3}$. For the GEOS-3 radar parameters, this optimum value is within the 4.0 - 5.0 meter range and is characterized by a very broad minimum (Figure 3.2).

REFERENCES

[1] Miller, L. S.; and Brown, G. S.: Engineering Studies Related to the GEOS-C Radar Altimeter, Final Report for Task D, NASA Contract NAS6-2307, May, 1974.

[2] Hayne, G. S.: Initial Development of a Method of Significant Waveheight Estimation for GEOS-III, NASA Contract Report NASA CR-141425, August, 1977.

[3] Seidman, L. P.: Performance Limitations and Error Calculations for Parameter Estimation, Proceedings of IEEE, Vol. 58, No. 5., pp. 644-652, May, 1970.

[4] Nahi, N. E.: Estimation Theory and Applications, John Wiley, 1969.

[5] Van Trees, H. L.: Detection Estimation and Modulation Theory (Part 1), John Wiley, 1968.

[6] Whalen, A. D.: Detection of Signals in Noise, Academic Press, 1971.

[7] Hofmeister, E. L. et al.: Data User's Handbook and Design Error Analysis-GEOS-C Radar Altimeter, Volume I, Prepared by General Electric Co., under Contract Numbers NAS6-2619 and JPL 372165, May, 1976.

[8] Brown, G. S. (Editor): Skylab S-193 Radar Altimeter Experiment Analysis and Results, NASA CR-2763, February, 1977.

[9] Fedorov, V. V.: Theory of Optimal Experiments, Academic Press, 1971.

[10] Hartley, H. O.: Modified Gauss Method for Fitting of Nonlinear Regression Functions, Technometrics 3, p. 269, 1968.

4.0 DISCUSSION OF OCEAN BACKSCATTERED SIGNAL CHARACTERISTICS

This section presents a discussion and interpretation of GEOS-3 data for cases in which the AGC values increase markedly for brief periods. These abrupt AGC changes have been observed in a considerable number of passes; Figure 4.1 shows the geographical distribution of occurrence of these AGC changes noted in the examination of approximately 75 records. It was thought that such a map might show a pattern, or grouping, in these occurrences (such as near the Gulf Stream), however, the distribution shown in Figure 4.1 is considered to essentially represent the geographic distribution of the underlying data base. This result suggests that these comparatively brief elevations in AGC values are the result of relatively calm ocean surface conditions, and are not caused by anomalous conditions. This premise is examined in the following paragraphs.

First examining the theoretically predicted values of σ°; standard references give the appropriate form as

$$\sigma_o(\theta) = \frac{|R(\theta)|^2 \, \ell^2}{4\sigma_s^2 \cos^4\theta} \, e^{-\frac{\ell^2}{4\sigma_s^2}\tan^2\theta}$$

where R = Fresnel reflection coefficient,

ℓ = surface height correlation length,

σ_s = rms surface height, and

θ = off-nadir angle.

For the GEOS-3 case: $\cos\theta \simeq 1$, $\sin^2\theta \simeq c\tau/h$ and assuming $R \simeq 1$

$$\sigma_o = \left(\frac{\ell}{2\sigma_s}\right)^2 e^{-\frac{c\tau}{h}\left(\frac{\ell}{2\sigma_s}\right)^2}$$

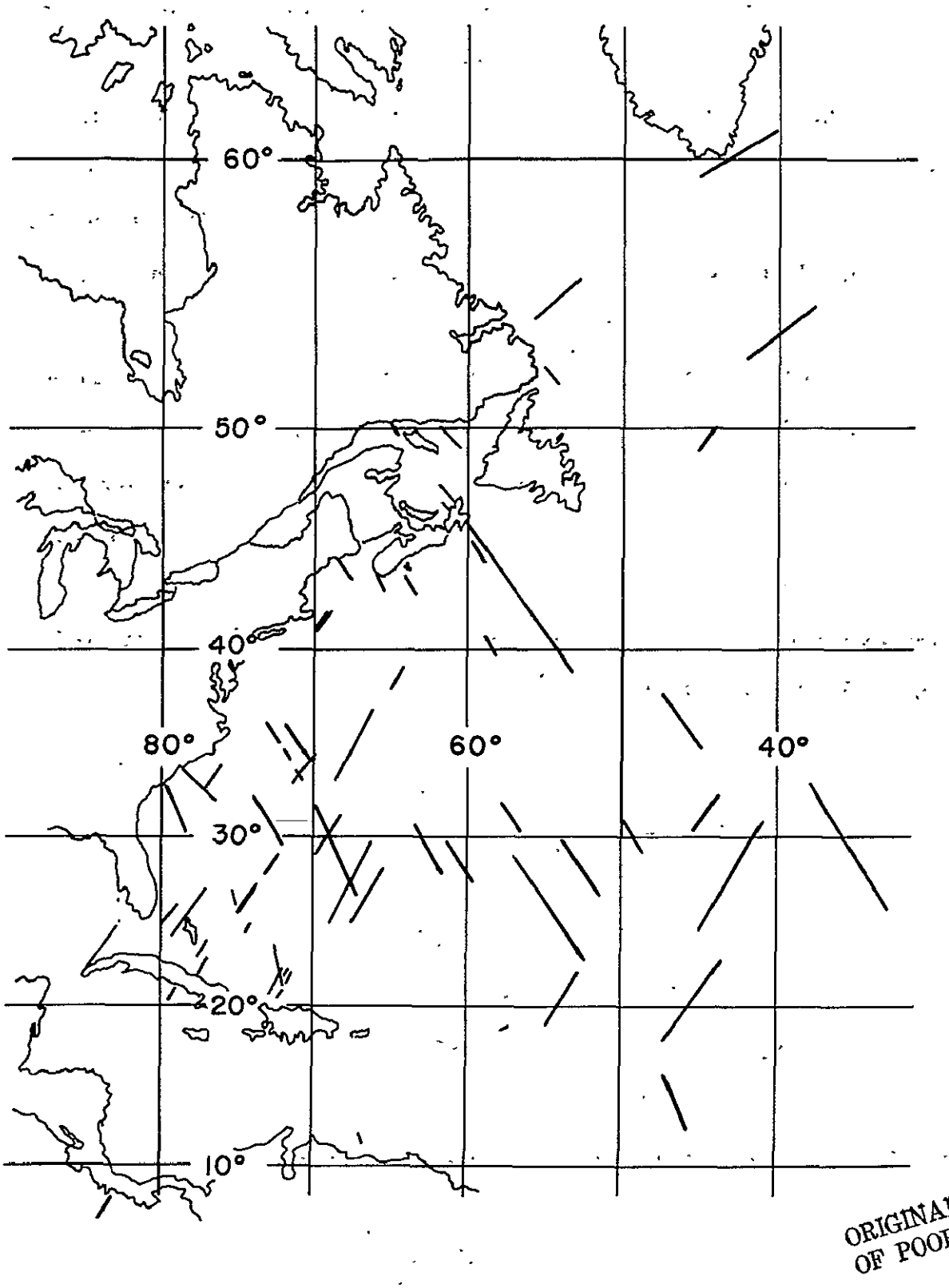

Figure 4.1. Geographic distribution of AGC step changes of $\geq$ 10 dB; approximately 75 total I-Mode AGC records examined.

Tabulated values for this equation are given below for τ = 60 ns.

$\frac{\ell}{\sigma_s}$	σ_o(dB)
3	3.52
5	7.96
10	13.97
50	27.9
100	33.75
500	42.2

The above value of τ was used to provide numerical values applicable to the AGC gate region. Note that the angular displacement of the AGC gate location from the nadir point is ~0.27 degrees, for which the decay effect of the antenna pattern is ~0.1 dB. The above tabulated σ° values indicate the values of σ° observed during the AGC step-changes are entirely consistent with backscatter theory. These theoretical values indicate that the elevated AGC conditions correspond to very calm surface conditions or to swell-dominated seas.

Figure 4.2 shows computed waveshapes as a function of ℓ/σ_s. These waveshapes show the expected decay in the plateau region between the leading edge and the AGC gate, as a function of the ratio of surface correlation length (ℓ) divided by rms surface roughness (σ_s). This result suggests the possibility of using attitude/specular gate and $H_{1/3}$ data as a means of estimating dominant surface wavelength. This possibility is next investigated.

4.1 Attitude/Specular Gate Behavior

The change in the attitude/specular gate value as a function of ℓ/σ_s may be computed using the previously given equation for σ° and the known antenna pattern behavior. Taking θ in this equation as ~1.0 degree for the attitude/specular gate angular location, the antenna pattern effect to be 3dB

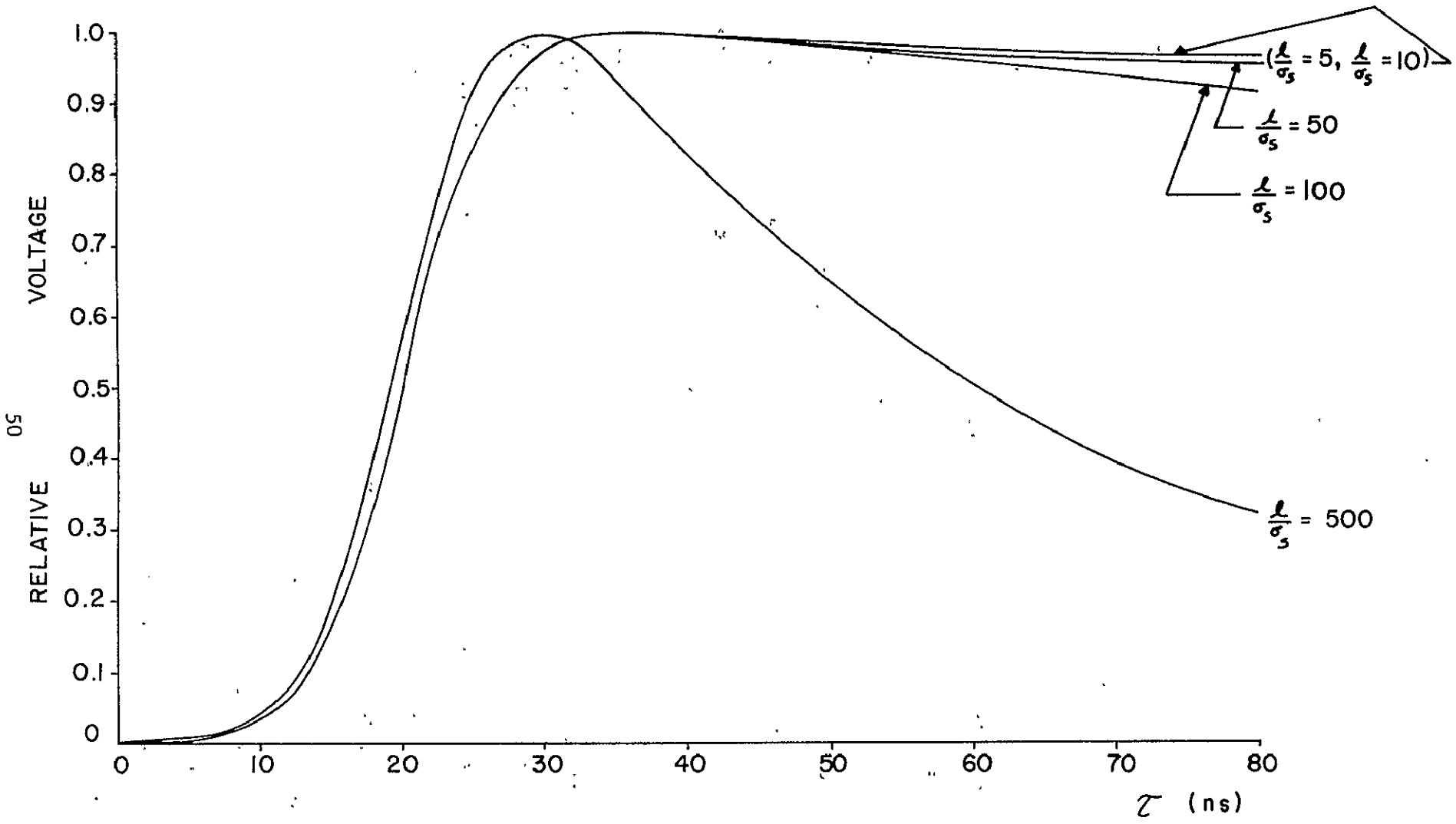

Figure 4.2. Computed GEOS-3 video waveshapes as a function of the ratio of ocean-surface correlation length to rms waveheight.

and the AGC gate nominal value to be 100 mv, the following attitude/specular (A/S) gate values are obtained.

ℓ/σ_s	A/S (mv)
20	48
40	45
80	31
100	23
200	2

In order to calculate correlation length as a function of attitude/specular gate voltage, V_{as} , a polynomial was curve-fitted to the above values. The results were

$$\ell = H_{1/3}\left[54.33 - 2.27\ V_{as} + .0587\ V_{as}^2 - 6.79 \times 10^{-4}\ V_{as}^3\right]$$

where $H_{1/3} = 4\sigma_s$ is in meters and V_{as} is in mv.

When this procedure was implemented and wavelength computed using measured V_{as} values it was soon found that GEOS-3 attitude/specular (A/S) data shows the following pattern: V_{as} values tend to first increase above 50 mv when an AGC step-change is encountered, to decrease in an expected fashion, and to again increase above 50 mv as the AGC feature is exited. This characteristic is shown in the data given in Table I, which was recorded over the Gulf of Mexico, orbit 1164.

Since backscatter theory does not admit to an increase in energy with off-nadir angle, this behavior was thought to be caused by the geometry of the A/S gate. Figure 4.3 shows the relative spatial areas of the sampling gates. Note that along-track signal level changes can be anticipated by the A/S gate by ~2 seconds (or ~1 low data rate frame period). A computer program was written to simulate the effect of such AGC changes on the A/S gate

TABLE I

LATITUDE Degrees	LONGITUDE Degrees	σ_n Meters	AGC dBm	$H_{1/3}$ Meters	AASG m.v.
26.162	277.793	.47	-70.80	-2.95	49.2
26.055	277.722	.53	-70.69	-1.78	48.4
25.948	277.650	.60	-70.59	1.84	50.3
25.841	277.579	.52	-70.15	-2.52	52.8
25.735	277.508	.35	-69.09	.47	48.8
25.628	277.437	.47	-69.28	-2.67	50.3
25.521	277.366	.99	-69.21	-1.39	54.7
25.414	277.295	.83	-67.89	2.14	48.8
25.307	277.224	.43	-68.42	1.38	50.3
25.200	277.153	.42	-68.22	-3.34	54.6
25.092	277.083	.41	-68.26	-3.63	58.3
24.985	277.012	.52	-66.42	-2.90	53.9
24.878	276.942	.37	-66.97	-3.85	49.5
24.771	276.872	.82	-67.63	1.45	62.0
24.664	276.802	.55	-67.30	-1.75	75.1
24.557	276.732	.54	-66.05	3.27	79.6
24.449	276.662	1.06	-63.09	3.40	77.0
24.342	276.592	.64	-60.76	3.04	71.1
24.235	276.522	.68	-57.84	-1.52	44.8
24.128	276.452	.44	-58.26	-3.46	44.8
24.020	276.383	.60	-57.41	-2.70	40.8
23.913	276.314	.38	-58.17	-3.28	36.4
23.805	276.244	.61	-59.20	-3.88	43.0
23.698	276.175	.56	-58.68	-3.61	46.3
23.590	276.106	.85	-59.53	-3.45	40.1
23.483	276.037	.57	-62.85	-3.03	63.8
23.376	275.968	.47	-61.69	-1.54	55.0
23.268	275.899	.71	-62.65	3.94	49.6
23.160	275.831	.62	-64.35	-1.44	45.5
23.053	275.762	.62	-65.60	-2.28	47.0
22.945	275.693	.88	-67.54	-2.03	47.8
22.838	275.625	.39	-68.33	-2.54	50.3
22.730	275.557	.58	-69.24	-3.43	50.7
22.622	275.488	.58	-69.64	-1.92	51.7
22.515	275.420	.62	-69.58	-1.87	51.0
22.407	275.352	.87	-70.12	1.70	52.1
22.299	275.284	.28	-69.79	-1.35	51.0

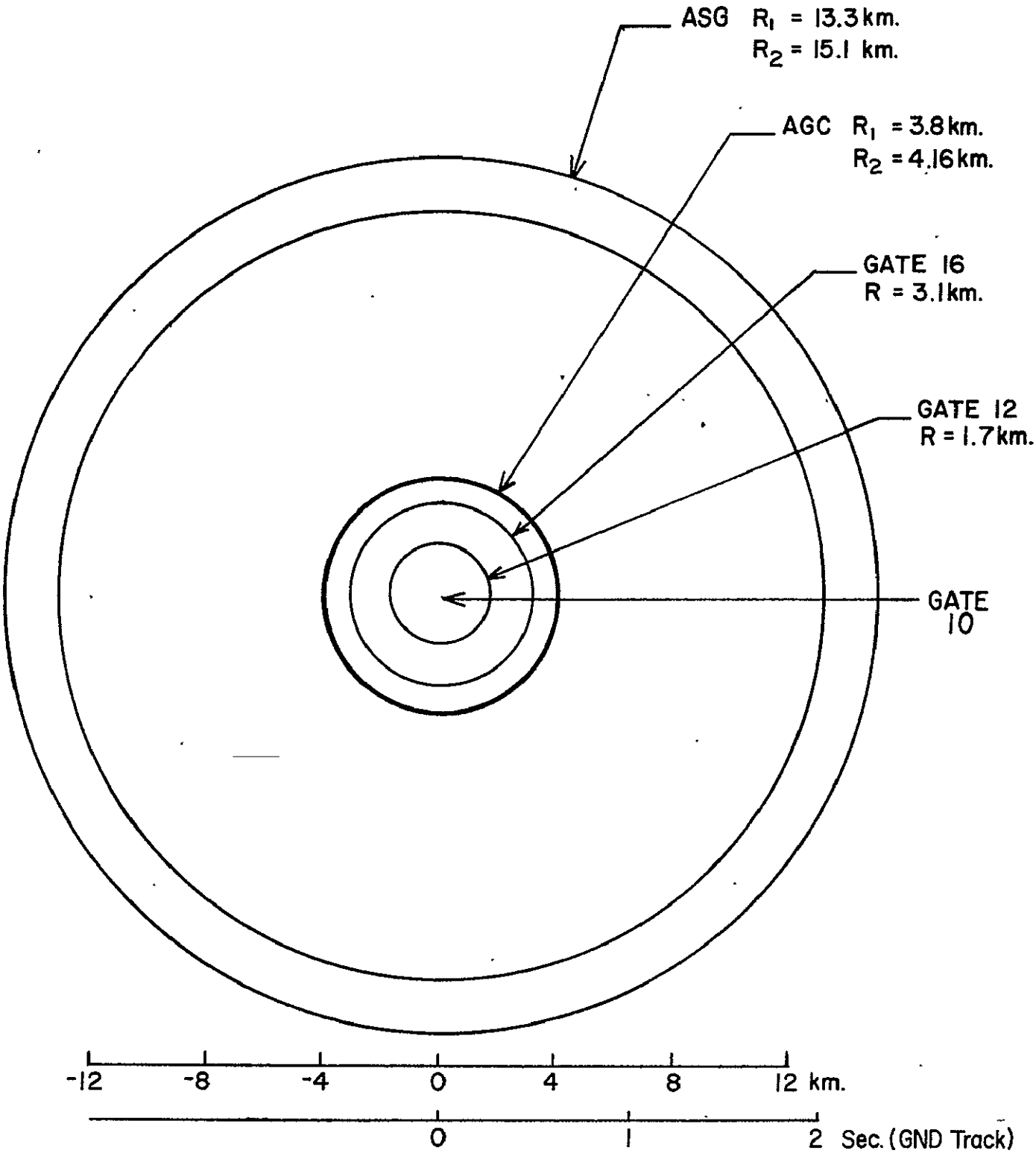

Figure 4.3. R_1 = inner radius and R_2 = outer radius of footprint.

behavior, for the case of ocean surface conditions which are homogeneous in the across track direction. This program comprised the following operations:

1) AGC values $a_1, a_2, \ldots a_n$ were read in
2) these dBm values were converted to power values A_n
3) the simulated A/S level was calculated based on the AGC power values one frame ahead and behind the nadir point, i.e.

$$A/S = \frac{A(n-1) + A(n+1)}{2}$$

4) these calculated A/S values were normalized to the nadir value and to 50 m.v. using

$$\frac{A(n)}{A/S} \times 50 .$$

A typical result from this simple model is shown in Figure 4.4. The lower graph in this figure shows the AGC features which were recorded in the Mediterranean Sea near the island of Crete (orbit 3469). Note that there are two brief changes of ~10 dB in AGC value which are not of sufficient duration to effect non-transitory conditions in the AGC and A/S gate footprints. The upper graphs in this figure show both calculated and measured A/S gate responses. These curves show that AGC disturbances alone can cause elevations above 50 m.v. in the A/S gate value. Although the calculated and observed A/S gate values are not in close agreement, the peaks and troughs and overall characteristics are considered to be in sufficient correspondence to validate the postulated mechanism. The lack of precise agreement is attributed to the (unknown) across-track variations in ocean backscatter.

The above results demonstrate that the analysis of waveform variations inferred by A/S gate-data requires that the ocean surface be essentially homogeneous over a spatial extent of tens-of-kilometers. Figure 4.5 shows

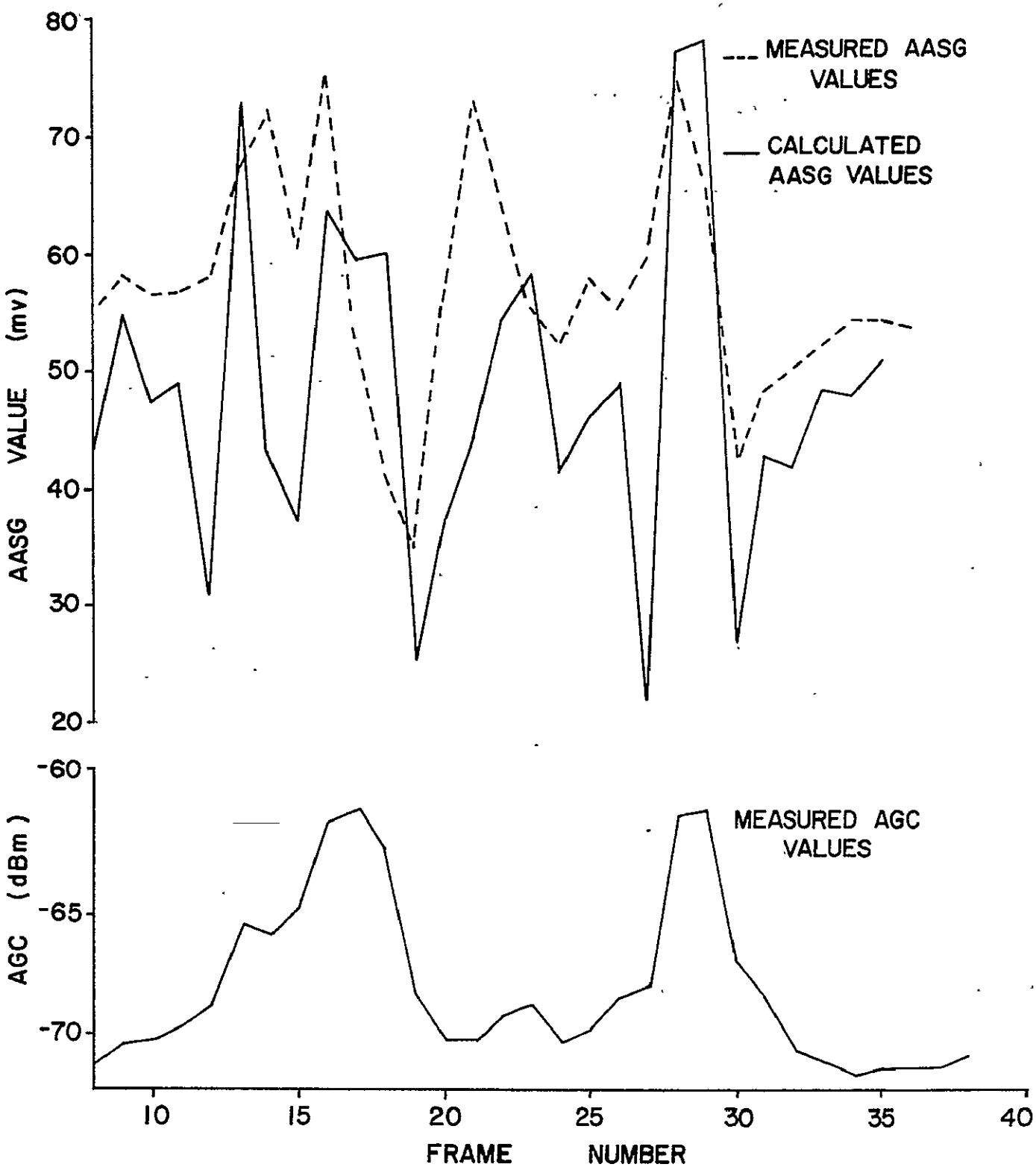

Figure 4.4. Comparison of AGC values with measured and calculated Attitude/Specular gate values, rev. 3469.

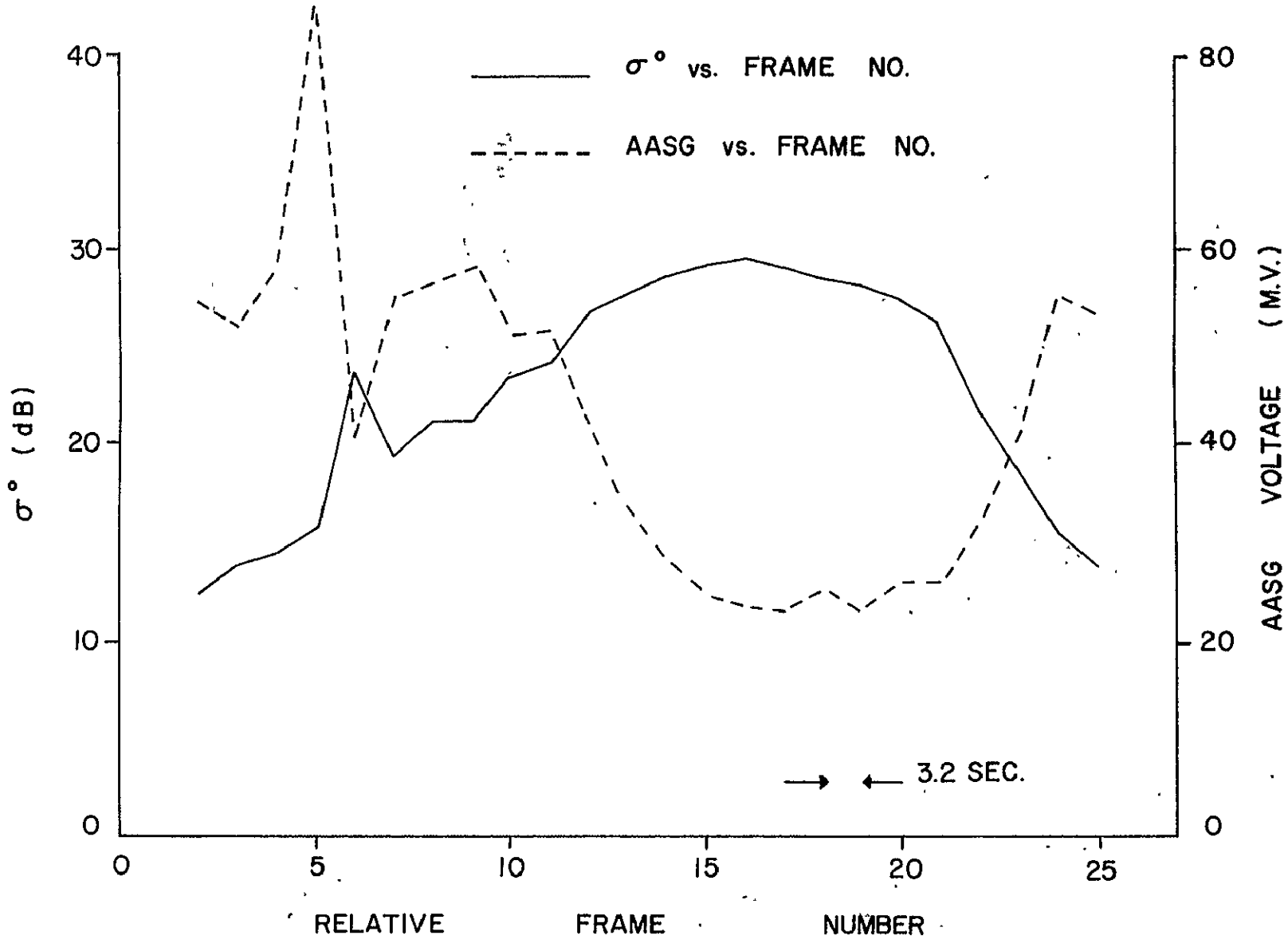

Figure 4.5. An example of a protracted rise in AGC level.

σ° and A/S gate data for one such record; these data were recorded over water between Cuba and Florida. Note that the elevated σ° values in this record persist for ~30 seconds. Measured significant waveheight during this period was ~1 meter; use of the above equation for correlation length gives $\ell = 33.7$ meters. Note that this $H_{1/3}$ value coupled with the high σ° value argues that swell is dominant; also the observed σ° value is in very good agreement with the theoretical value for this ℓ/σ_s ratio. Using the approximation: wavelength $\lambda = 4\ell$ and the standard equation for wave period T,

$$T = \sqrt{\frac{\lambda}{1.56}}$$

yields $T = 9.3$ seconds, which is a reasonable period for swell conditions.

The main uncertainty in the above calculations is in the $H_{1/3}$ value. A total of 10 per-frame $H_{1/3}$ values were averaged to obtain the value quoted above. The standard deviation in these 10 per-frame $H_{1/3}$ values was ~1.8 meters. Based on these results, it is concluded that the present $H_{1/3}$ algorithm is probably not sufficiently stable (at low waveheights) for use in estimating surface correlation length. The variance-based $H_{1/3}$ algorithm, discussed elsewhere in this report, may prove to be adequate for this purpose, if surface correlation length estimates prove to be a useful parameter.

4.2 Spatial Variability of $H_{1/3}$ Estimates

Figure 4.6 illustrates the autocorrelation function of frame averaged $H_{1/3}$ for two different averaging times. When the frame averaging time is changed from five to three the decorrelation time is affected by more than 60 percent. This is a significant effect and indicates that a five frame average of $H_{1/3}$ values can significantly affect the statistics of a three frame averaged $H_{1/3}$ process.

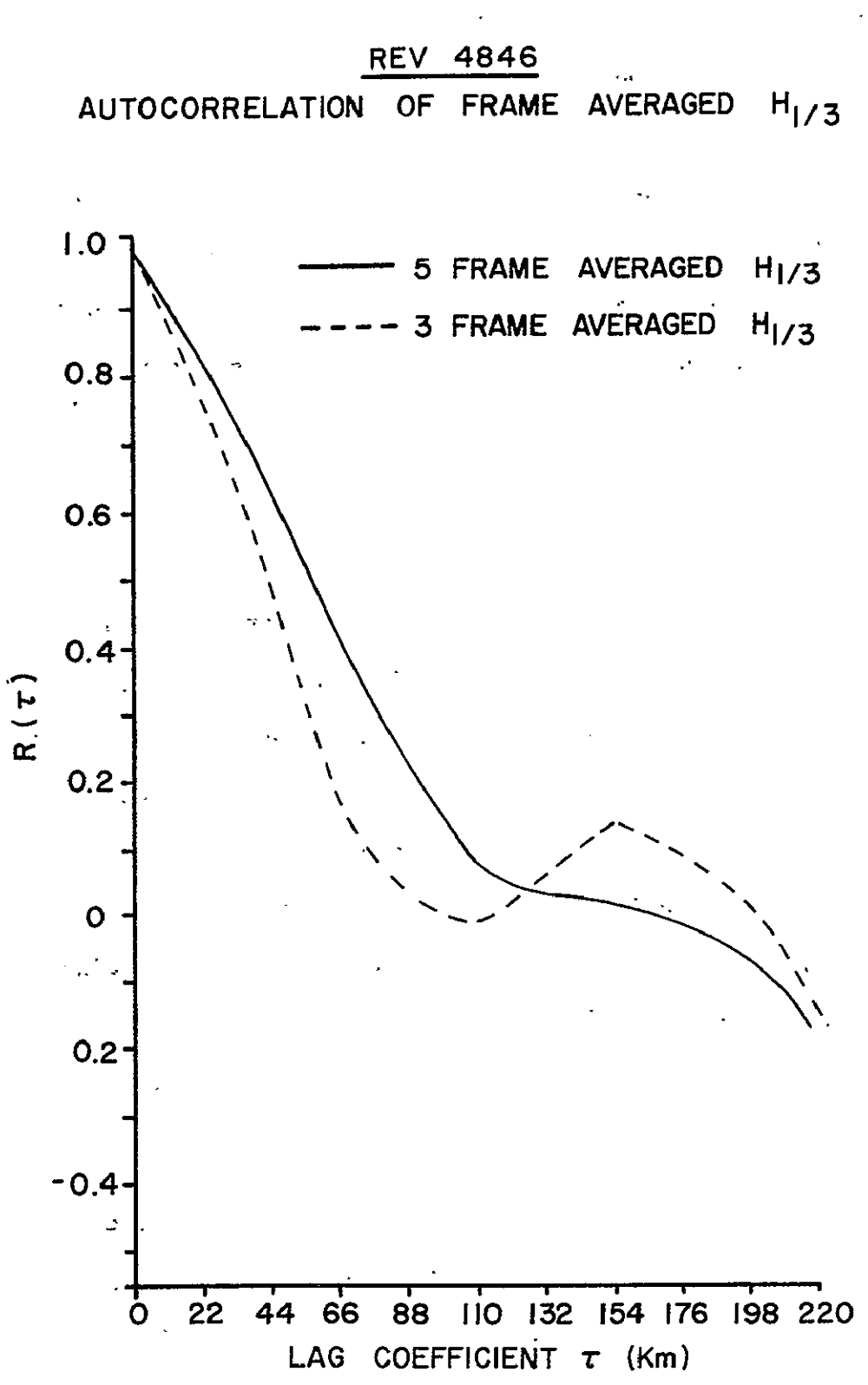

Figure 4.6. Effect of frame averaging on $H_{1/3}$ autocorrelation function.

Figure 4.7 illustrates the effects of a five-frame average of $H_{1/3}$ on the autocorrelation function. The solid curve for the autocorrelation function of unaveraged data clearly indicates the presence in the $H_{1/3}$ data of two uncorrelated processes. The first of these processes rapidly decorrelates and is probably due to Rayleigh noise caused by return signal fluctuation. The second process is characterized by slow decorrelation and represents sea state effects. Note, however, that in the average curve the two processes have been smeared together so that they are essentially indistinguishable. Based on these results it is concluded that care is required in interpretation of results based upon filtered $H_{1/3}$ data. The results of this paragraph indicate that $H_{1/3}$ can be significantly altered by filtering operations.

4.3 AGC Calibration

This paragraph gives results of σ_o values computed using both the "clean signal" and the "clutter signal" AGC calibrations. Figure 4.8 shows σ° values obtained under moderate waveheight conditions and Figure 4.9 shows σ° values during a period in which the AGC values experience a brief step change of ~10 dB. As shown in Figure 4.1, such changes have been observed over a rather wide range of geographic locations. Figures 4.8 and 4.9 show the clutter calibration data to yield better agreement with published σ° values than do the clean calibrations. For this reason, it is recommended that "clutter signal" calibrations be used in all σ° computations.

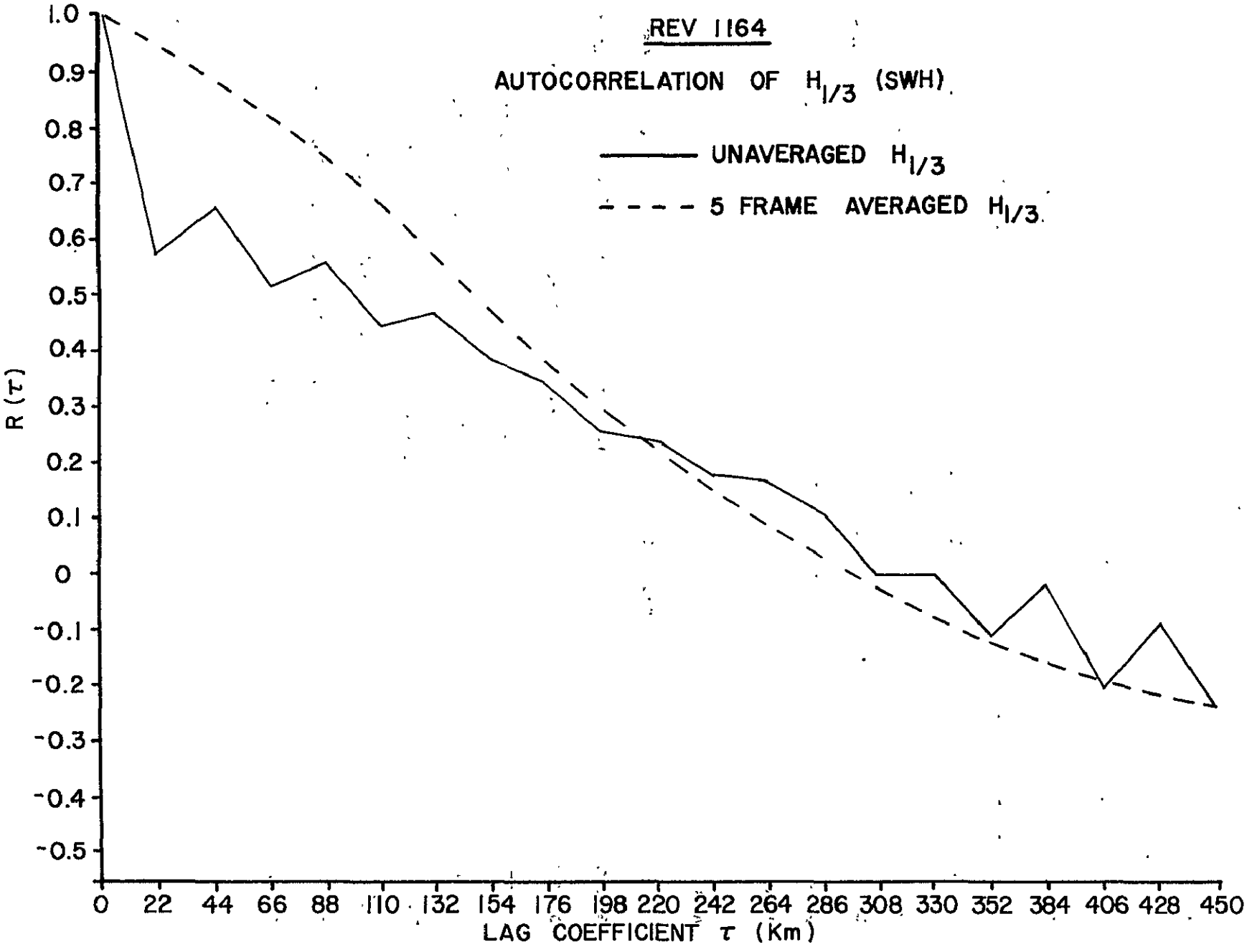

Figure 4.7. Effect of frame averaging on $H_{1/3}$ autocorrelation function.

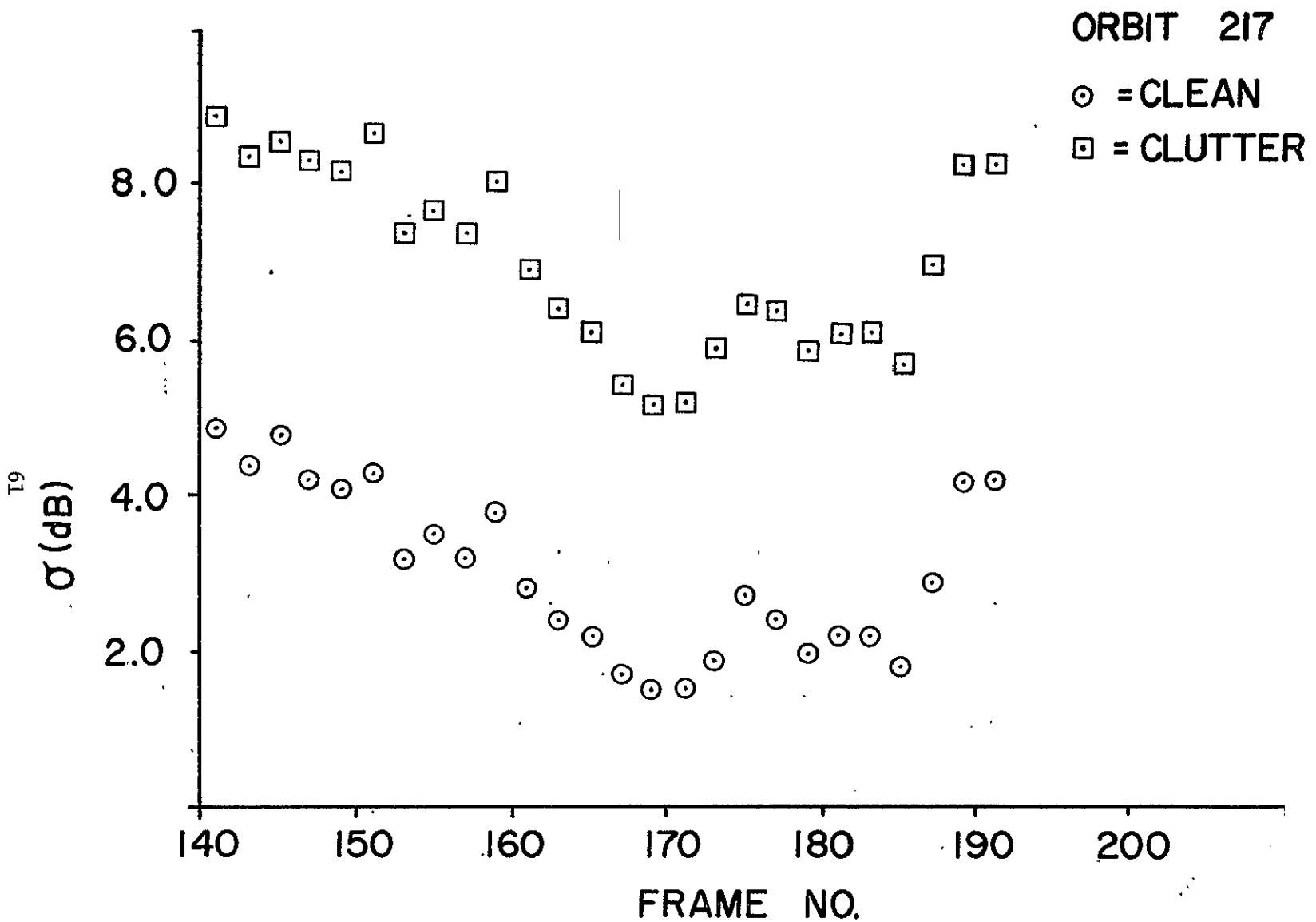

Figure 4.8. Radar cross-section values for moderate sea states. (~ 6 meters, $H_{1/3}$)

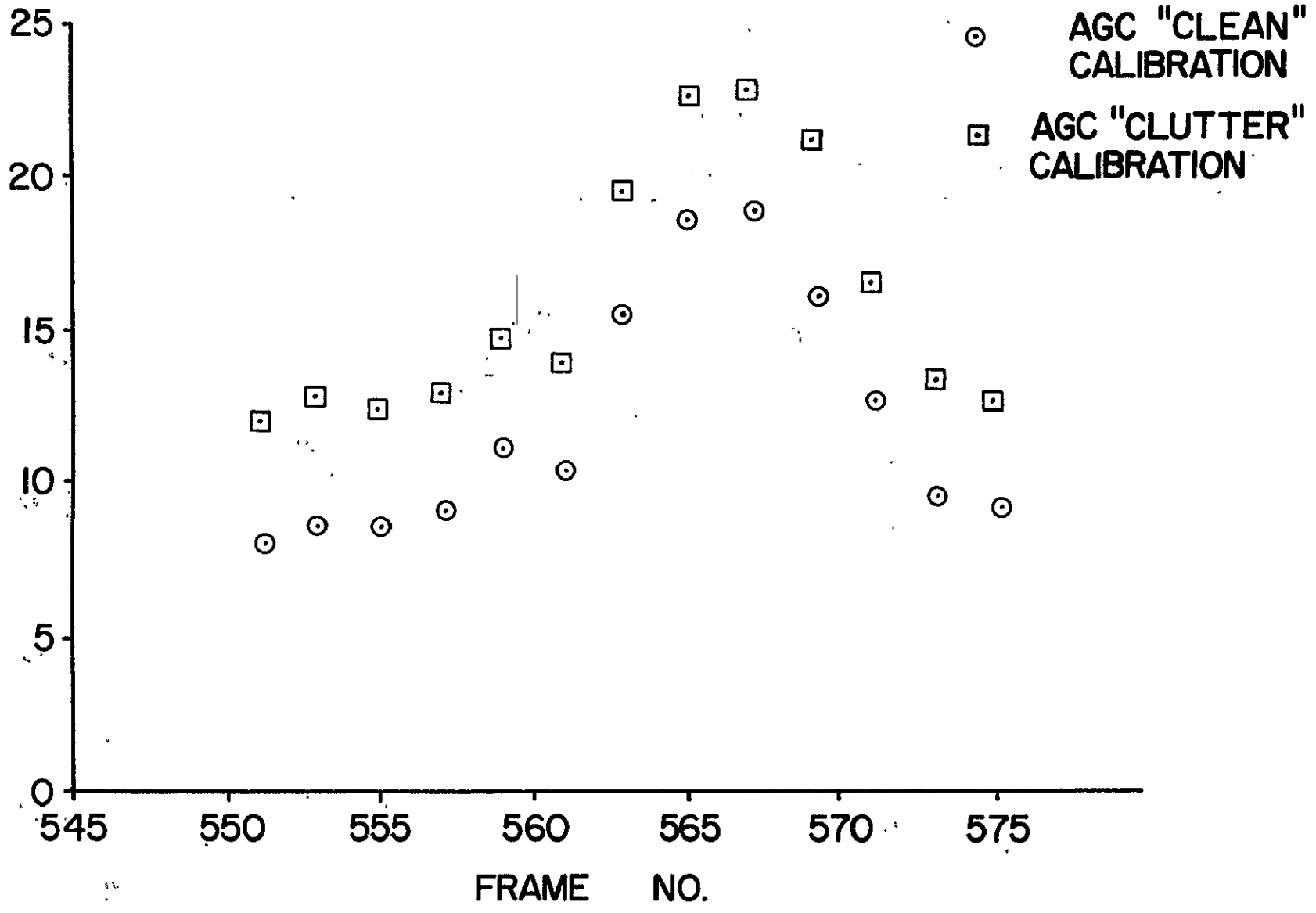

Figure 4.9. Radar cross-section values during a seemingly anomalous AGC period.

5.0 ALTIMETER DATA PROCESSING CONSIDERATIONS

Experience with the GEOS-3 data has shown that preprocessing or data editing is required before optimal filtering procedures can be applied. Automated techniques have been developed which provide for wild-point interpolation and correction and for estimation of residual orbit bias and slope parameters [1]. These parameters are obtained using statistical regression techniques.

Non linear characteristics of the GEOS-3 split-gate tracker have been found to cause negative asymmetries in the altitude data. Figure 5.1 shows altitude data for orbit 2023 over the Gulf of Mexico; this record displays the characteristic negative (or downward) perturbations in the altitude data. Figure 5.2 reproduces a section of the orbit 2023 data on an expanded scale and containing threshold data. The threshold altitude algorithm is seen to essentially remove the altitude disturbances and to indicate that they are hardware-specific in origin. Based on this behavior, and because low data rate telemetry data cannot use the threshold algorithm, computerized edit procedures were implemented to interpolate through such periods.

5.1 Sea State Bias

The term sea state bias has been used to account for any systematic differences between mean value of the geometrical ocean surface and radar sensed mean value. This type of bias is thought to arise due to either the trochoidal shape of ocean waves or the increased occurrence of capillaries on wave peaks compared to wave troughs. Either of these factors could cause an increase in radar cross section per unit area with increasing distance below the wave crests. The direct measurement of this bias term under deep water, long fetch conditions would be extremely difficult. It would require the acquisition of simultaneous waveheight and radar backscatter data of very high

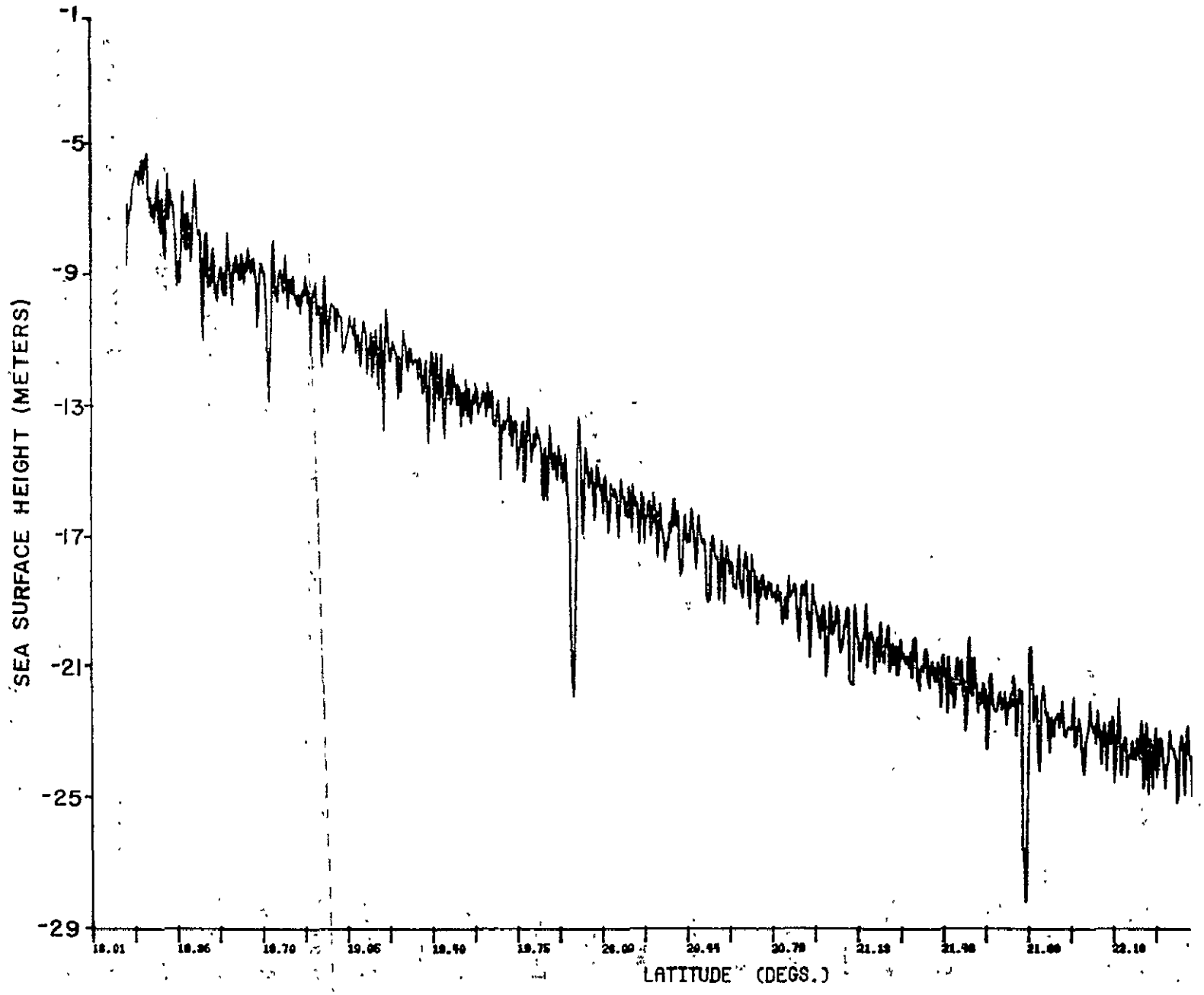

Figure 5.1. Example of non-Gaussian altitude residuals.

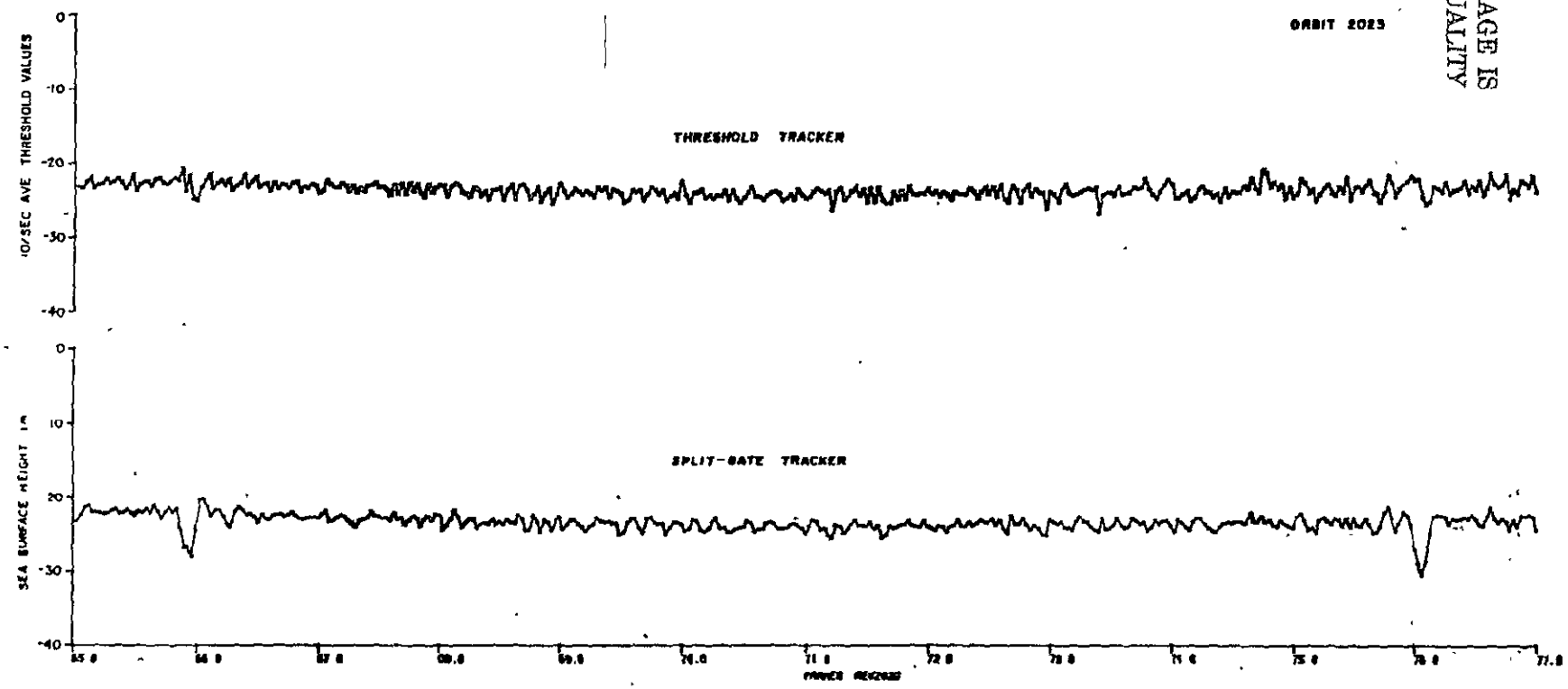

Figure 5.2. Comparison of threshold and split gate tracker data for period shown in previous figure.

absolute and temporal accuracy in mid ocean, under high sea state conditions. The only known instance in which direct measurement has been attempted is the work of Yaplee, et al., reported in 1971 [2]. These measurements, conducted from a tower located off the coast near Norfolk, Va., showed a bias toward the wave troughs of magnitude

$$\Delta t \simeq .17\ H_{1/3} - .31$$

where Δt is the time bias in nanoseconds and $H_{1/3}$ is the significant wave-height in feet. The empirical relationship shows a bias change of ~8 cm for a waveheight change of 1 meter. This degree of bias will be shown to be in general agreement with the bias results to be discussed.

In contrast with the results reported in [2], the sea state bias results to be given below relate to instrument-induced biases as well as ocean surface effects. These instrument biases are primarily caused by changes in the tracker equilibrium point which are in-turn induced by any changes in the received waveshape. Such waveshape changes are caused by variations in:

a. received signal-to-noise ratio, and

b. significant waveheight.

Experimentally measured values of altitude bias as a function of signal-to-noise ratio are in the range of 2.0 ns, see [3]. Bias effects due to pointing angle and significant waveheight cause corresponding changes in the split gate tracker equilibrium point; these effects have been analyzed in [4].

The sea state biases reported here are based on analysis of data from near-overlapping satellite passes. Altimetric data for such passes is first examined and, if necessary, edited to remove data discontinuities and then filtered using a Wiener convolutional algorithm [5]. The ensuing data from several passes is then adjusted in absolute altitude value to provide overlap for the low sea-state portions of the passes. Figure 5.3 shows raw

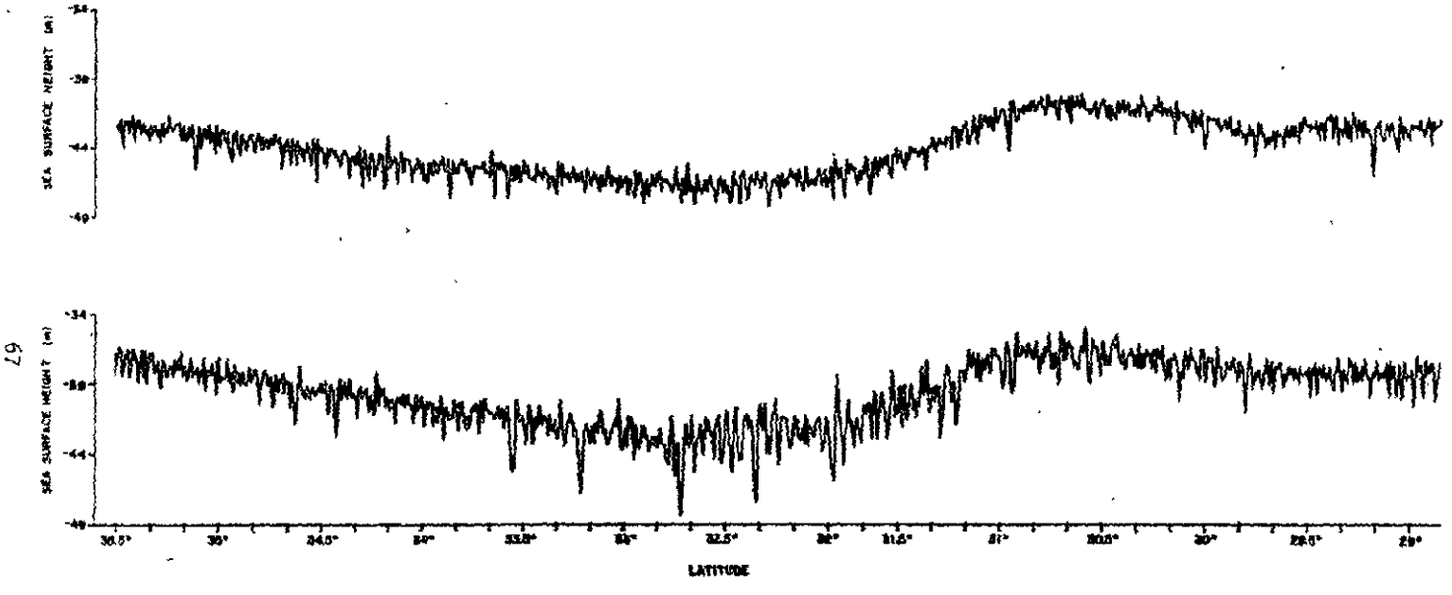

Figure 5.3. Unprocessed sea surface height data for two near-overlapping passes.

altitude data (10/sec) for two passes; orbit numbers 1633 and 6893 for a North Atlantic segment over the latitude and longitude limits shown on the abscissa. Orbit 6893 data comprised the high sea state pass and the data is considerably noisier than orbit 1633 data; however, the permanent geoidal characteristics are seen to exhibit very good repeatability. Figure 5.4 shows both the filtered sea surface height and the sea state data relevant to these data periods. Note in the lower figure that the passes (which have been offset by ~2 meters) show a systematic departure which correlates with the high sea state period shown in the upper figure.

The above analysis technique has been used with a total of five orbits to produce the results shown in Figure 5.5. These results show the altitude measurement to be increased by the presence of high seas; that is, the measured mean-sea-level value is depressed downward due to high seas. Based on the results shown in Figure 5.5, the bias effect increases with increasing significant waveheight ($H_{1/3}$) and is in the order of 10 percent of the $H_{1/3}$ value for 10 meter seas.

5.2 Precipitation Sensitivity

Figure 5.6 gives calculated values of 1) single pulse signal levels and 2) signal-to-noise ratio for one second post detection averaging, both as a function of precipitation level. These results indicate that moderate to heavy precipitation should be detectable in the Global mode. Other considerations, however, indicate that hardware changes would be necessary to implement this capability; the present noise gate is an a-c coupled circuit that does not provide a direct measure of noise power. In the event that the GEOS-3 backup system is used, simple changes in the noise or sampling gates and the AGC loop would permit observation of precipitation return.

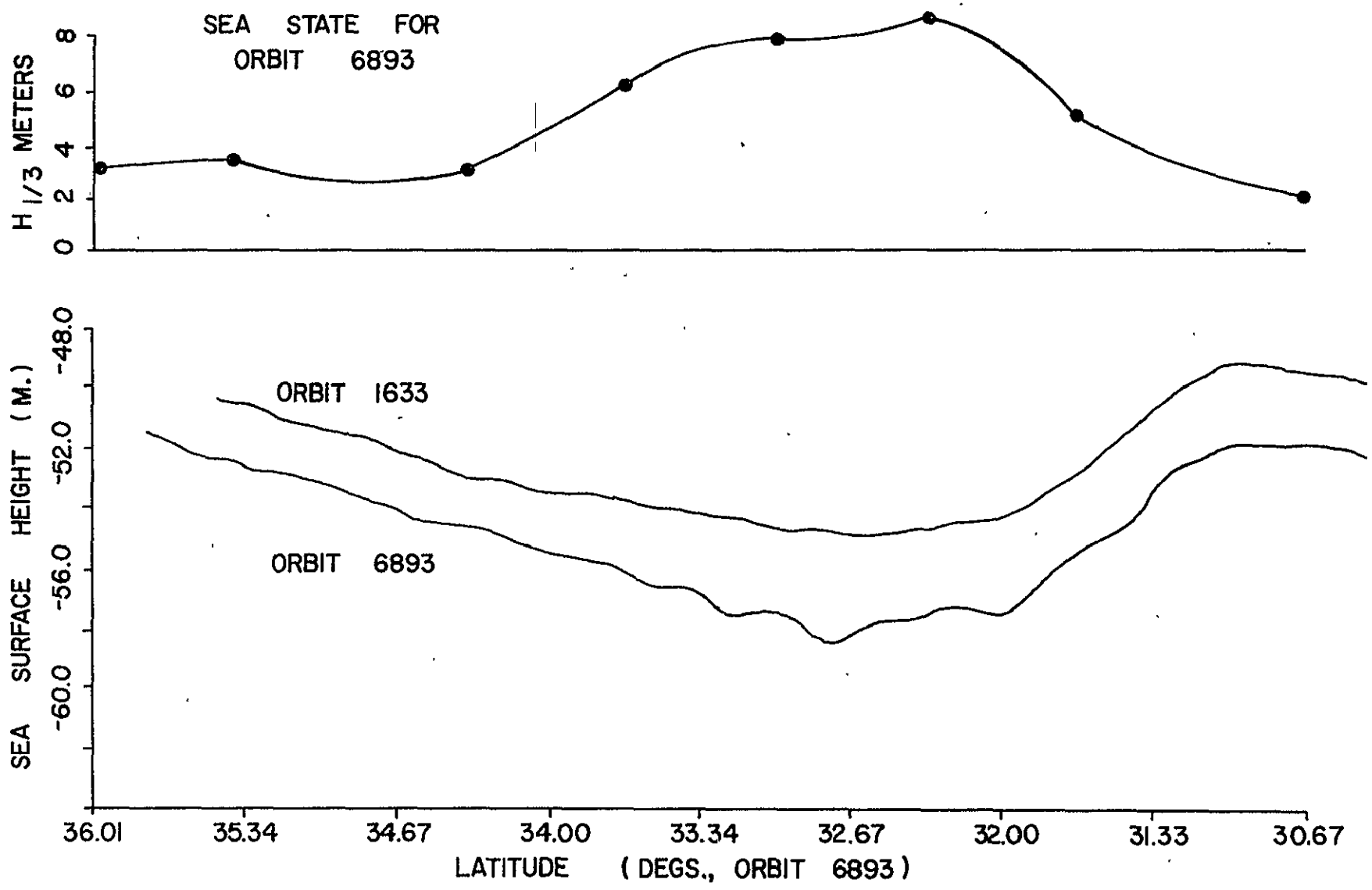

Figure 5.4. Filtered sea surface height and sea state data.

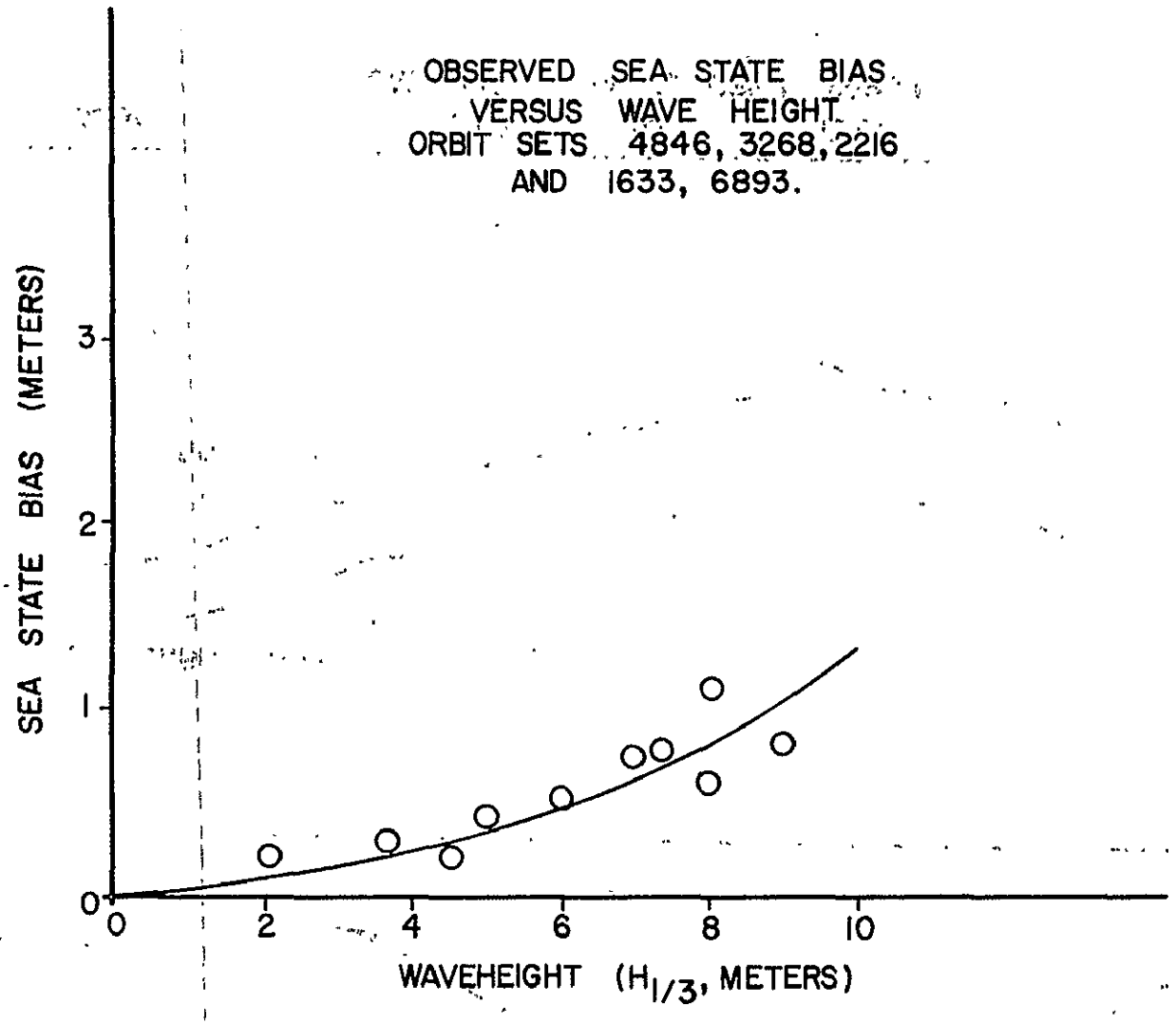

Figure 5.5. Sea state bias results.

GEOS-III Calculated Single-pulse $\bar{P}_r$ (dBm).

	I Mode	G Mode
Light rain (1mm/hr)	-134	-121
Excessive rain (40 mm/hr)	-108	- 96
Nimbostratus cloud	-156	-144
Cirrus cloud	-168	-151

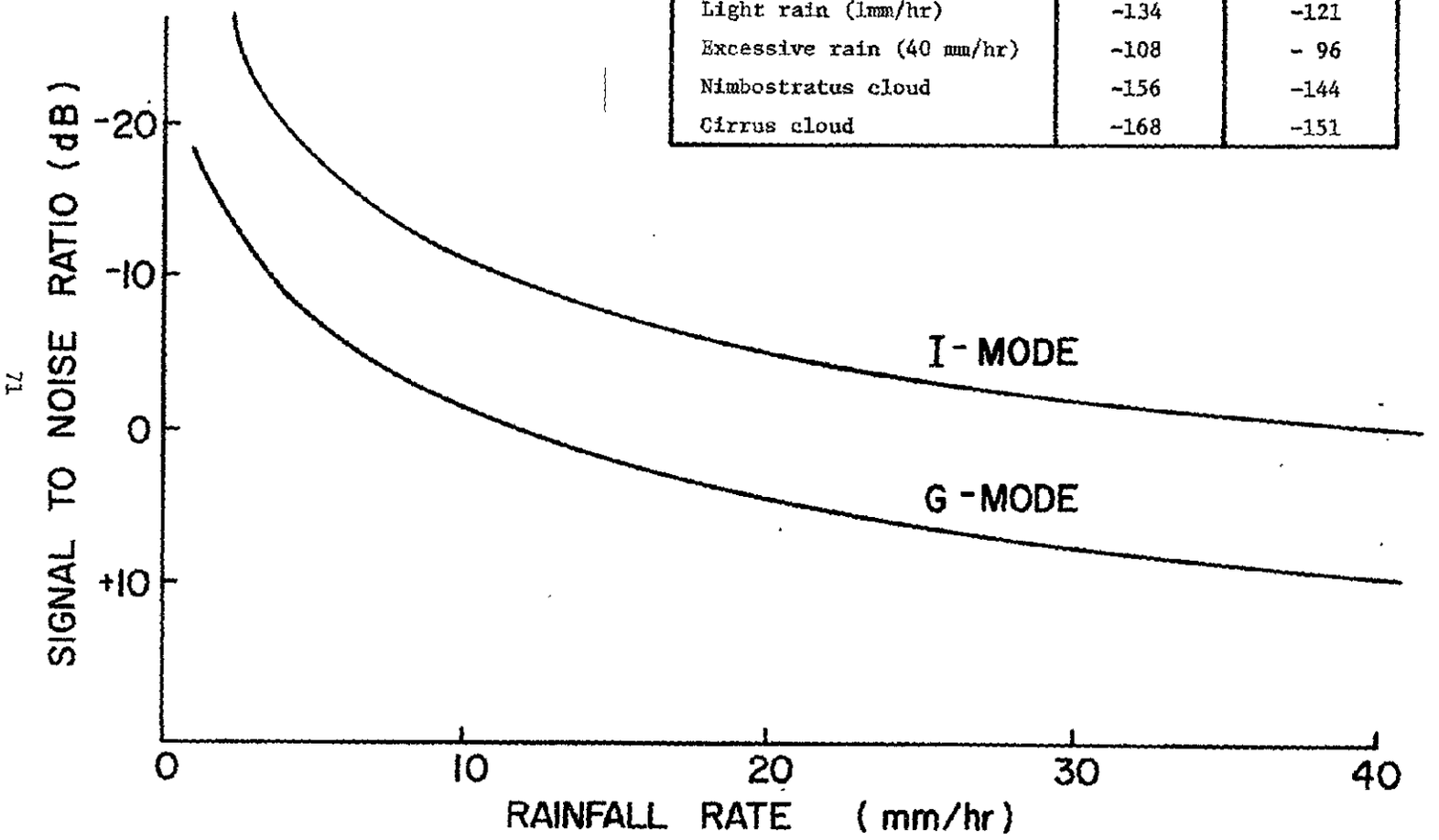

Figure 5.6. Calculated G-Mode and I-Mode received SNR versus rainfall rate for one second post detection integration.

5.3 Waveform Sampler Corrections

The following paragraphs summarize our efforts toward deriving corrections for the sampling gates. The initial approach to this problem was to use BIT/CAL data to identify offset and gain differences between samplers. As discussed below, this approach was not feasible because BIT/CAL offset values did not correlate with data acquisition offset values. The bias-test portion of the BIT/CAL data also showed waveform changes, especially in the $12^{\underline{th}}$ gate values. It is not known whether these were due to sampler effects or changes in transmitter leakage.

The second approach comprised the extraction of offset corrections from fitting an error function to the waveform and gain corrections from the standard-deviation waveform. Two difficulties were experienced in this approach: a study of gate-to-gate covariance indicated that timing differences were also present. In addition, offset corrections derived from the on-board averaged waveforms and the software averaged waveforms were not in agreement. At this point it was decided that gain corrections could not be obtained for the low data rate case; and the approach taken was to obtain offset corrections from the error function fit and timing corrections from the covariance calculations. Shortly after this approach was taken it was learned that E. J. Walsh of WFC had obtained pre-launch timing corrections from G. E. and had derived offset corrections, both of which generally agreed with our results. Our activities were discontinued at this point.

As the results given below show, empirically derived offset corrections appear to be valid to within ~2 m.v. The 2 m.v. uncertainty derives from short term drifts in the offset values.

Figure 5.7 shows graphed values of BIT/CAL and backscattered waveforms for Pass 217. Data from other passes have also been examined and the BIT/CAL

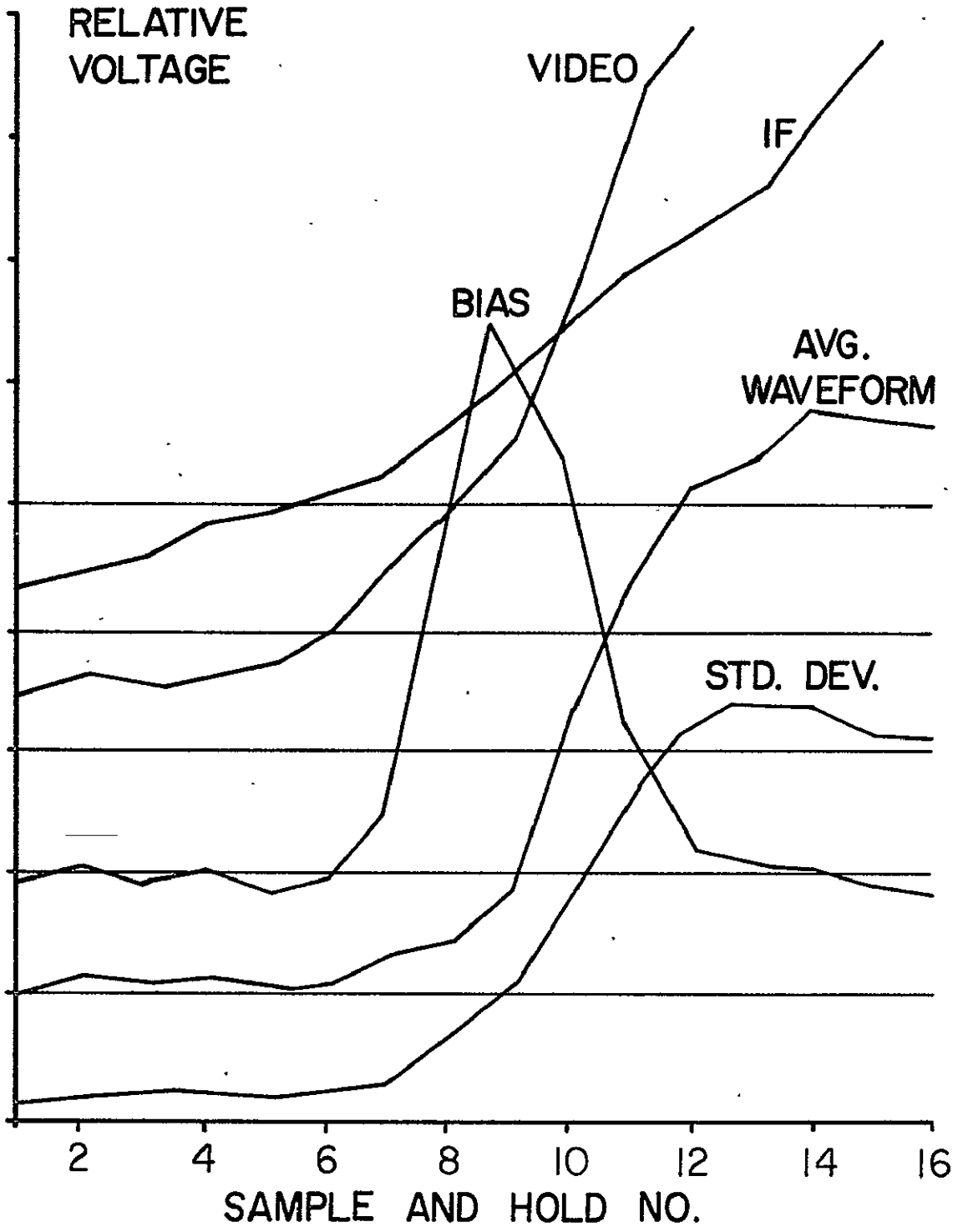

Figure 5.7. Comparison of BIT/CAL and experimental waveforms; Pass 217 (6-Frame average).

waveforms were found to be similar to those shown in Figure 5.7. In this figure the baseline is displaced upward one division for each of the waveshapes shown. The following comments pertain to the data shown in Figure 5.7.

1) The unevenness of the ocean scattered waveshape is much larger than the expected statistical uncertainty. The 6-frame averages contain approximately 1900 samples, therefore, the one-sigma confidence bound should be approximately 2%.
2) There is no clear cut relationship between the noise region sample values for the Bias Test and the experimental waveform.
3) The fact that the IF and video waveforms are locally uneven and the differences between the voltage and standard deviation relative waveshapes suggest that dc biases and gain differences both exist.

Figure 5.8 shows a time-sequence graph of several "noise" or early gates; these results partially explain the lack of agreement in bias values noted above. The upper curve shows per-frame values for ARS-4, which represents the on-board averaged values for the fourth gate. The next three curves show the software averaged values (AW) for gates 1, 2 and 4. These three curves are rather surprising for two reasons: The apparent correlation between gates 2 and 4 is striking; and the correlation with gate 1 is higher than expected. The rate of fluctuation is also much greater than expected; if these off-sets were due to d-c drift, temperature, etc., the fluctuations would be much slower. The lower graph shows AGC values and the largest gate excursion is seen to coincide with the highest AGC value; thus the noise gate values are seen to increase during a period in which they would be expected to show a decrease. The level of correlation present in the gate values

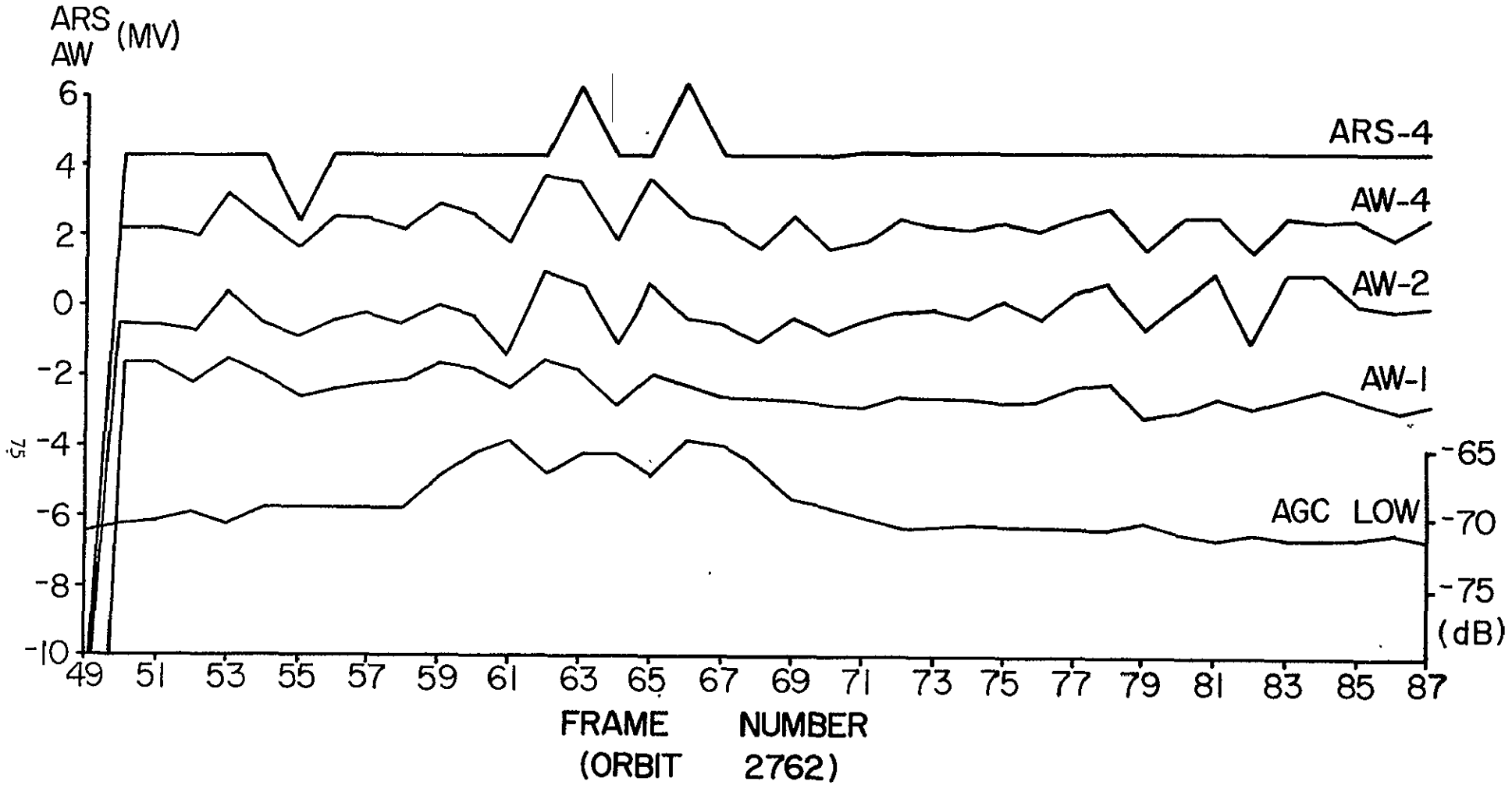

Figure 5.8. Comparison of on-board ARS and software AW averaged gate values with AGC data. (For 320 values of intra-frame data, tape dump showed Gate 2 rms of 4 m.v.)

indicate that the changes are due to system variations rather than signal information. The per-pulse values for one frame were examined and quantization effects were strongly in evidence. The data showed typically 3 step or transition values of ~7 m.v. Inspection of the variances of the per-frame values shows that the quantization distribution is not uniform. Thus the step changes appear to be a slowly-varying effect.

Figure 5.9 shows the computed covariance for the first five gates based on use of the per-pulse values. The signal variability in these gates are largely due to offset drift as depicted by the ~7 m.v. quantization. This figure shows gates 2 and 3 to be much more highly correlated than gates 1 and 2. This implies a wider gate separation in the latter case. Figure 5.10 shows the covariance in the plateau region for two cases. Since gate 14 was selected as the reference gate, the right-left asymmetry in the covariance function is indicative of sample timing differences.

A set of gate spacings were derived by least-squares fitting a Gaussian covariance model to the experimental data; the fit was constrained to require that the sum of the gate spacings approximate the design value (4×6.25 n.s.). The fit obtained is shown in Figure 5.11 and the derived gate spacings were

Gate No.	12	13	14	15	16
Spacing (n.s.)	5	9	5	6.5	

With the exception of the gates 12-13 spacing, these results are in good agreement with Walsh's results (Figure 5.12).

5.4 Tracking Jitter Correlation Properties

Autocorrelation and tracking jitter probability density functions were extracted from the orbit 578 data. Figure 5.13 shows the pre-launch measured

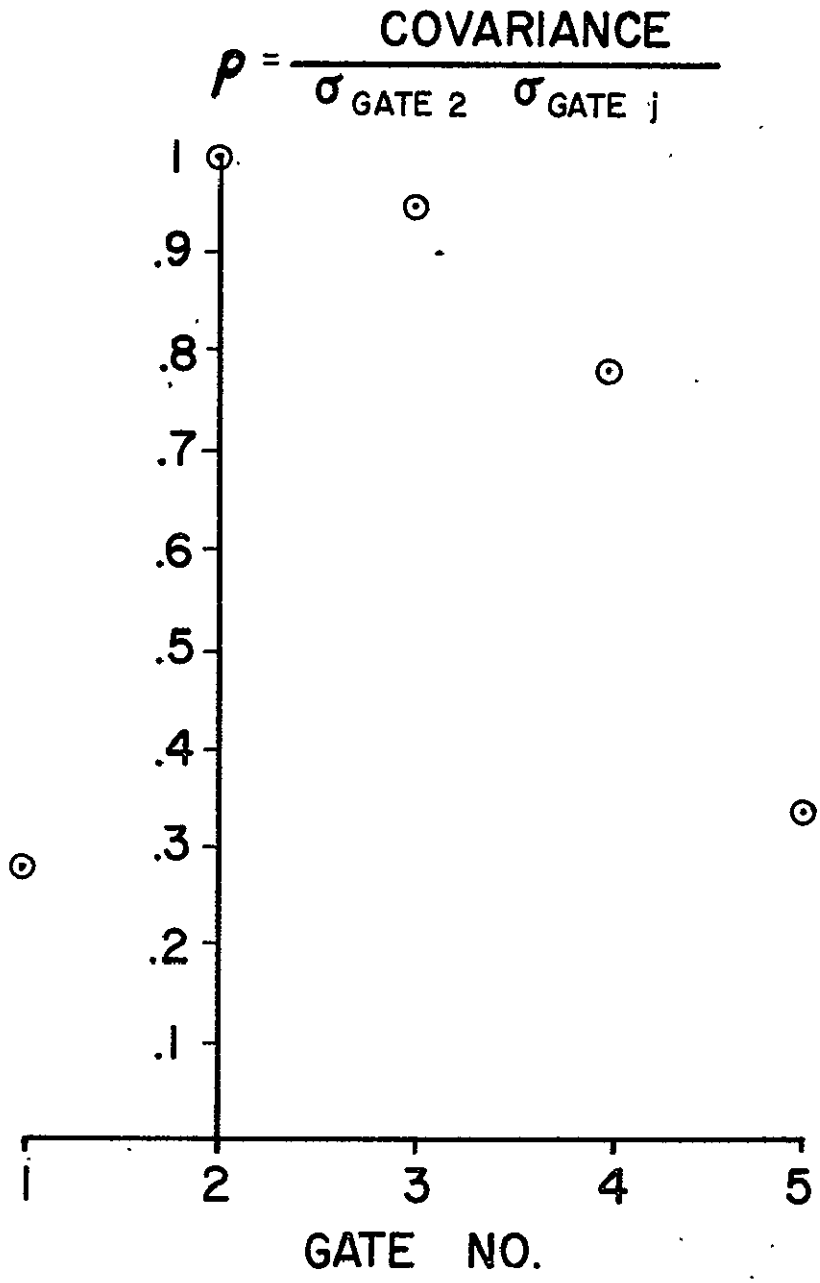

Figure 5.9. Correlation coefficient between Gate 2 and Gates 1-5.

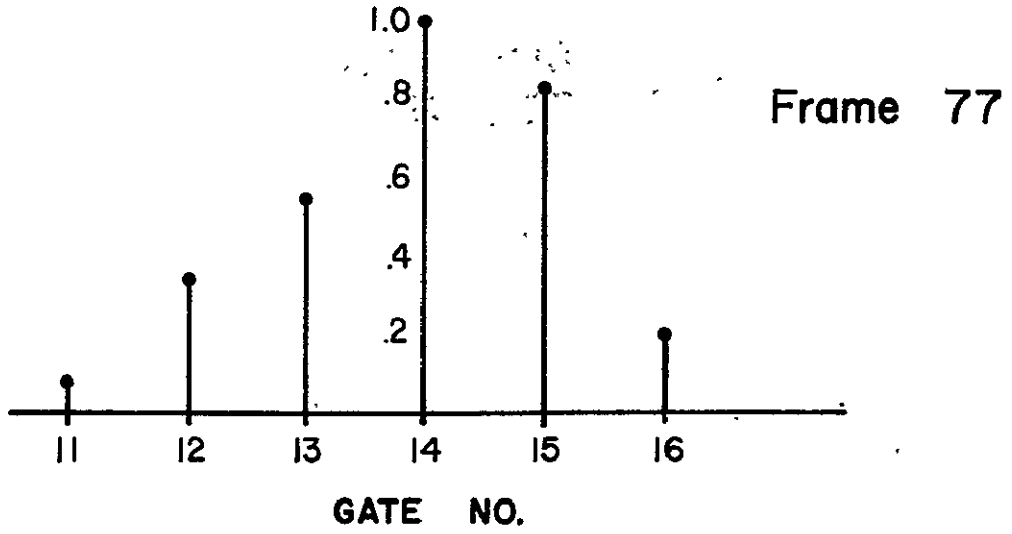

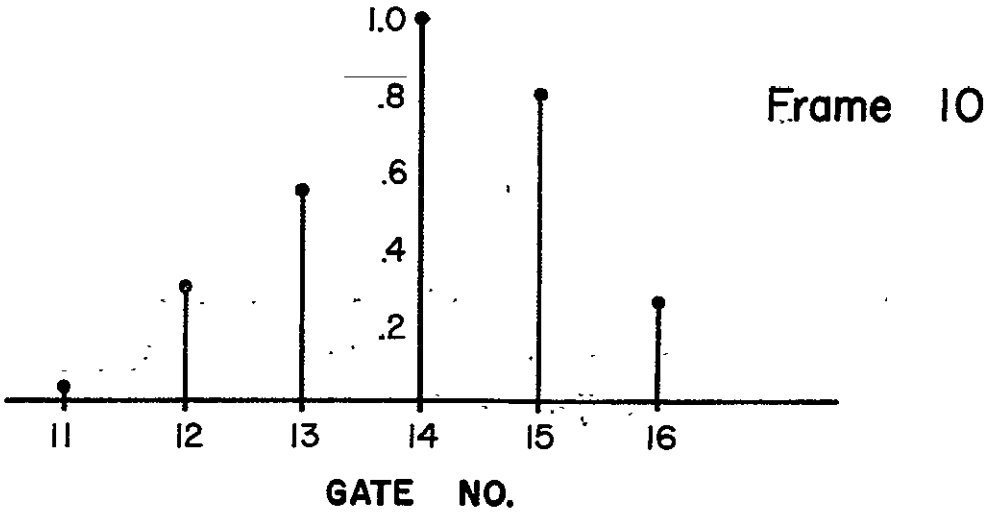

Figure 5.10. Normalized covariance of Gate 14 with Gates 11-16, Rev. 4604.

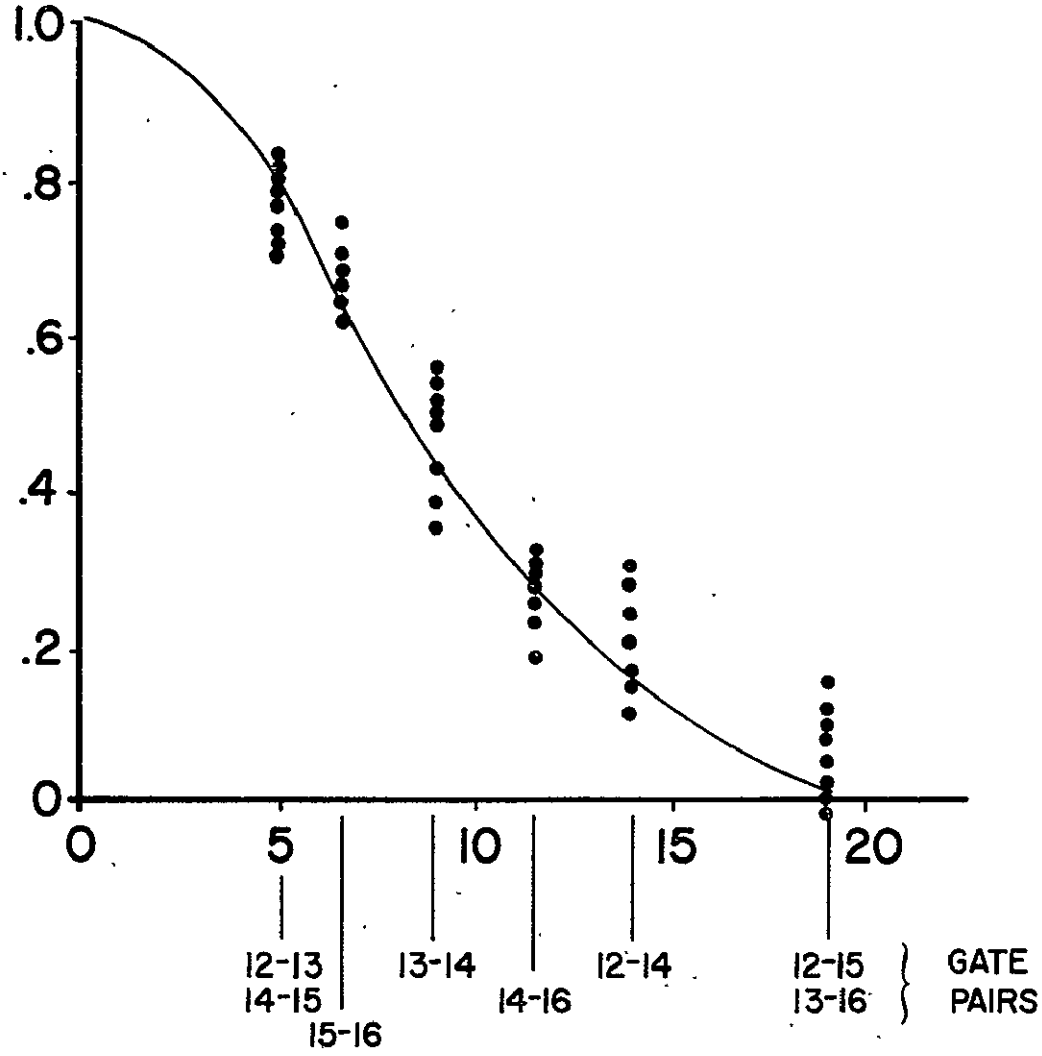

Figure 5.11. Least-squares fit of Gaussian curve to experimental data.

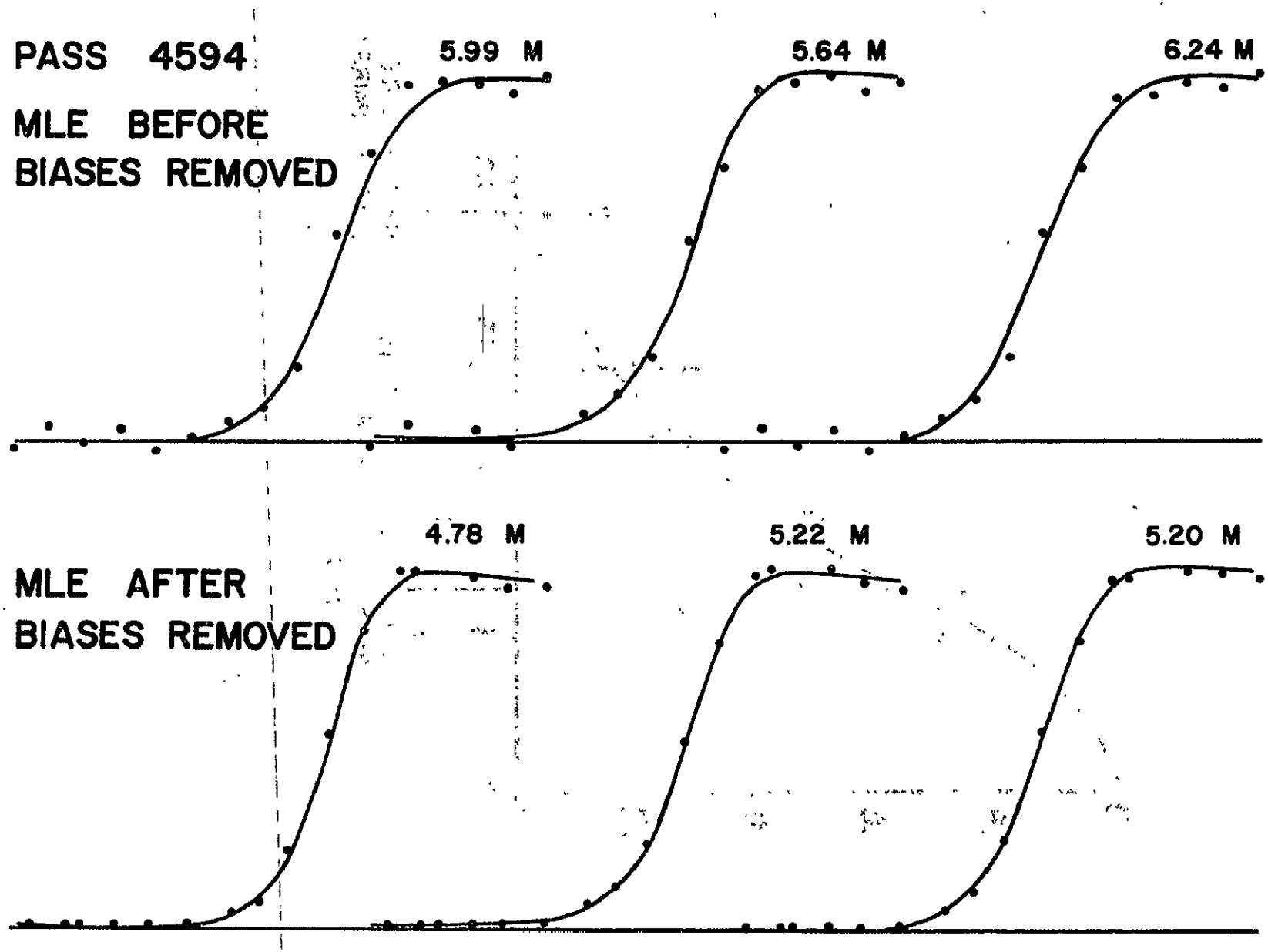

Figure 5.12. Comparison of offset corrected waveforms with uncorrected waveforms. (From Walsh)

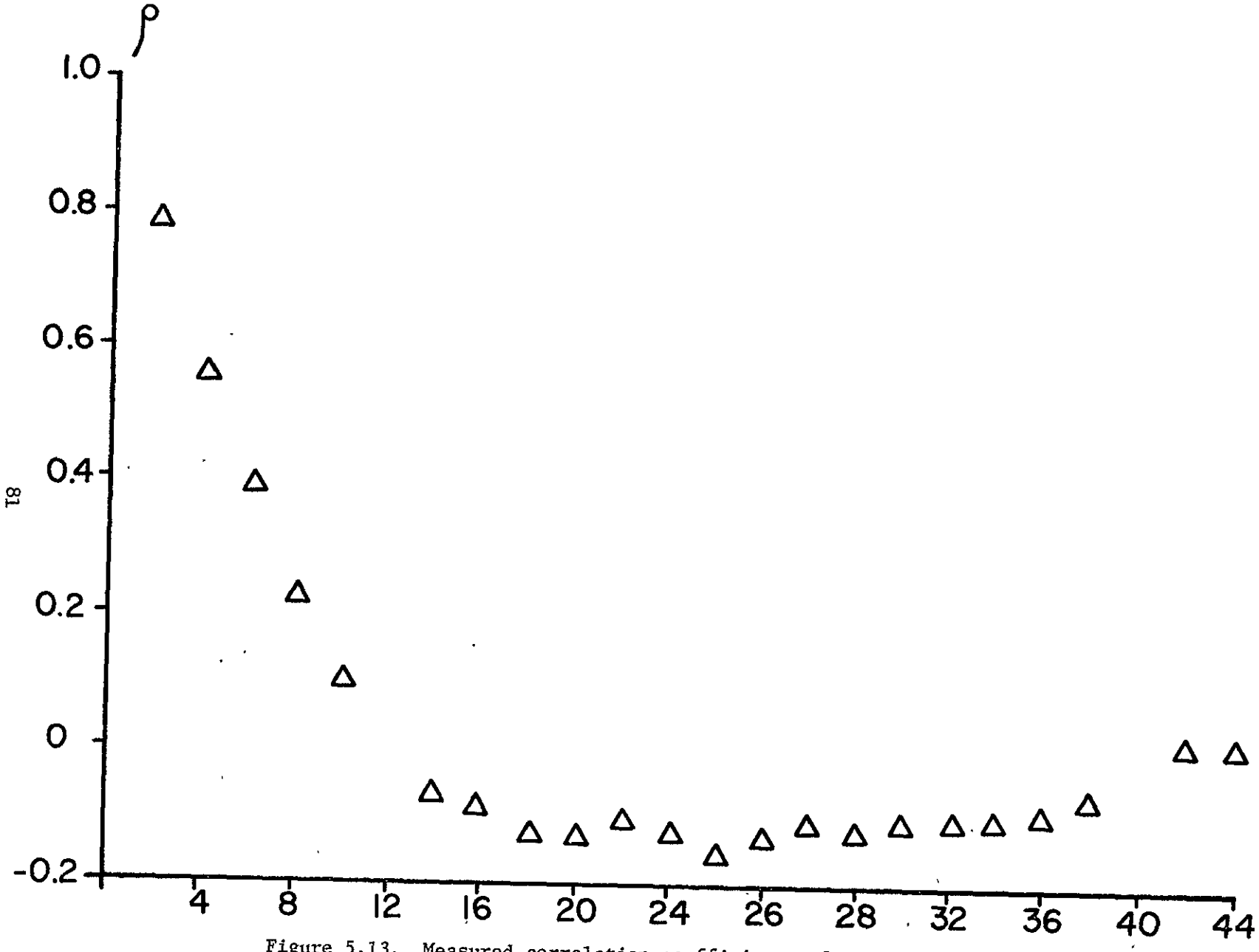

Figure 5.13. Measured correlation coefficients of random tracking error for Intensive Mode with low waveheight ($H_{1/3} = 2$ m.) test signal.

tracking jitter correlation coefficient. Figure 5.14 shows (1) the computed correlation for orbit 578 and (2) the over land correlation for orbit 2236. The agreement between the orbit 578 data and the pre-launch data is quite good; this over-ocean experimental result shows the loop bandwidth to be in the neighborhood of 5 Hz, based on the correlation period shown. The over land result for this data-span shows that the very different mean waveshapes encountered cause the time discriminator characteristic and thus the loop bandwidth to differ substantially from the over ocean values. It should be noted that waveform data for the overland segment of 2236 [2] shows considerable saturation and the tracking loop may be operating non-linearly.

REFERENCES

1. Hayne, G. S.: Unpublished data, 1977.
2. Yaplee, B. S., et al.: "Nanosecond Radar Observations of the Ocean Surface from a Stable Platform," IEEE Trans. Geosc. Elect., Vol. GE-9(7), 1971.
3. Hayne, G. S.; and J. B. Clary: "Initial Test Results Using GEOS-3 Engineering Model Altimeter," NASA CR-141421, Applied Science Associates, Inc., Apex, N. C., 1977.
4. Brown, G. S.; and W. J. Curry: "The Estimation of Pointing Angle and σ° From GEOS-3 Radar Altimeter Measurements," NASA CR-141426, Applied Science Associates, Inc., Apex, N. C., 1977.
5. Miller, L. S.: "Investigation Of The Applications Of GEOS-3 Radar Altimeter Data In Remote Sensing Of Land And Sea Features," NASA CR-141428, Applied Science Associates, Inc., Apex, N. C., 1977.

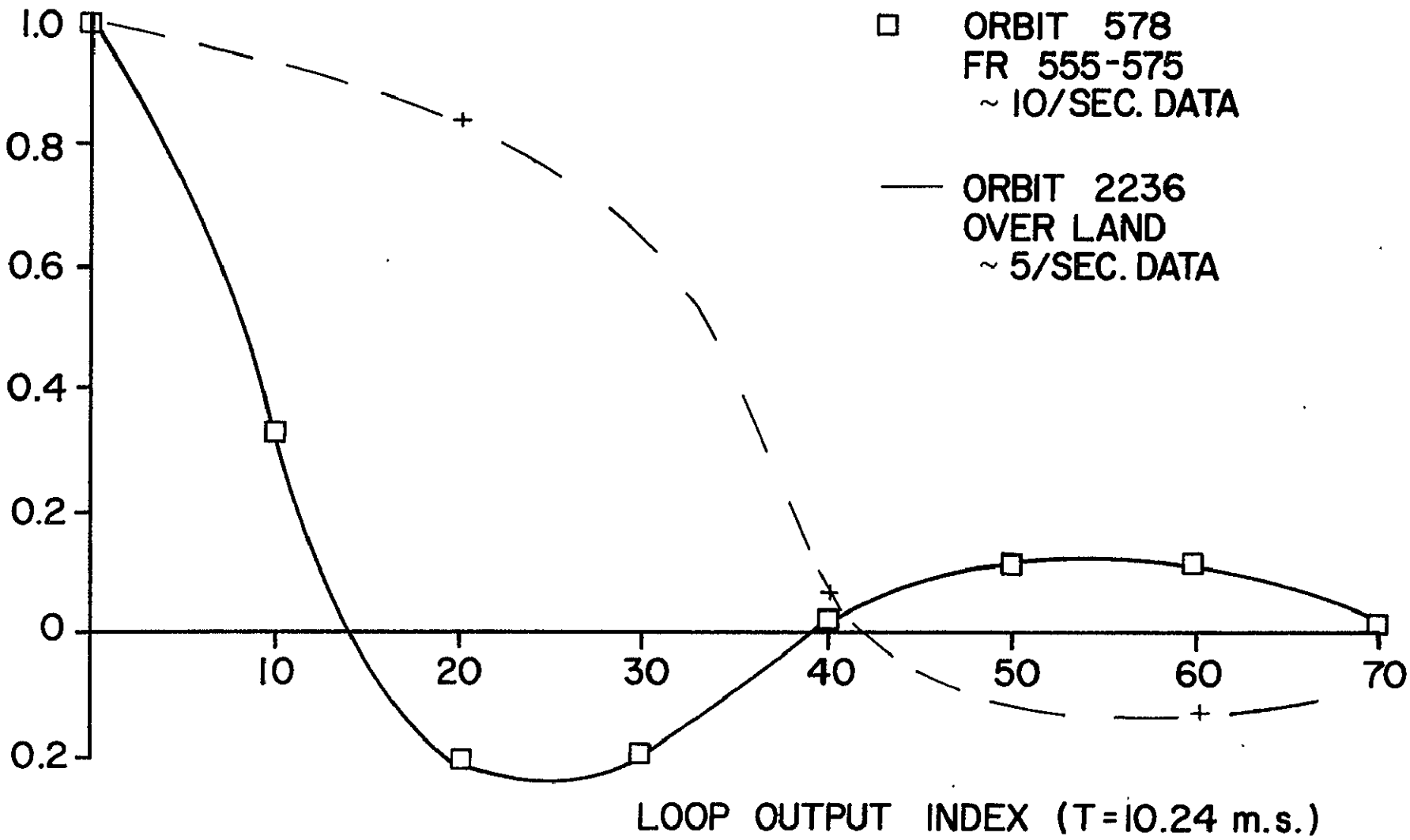

Figure 5.14. Computed correlation coefficients of altitude residuals.

6.0 CONCLUSIONS AND RECOMMENDATIONS

Comparisons between the deconvolution sea state algorithm and the WFC algorithm show good agreement and it is concluded that the WFC algorithm is entirely adequate for GEOS-3 sea state computation. Use of the deconvolution algorithm has shown that extraction of the radar inferred waveheight density function from GEOS-3 data is possible under high sea state conditions. These densities suggest that shorter pulse, higher data-rate sensors (such as the SEA SAT altimeter) will be able to resolve the underlying densities in the low to moderate sea state range. It is recommended that the deconvolution algorithm given herein be utilized with SEA SAT data to investigate the possible improvements in accuracy of sea state estimation compared to algorithms that assume that the received waveshape is strictly an error function form. (Time sidelobe effects on the SEA SAT data should also be considered.)

Both the Cramer Rao error analysis and examination of sea state spatial variability have shown that the achievable sea state resolution is bounded by either Rayleigh noise or by ocean surface inhomogeneity. An averaging period of ~20 seconds is considered to be near-optimum for GEOS-3 data processing.

Comparisons between theoretical σ° values and GEOS-3 observed values have been found to be highly consistent. The "step changes" sometimes observed in σ° data, in areas such as the Gulf Stream, were found to correspond to theoretical values for which the rms surface slope is small. Since surface slope is dominated by waves in the capillary range, such calculations indicate that these σ° changes will occur over either very calm or swell dominated seas. Based on the comparisons given, it is recommended that the "clutter" AGC calibration be used in calculating σ° values.

Data analyses reported herein show a systematic change, or bias, in indicated sea surface height as sea state increases. This change is generally less than 10 percent of the significant waveheight and, as such, is considerably less than orbit errors. Should orbit errors dramatically improve in future systems, this error source should be re-examined.

The presence of d-c biases in the waveform samplers have been found to be a source of difficulty in waveform data processing. Especially frustrating is the apparent inconsistencies between the calibrate and data acquisition indicated biases. In future systems, it is recommended that laboratory studies be conducted to resolve these differences and that use of chopper stabilized circuits be considered.

The GEOS-3 system has proven to be a reliable and versatile satellite system and sensor; consideration should be given to possible use of the back-up hardware system in other remote sensing investigations. Some of the potential uses are as follows:

1. With modifications to the pulse length and repetition rate (~6 ns and 500 per sec.) the sea state resolution could be increased by a factor of 5. With these comparatively inexpensive changes the system could be orbited in conjunction with other Shuttle launches to provide a denser grid of sea state and surface wind data compared to that available from the SEA SAT altimeter. Experience with GEOS-3 has shown that the principal limitation to its sea state measurement capability is in the coverage provided by a single (nadir) sensor.
2. With primarily altitude tracker and AGC modifications the system could be optimized for data acquisition over ice and land areas. Other studies [1] have discussed the usefulness of global ice boundary data and ice sheet topography measurement to NASA climate programs.

3. The addition of a multiple feed structure and possibly a larger antenna would provide wind data over perhaps ± 100 km off nadir. This would yield useful information on surface wind homogeneity and, to some degree, wind direction.

4. All of the above sensor concepts pertain to capabilities of the Intensive Mode. Analyses summarized in this report indicate that minor modification of the Global Mode would permit the acquisition of precipitation data. This capability would thus be incorporated with any of the above system modifications.

In addition to these hardware-specific suggestions, the GEOS-3 program, improving the topographic and sea state measurement capabilities of short pulse altimetry, has demonstrated the greatest deficiency to be that of area coverage. Since finite-swath altimeter concepts have not been forthcoming (for practical antenna sizes), the obvious solution appears to be use of multiple satellites. For sea state measurement only, consideration should be given to sensing techniques other than those requiring short pulse-lengths. Additional studies are needed in these areas.

REFERENCES

[1] Miller, L. S., Brown, G. S. and Priester, R. W.: "A Summary of GEOS-3 Data Studies," Applied Science Associates, Inc., Technical Report, November, 1977.

Appendix A

Computer Program Listing

The results presented in paragraph 2.3 were obtained using the Fortran program which will be described in this appendix. In the attached listing Fortran statements often appear to begin in position 9 rather than the standard position 7. This is a result of the TAB key feature supported by the RT11 TEXT EDITOR in DEC's LSI 11/03 computer. If storage space is a problem, an overlay structure can be used as illustrated in Figure A.1. Such a structure has been used under RT-11 for which TTY I/O is designated by devices 5(input)/7(output) respectively in the listings contained herein. The listing presented in this appendix was used to obtain the results of paragraph 2.4.1; therefore, the attached listing can be used in its present form to obtain $H_{1/3}$ and $\hat{h}(t)$ if $H_{1/3} \geq 4$ m. To use the code as described in paragraph 1.4.2 two changes are required:

(a) In subroutine H13MSR the instruction DATA U1/3Ø*1.Ø
should be used in place of DATA U1/Ø, .25, .5, .75, 26*1./

(b) In subroutine WAVEHT change statement marked with *
(immediately after statement label 9Ø) to read as follows:

```
SWH=DABS(SWH)*SWH-57.Ø
```

An example of executing the code immediately follows the FORTRAN listing and will be described at this time. The input command R H13TST causes the executable code corresponding to the source program to be loaded. The program then requests that NNUM , NDENOM , NINP be input in format 3I3. NNUM = m-1 (where m = order of H(s) numerator polynomial), NDENOM = order of H(s) denominator polynomial), and NINP is an integer which specifies the number of sample gate values which will be input (usually this will be 16 for GEOS-3). Normalized gate samples are printed next. These values are computed from the

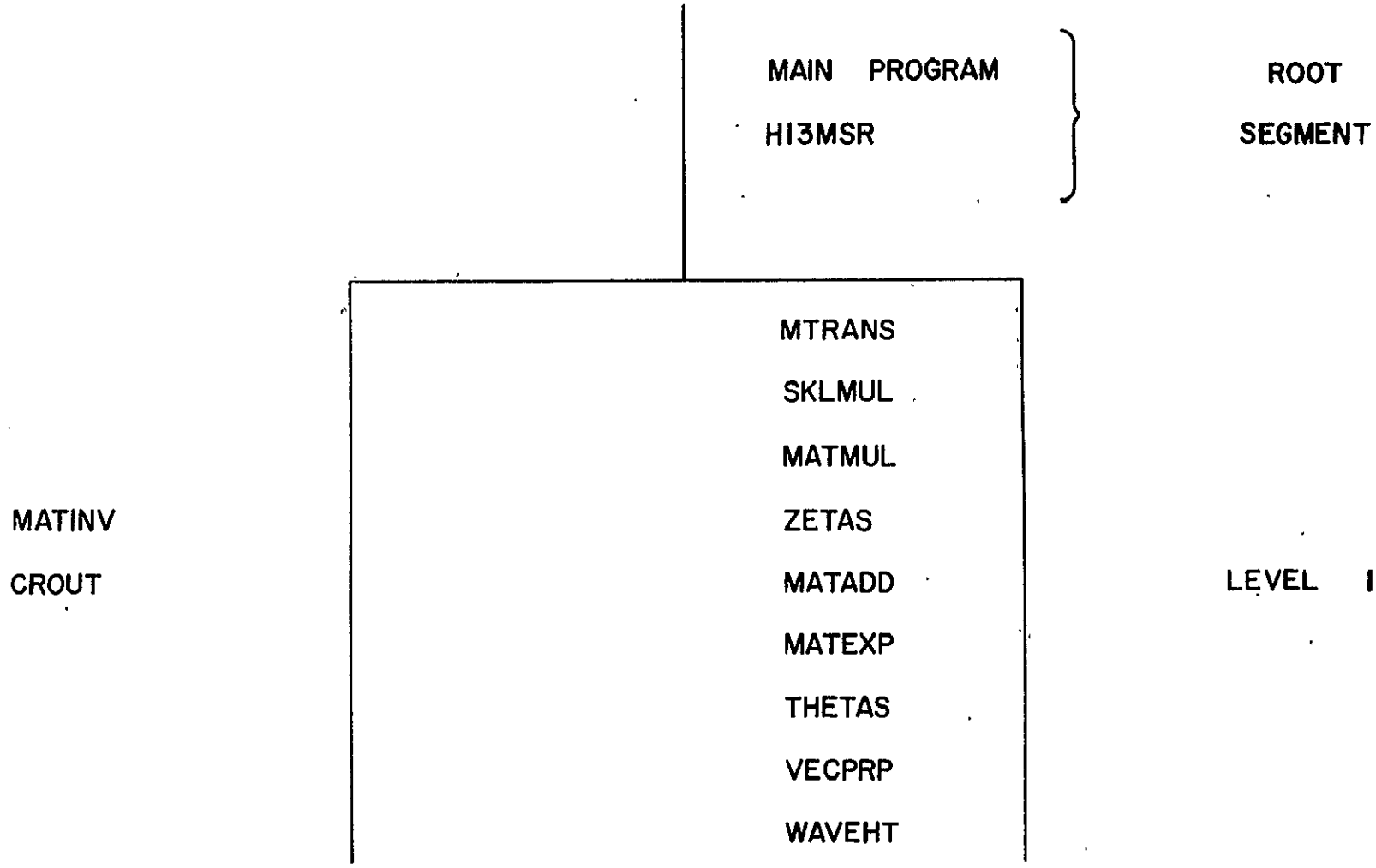

Figure A.1. Overlay structure of Fortran subroutines used to obtain results of paragraph 1.4.

gate samples input earlier as follows:

(a) The average of the first four samples is subtracted from all gate values in order to remove offset effects.

(b) The input set of samples is expanded in number to 25 by padding from NINP to 25. The value inserted is specified by the average of input samples NINP , NINP-1, and NINP-2. This is done in order to enhance the stability of the H(s) identified by the algorithm.

After the identification algorithm has executed successfully, the parameter vector is printed. The parameters are listed in the following order: a_1, a_2, $\ldots a_n$; $-b_1$, $-b_2$,$\ldots$,$-b_n$. Next probability density is output; the numbers printed must be divided by 10. Significant waveheight (SWH), m_2(AT2), m_1(AT), and A(a) are printed on the next line (see paragraph 2.3 for definition of these quantities).

Residuals are defined as input gate values minus model output resulting from identification procedure. The final output is the sum squared error, SSQER.

```
C
C       MAIN PROGRAM
C
        DIMENSION Z(64),TR(64),TH(64)
        DIMENSION COV(144),COVI(144)
        DIMENSION XH(350),XHT(350)
        DOUBLE PRECISION Z,TR,TH,COV,COVI,XH,XHT
        WRITE(7,501)
 501    FORMAT('  INPUT NNUM,NDENOM,NINP-FORMAT 3I3')
        READ(5,500) NNUMER,NDENOM,NINP
        NDATA=25
 500    FORMAT(3I3)
C       NNUMER=ORDER OF N(S)=ZERO IF ONLY CONSTANT IN NUMERATOR
C       NDENOM=ORDER OF DENOMINATOR,MAY BE 2,3,4,OR 5 ONLY
C       NDATA=NO. OF DATA POINTS TO BE PROCESSED
C       NINP=NO. OF GEOS-3 INPUT SAMPLES
        NN=NNUMER
        ND=NDENOM
        NDAT=NDATA
        NPR=NNUMER+NDENOM+1
        NPR=NPR+0
C       Z,TR,TH,XH,XHT,COV,COVI ARE STORAGE AREAS FOR H13MSR
        CALL H13MSR(Z,TR,TH,XH,XHT,COV,COVI,NN,ND,NDAT,NPR,NINP)
        STOP
        END
        SUBROUTINE H13MSR(ZETA,THMAT,THETA,XHAT,XHATT,COV,COVI,NNUMER,NDEN-
     COM,NDATA,NPRAM,NINP)
C       ZETA=MATRIX:(A**(-1)*(THETA-TSTEP*I))
C       THETA=MATRIX:(A**(-1))*(PHI-I)
C       PHI=TRMAT=STATE TRANSITION MATRIX
C       XHAT=MATRIX OF PREDICTED STATE VECTORS
C       XHATT=MATRIX TRANSPOSE OF XHAT
C       THIS PROGRAM ESTIMATES H1/3 FROM 16 GATE SAMPLES
```

```
      DIMENSION P1(8,4),YO(30),YM(30),U(30)
      DIMENSION X1K(8),X1KP1(8),X2K(8),X2KP1(8)
      DIMENSION PBACK(8),XII(30),BIGY(30),ERV(30),P(12),YSOL(12)
      DIMENSION COV(NPRAM,NPRAM),COVI(NPRAM,NPRAM)
      DIMENSION THETA(NDENOM,NDENOM),ZETA(NDENOM,NDENOM)
      DIMENSION TRMAT(NDENOM,NDENOM)
      DIMENSION D1(64),D2(64),D3(64)
      DIMENSION Y(30),U1(30)
      DIMENSION PROB(30)
C     D1,D2,D3 ARE TEMP. STORAGE FOR MATRICES COMPUTED IN SUB-ROUTINES
C     THETAS USES C=D1,AINV=D2
C     MATEXP USES DM=D1,FM=D2,XMAT=D3
      DIMENSION XHAT(NDATA,NPRAM),XHATT(NPRAM,NDATA)
      DOUBLE PRECISION ZETA,TRMAT,THETA,XHAT,XHATT,COV,COVI
      DOUBLE PRECISION YO,YM,U,X1K,X1KP1,X2K,X2KP1,PBACK,XII
      DOUBLE PRECISION BIGY,ERV,P,YSOL,D1,D2,D3,YBAR,SSQER
      DOUBLE PRECISION SSQERB,TSTEP,EPS1,EPS3,FAC
      DOUBLE PRECISION ERCHK,DU,DY
      DOUBLE PRECISION XEXP,YHI
      DOUBLE PRECISION SWH,AT2,AT,A
C     SET UP INPUT FUNCTION
C     DATA U1/0.,.0288,.1955,.5000,.8045,.9712,24*1./
C     DATA U1/30*1.0/
      DATA U1/0.,.25,.5,.75,26*1./
C     DEFINE INITIAL ESTIMATES OF PARAMETER VECTOR
      DATA P1/3.,3.,6*0.,15.,15.,6.,5*0.,105.,105.,45.,10.,4*0.,945.,945
     +.,420.,105.,15.,3*0./
C     READ GEOS GATE SAMPLES
      WRITE(7,500)
 500  FORMAT(' INPUT GATE SAMPLES'/5('     .      '))
      READ(5,501)(Y(I),I=1,NINP)
 501  FORMAT(5F10.5)
      DO 5 I=1,NDATA
 5    U(I)=DBLE(U1(I))
      DO 6 I=1,NINP
```

```
 6      YO(I)=DBLE(Y(I))
C       PREPROCESS INPUT DATA SAMPLES
       YBAR=YO(1)+YO(2)+YO(3)+YO(4)
       YBAR=YBAR/4.
C       SUBTRACT OUT YBAR
       DO 10 I=1,NINP
       YO(I)=YO(I)-YBAR
 10    CONTINUE
       YHI=YO(NINP)+YO(NINP-1)+YO(NINP-2)
       YHI=YHI/3.
       NINP1=NINP+1
       DO 11 I=NINP1,NDATA
 11    YO(I)=YHI
       WRITE(7,800)
 800   FORMAT('   NORMALIZED GATE SAMPLES
       WRITE(7,801)(YO(I),I=1,NDATA)
 801   FORMAT(8F8.4)
       YO(NDATA+1)=YO(NDATA)
C       YO VALUES NOW REPRESENT UN-NORMALIZED PROB - DISTRIBUTION
       SSQERB=0.
       TSTEP=.1
       NMODE=20
       EPS1=1.D-13
       EPS3=1.D-13
C       APPLY SCALINGS TO SELECTED P-VECTOR AND INITIALIZE ESTIMATE
C       VECTOR
       FAC=2.
       DO 12 I=1,NDENOM
       IEXP=NDENOM+1-I
       INDX=NNUMER+1+I
       ININDX=NDENOM-1
       P(INDX)=DBLE(P1(I,ININDX))*((FAC)**IEXP)
       P(INDX)=-P(INDX)
       IF(I.LE.NNUMER+1) P(I)=0.
 12    CONTINUE
C       INITIALIZE BACK-VALUED P-VECTOR
```

```
      DO 36 I=1,NDENOM
      II=I+NNUMER+1
      PBACK(I)=P(II)
 36   CONTINUE
C     TEST FOR MONOTICITY OF YO
      NOSW=0
      DO 15 I=6,NDATA
      IF(YO(I).GT.YO(I+1)) NOSW=NOSW+1
 15   CONTINUE
C     NOSW=NO. OF TIMES THAT CURVE WAS DECREASING
      ITERNO=0
C     *********THIS IS MAIN LOOP POINT**********
      DO 150 ILOOP=1,16
      ITERNO=ITERNO+1
C     DECIDE IF MODEL (YM) OUTPUT OR EXPERIMENT (YO) OUTPUT SHOULD
C     BE USED IN COMPUTATIONS
      IF(ITERNO.GE.NMODE) GO TO 30
C     DON'T USE MODEL OUTPUT YET
      NDATP1=NDATA+1
      DO 25 I=1,NDATP1
      YM(I)=YO(I)
 25   CONTINUE
 30   CONTINUE
C     DO 35 I=1,NDENOM
C     X1K(I)=0.
C     X1KP1(I)=0.
C     X2K(I)=0.
C     X2KP1(I)=0.
C 35  CONTINUE
C     COMPUTE TRANSITION MATRIX
      CALL MATEXP(TRMAT,P,TSTEP,NDENOM,NNUMER,NPRAM,D1,D2,D3)
C     COMPUTE THETA FOR H(S) SUB-I
      CALL THETAS(THETA,P,TRMAT,NDENOM,NNUMER,NPRAM,D1,D2)
C     COMPUTE ZETA FOR H(S) SUB-I
      CALL ZETAS(ZETA,P,THETA,TSTEP,NDENOM,NNUMER,NPRAM,D1,D2)
      JXK=1
```

```
C       SKIP PROPAGATION AFTER 1ST ITERATION
        IF(ITERNO.GT.1) GO TO 39
C       NOW CALL VECPRP TO PROPAGATE STATE AND FORM XHAT
        CALL VECPRP(XHAT,BIGY,X1K,X2K,X1KP1,X2KP1,TRMAT,THETA,ZETA,U,YM,YO
     +,TSTEP,XII,P,NNUMER,NDENOM,NDATA)
 39     CONTINUE
C       NOW HAVE X-OVERBAR,UNDERBAR AND YO+ X-SUBII VECTOR
C       SOLVE FOR UPDATED P-VECTOR
C       LEAST SQ. FIT FOR P-VECTOR
C       TRANSPOSE XHAT
        CALL MTRANS(XHATT,XHAT,NDATA,NPRAM)
C       COV=XHATT*XHAT
        CALL MATMUL(COV,XHATT,XHAT,NPRAM,NDATA,NPRAM)
C       COVI=INVERSE(COV)
        CALL MATINV(NPRAM,COV,EPS1,EPS3,COVI)
C       XHAT*BIGY REQUIRED TO GET P-VECTOR
        CALL MATMUL(YSOL,XHATT,BIGY,NPRAM,NDATA,JXK)
C       NOW READY FOR P-VECTOR
C       SAVE P-VECTOR IN PBACK BEFORE GETTING NEW P-VECTOR
        DO 41 I=1,NDENOM
        II=I+NNUMER+1
        PBACK(I)=P(II)
 41     CONTINUE
        CALL MATMUL(P,COVI,YSOL,NPRAM,NPRAM,JXK)
C       COMPUTE: ERROR VECTOR(ERV),AND SUM SQ. ERROR(SSQER)
C       NOW PREPARE TO COMPUTE MODEL OUTPUT , YM-USE NEW P-VEC
        CALL MATEXP(TRMAT,P,TSTEP,NDENOM,NNUMER,NPRAM,D1,D2,D3)
        CALL THETAS(THETA,P,TRMAT,NDENOM,NNUMER,NPRAM,D1,D2)
        CALL ZETAS(ZETA,P,THETA,TSTEP,NDENOM,NNUMER,NPRAM,D1,D2)
C       NOW USE VECPRP TO GET XHAT
        CALL VECPRP(XHAT,BIGY,X1K,X2K,X1KP1,X2KP1,TRMAT,THETA,ZETA,U,YM,Ø
     +,TSTEP,XII,P,NNUMER,NDENOM,NDATA)
C       COMPUTE YM FOR POSSIBLE USE ON NEXT ITERATION
        DO 90 K=1,NDATA
        YM(K)=Ø.
        DO 100 I=1,NPRAM
```

```
      YM(K)=YM(K)+XHAT(K,I)*P(I)
 100  CONTINUE
      DO 110 I=1,NDENOM
      II=NNUMER+1+I
      YM(K)=YM(K)-XHAT(K,II)*PBACK(I)
 110  CONTINUE
 90   CONTINUE
      YM(NDATA+1)=YM(NDATA)
C     COMPUTE SUM SQUARED ERROR
      SSQER=0.
      DO 120 K=1,NDATA
      ERV(K)=YO(K)-YM(K)
 120  SSQER=SSQER+ERV(K)*ERV(K)
C     WRITE(7,990)((P(I),I=1,NPRAM),SSQER)
      NOINT=NINP-1
      CALL WAVEHT(SWH,AT2,AT,A,P,TSTEP,NOINT,TRMAT,THETA,D2,ZETA,D1,D3,P
     +ROB,NNUMER,NDENOM,NPRAM,NDATA)
C     WRITE(7,505)(SWH,AT2,AT,A)
 505  FORMAT(4F15.8)
 990  FORMAT(6F12.4)
C     *********TEST FOR STOPPING CONDITIONS **********
C     STOP WHEN SSQER BECOMES CONSTANT OR WHEN ITERNO>16
C     FIRST CHECK FOR CONVERGENCE,THEN FOR ITERATION LIMIT
      ERCHK=SSQER-SSQERB
      ERCHK=DABS(ERCHK)
      SSQERB=SSQER
      IF(ERCHK.LE.1.D-03) GO TO 200
      IF(ITERNO.GT.15) GO TO 250
 150  CONTINUE
 200  WRITE(7,400)
 400  FORMAT(/'   H(S) PARAMETER VECTOR')
      WRITE(7,401)(P(I),I=1,NPRAM)
 401  FORMAT(6F12.4)
      WRITE(7,989)
 989  FORMAT('  PROB. DENSITY ')
      WRITE(7,990)(PROB(I),I=1,NDATA)
```


C-3

```
      WRITE(7,988)
 988  FORMAT('  SWH=,AT2=,AT=,A=: ')
      WRITE(7,505)(SWH,AT2,AT,A)
      WRITE(7,402)
 402  FORMAT(//' RESIDUALS ')
      WRITE(7,401)(ERV(I),I=1,NDATA)
      WRITE(7,403) SSQER
      GO TO 450
 403  FORMAT(//'  SSQER='F12.8)
 250  WRITE(7,410)
      GO TO 450
 420  WRITE(7,503)
 503  FORMAT(///'  CHECK INPUT DATA,H13 COMP. NOT ATTEMPTED')
 410  FORMAT(//'-   *****DIVERGENCE*****')
 450  CONTINUE
      RETURN
      END
*
```

```
      SUBROUTINE MTRANS(B,A,IRA,ICA)
C     RETURNS TRANSPOSE(A) IN B
C     IRA=#ROWS IN A
C     ICA=#COLS. IN A
      DIMENSION A(IRA,ICA),B(ICA,IRA)
      DOUBLE PRECISION A,B
      DO 5 I=1,IRA
      DO 5 J=1,ICA
      B(J,I)=A(I,J)
 5    CONTINUE
      RETURN
      END
      SUBROUTINE SKLMUL(B,A,FACTOR,IRA,ICA)
C     MULTIPLY A BY SCALAR=FACTOR,RETURN IN B
      DIMENSION B(IRA,ICA),A(IRA,ICA)
      DOUBLE PRECISION B,A,FACTOR
      DO 5 I=1,IRA
      DO 5 J=1,ICA
      B(I,J)=FACTOR*A(I,J)
 5    CONTINUE
      RETURN
      END


      SUBROUTINE MATMUL(C,A,B,IRA,ICRAB,ICB)
C     THIS ROUTINE COMPUTES A*B AND RETURNS IN C
C     IRA=ROWS IN A
C     ICRAB=#COLS. IN A,# ROWS IN B
C     ICB=# COLS. IN B
      DIMENSION A(IRA,ICRAB),B(ICRAB,ICB),C(IRA,ICB)
      DOUBLE PRECISION A,B,C
      DO 5 I=1,IRA
      DO 5 J=1,ICB
      C(I,J)=0.
      DO 5 K=1,ICRAB
      C(I,J)=C(I,J)+A(I,K)*B(K,J)
 5    CONTINUE
      RETURN
      END
```

```
      SUBROUTINE ZETAS(ZETA,P,THETA,TSTEP,NDENOM,NNUMER,NPRAM,C,AINV)
C     THIS ROUTINE COMPUTES ZETA=AINV*(THETA-TSTEP*I)
      DIMENSION THETA(NDENOM,NDENOM),P(NPRAM),ZETA(NDENOM,NDENOM)
      DIMENSION C(NDENOM,NDENOM),AINV(NDENOM,NDENOM)
      DOUBLE PRECISION ZETA,P,THETA,TSTEP,C,AINV
      NDENO=NDENOM
      DO 5 I=1,NDENOM
      DO 5 J=1,NDENOM
      C(I,J)=THETA(I,J)
      IF(I.EQ.J) C(I,J)=C(I,J)-TSTEP
C     SET UP AINV FROM P-VECTOR
      AINV(I,J)=0.
      IM=I-1
      IF(IM.EQ.J) AINV(I,J)=1.
      NPICK=NNUMER+1
      NSEL=NPICK+J+1
      IF(J.EQ.NDENOM) GO TO 5
      IF(I.EQ.1) AINV(I,J)=-P(NSEL)/P(NPICK+1)
 5    CONTINUE
      AINV(1,NDENOM)=1./P(NPICK+1)
C     NOW COMPUTE ZETA
      CALL MATMUL(ZETA,AINV,C,NDENO,NDENO,NDENO)
      RETURN
      END

      SUBROUTINE MATADD(C,A,B,IRA,ICA)
C     ADD A TO B,RETURN IN C
      DIMENSION A(IRA,ICA),B(IRA,ICA),C(IRA,ICA)
      DOUBLE PRECISION C,A,B
      DO 5 I=1,IRA
      DO 5 J=1,ICA
      C(I,J)=A(I,J)+B(I,J)
 5    CONTINUE
      RETURN
      END
```

```
      SUBROUTINE MATEXP(TRMAT,P,TSTEP,NDENOM,NNUMER,NPRAM,DM,FM,XMAT)
C     THIS ROUTINE COMPUTES MATRIX EXPONENTIAL-(A*TSTEP)
C     TSTEP=TIME STEP SIZE
C     NDENOM=ORDER OF SQUARE MATRIX
      DIMENSION TRMAT(NDENOM,NDENOM),P(NPRAM)
      DIMENSION DM(NDENOM,NDENOM),FM(NDENOM,NDENOM)
      DIMENSION XMAT(NDENOM,NDENOM)
      DOUBLE PRECISION TRMAT,P,TSTEP,DM,FM,XMAT,TSPRME,DIVFAC
C     INITIALIZE AS FOLLOWS:
C     TRMAT TO IDENTITY MATRIX
C     DM = TRMAT
C     FM = FORMED FROM DENOMINATOR TERMS IN P-VECTOR
      TSPRME=TSTEP/256.
      DO 5 I=1,NDENOM
      DO 5 J=1,NDENOM
      IF(I.EQ.J) TRMAT(I,J)=1.
      IF(I.NE.J) TRMAT(I,J)=0.
      DM(I,J)=TRMAT(I,J)
      FM(I,J)=0.
      JJ=NNUMER+1+J
      IP1=I+1
      IF(I.EQ.NDENOM) FM(I,J)=P(JJ)*TSPRME
      IF(IP1.EQ.J) FM(I,J)=TSPRME
 5    CONTINUE
      NDENO=NDENOM
C     COMPUTE POWERS OF ARGUMENT MATRIX FM AND ACCUMULATE INTO TRMAT
C     RECAL THAT TRMAT IS INITIALIZED TO I-MATRIX
      DO 10 I=1,10
      CALL MATMUL(XMAT,DM,FM,NDENO,NDENO,NDENO)
      DO 15 II=1,NDENOM
      DO 15 JJ=1,NDENOM
      DM(II,JJ)=XMAT(II,JJ)
 15   CONTINUE
      TEMP=FLOAT(I)
      DIVFAC=1./DBLE(TEMP)
C     MULTIPLY DM BY DIVFAC
```

```
      CALL SKLMUL(DM,DM,DIVFAC,NDENO,NDENO)
C     ACCUMULATE INTO TRMAT
      CALL MATADD(TRMAT,TRMAT,DM,NDENO,NDENO)
 10   CONTINUE
C     NOW RAISE TO POWER (TO CANCEL TSPRME EFFECT ABOVE)
C     USE DM AND FM FOR TEMP. STORAGE
      DO 20 I=1,4
      CALL MATMUL(FM,TRMAT,TRMAT,NDENO,NDENO,NDENO)
C     NOW REPEAT TO GET TO CORRECT POWER
 20   CALL MATMUL(TRMAT,FM,FM,NDENO,NDENO,NDENO)
C     TRANSITION MATRIX NOW STORED IN TRMAT
      RETURN
      END

      SUBROUTINE THETAS(THETA,P,TRMAT,NDENOM,NNUMER,NPRAM,C,AINV)
C     THIS ROUTINE COMPUTES THETA=INV(A)*(TRMAT-I)
      DIMENSION THETA(NDENOM,NDENOM),P(NPRAM),TRMAT(NDENOM,NDENOM)
      DIMENSION C(NDENOM,NDENOM),AINV(NDENOM,NDENOM)
      DOUBLE PRECISION THETA,P,TRMAT,AINV,C
      NDENO=NDENOM
      DO 5 I=1,NDENOM
      DO 5 J=1,NDENOM
      C(I,J)=TRMAT(I,J)
      IF(I.EQ.J) C(I,J)=C(I,J)-1.
C     SET UP AINV FROM P-VECTOR
      AINV(I,J)=0.
      IM=I-1
      IF(IM.EQ.J) AINV(I,J)=1.
      NPICK=NNUMER+1
      NSEL=NPICK+J+1
      IF(J.EQ.NDENOM) GO TO 5
      IF(I.EQ.1) AINV(I,J)=-P(NSEL)/P(NPICK+1)
 5    CONTINUE
      AINV(1,NDENOM)=1./P(NPICK+1)
C     NOW COMPUTE THETA
      CALL MATMUL(THETA,AINV,C,NDENO,NDENO,NDENO)
      RETURN
      END
```

```
      SUBROUTINE VECPRP(XHAT,BIGY,X1K,X2K,X1KP1,X2KP1,TRMAT,THETA,ZETA,U
     +,YM,YO,TSTEP,XII,P,NNUMER,NDENOM,NDATA)
C     THIS ROUTINE PROPAGATES INITIAL STATE VECTOR THROUGH
C     ENTIRE INPUT FORCING FUNCTION
      DIMENSION XHAT(NDATA,NDATA),BIGY(16),X1K(8),X2K(8),X1KP1(8)
      DIMENSION X2KP1(8),TRMAT(NDENOM,NDENOM),THETA(NDENOM,NDENOM)
      DIMENSION ZETA(NDENOM,NDENOM),U(17),YM(17),YO(17),P(12)
      DIMENSION XII(16)
      DOUBLE PRECISION XHAT,BIGY,X1K,X2K,X1KP1,X2KP1
      DOUBLE PRECISION TRMAT,THETA,ZETA,U,YM,YO,P,XII
      DOUBLE PRECISION TSTEP,DU,DY
      JXK=1
C     INITIALIZE VECTORS FIRST
      DO 35 I=1,NDENOM
      X1K(I)=0.
      X1KP1(I)=0.
      X2K(I)=0.
      X2KP1(I)=0.
 35   CONTINUE
      DO 60 K=1,NDATA
C     COMPUTE STATE VECTOR FOR H(S) SUB-I
C     FIRST GET TRANSIENT COMPONET
      CALL MATMUL(X1KP1,TRMAT,X1K,NDENOM,NDENOM,JXK)
C     NOTE:X1KP1=X1K UPDATED ONE STEP BY STATE TRANSITION MATRIX
C     NOW ADD FORCING TERM
      INUMP1=NNUMER+1
      DO 40 I=1,NDENOM
 61   X1KP1(I)=X1KP1(I)+THETA(I,NDENOM)*U(K)
      DU=U(K+1)-U(K)
      DU=DU/TSTEP
 64   X1KP1(I)=X1KP1(I)+ZETA(I,NDENOM)*DU
      XHAT(K,I)=X1K(I)
C     NOW SAVE X1KP1 FOR NEXT PASS THROUGH(K+1)
      X1K(I)=X1KP1(I)
 40   CONTINUE
C     ***********NOW COMPUTE STATE FOR H(S) SUB-II
      CALL MATMUL(X2KP1,TRMAT,X2K,NDENOM,NDENOM,JXK)
```

```
      XII(K)=0.
      BIGY(K)=0.
C     XII(K) IS USED TO TEMPORAIRLY HOLD (X-SUB-II(TRANSPOSED)*PBACK)
      DO 50 I=1,NDENOM
      X2KP1(I)=X2KP1(I)+THETA(I,NDENOM)*YM(K)
      DY=YM(K+1)-YM(K)
      DY=DY/TSTEP
      X2KP1(I)=X2KP1(I)+ZETA(I,NDENOM)*DY
      I2=NNUMER+I+1
      XHAT(K,I2)=X2K(I)
      XII(K)=XII(K)+X2K(I)*P(I2)
      X2K(I)=X2KP1(I)
 50   CONTINUE
      BIGY(K)=YO(K)+XII(K)
 60   CONTINUE
      RETURN
      END
```

```
      SUBROUTINE WAVEHT(SWH,AT2,AT,A,P,TSTEP,NOINT,TRMAT,THETA,D2,ZETA,D
     +1,D3,PROB,NNUMER,NDENOM,NPRAM,NDATA)
      DIMENSION P(NPRAM),TRMAT(NDENOM,NDENOM),THETA(NDENOM,NDENOM)
      DIMENSION PROB(NDATA),D1(NDENOM,NDENOM),D2(NDENOM,NDENOM)
      DIMENSION D3(NDENOM,NDENOM),ZETA(NDENOM,NDENOM)
      DOUBLE PRECISION P,TRMAT,THETA,D1,D2,D3,ZETA
      DOUBLE PRECISION SWH,AT2,AT,A,TSTEP,BT,T,PARM
C     THIS ROUTINE COMPUTES:
C     SWH=H1/3=SIGNIFICANT WAVE HEIGHT
C     AT2=E(T**2),E=EXPECTATION
C     AT =E(T)
C     A=INTEGRAL(H(T)=AREA UNDER PRØB.CURVE
      X=FLOAT(NOINT-4)
      BT=TSTEP*DBLE(X)
      T=BT/16.
C     COMPUTE TRMAT
      CALL MATEXP(TRMAT,P,T,NDENOM,NNUMER,NPRAM,D1,D2,D3)
C     RAISE RESULT TO 16TH POWER
      DO 5 I=1,2
      CALL MATMUL(D1,TRMAT,TRMAT,NDENOM,NDENOM,NDENOM)
 5    CALL MATMUL(TRMAT,D1,D1,NDENOM,NDENOM,NDENOM)
C     NOW COMPUTE THETA
      CALL THETAS(THETA,P,TRMAT,NDENOM,NNUMER,NPRAM,D1,D2)
C     NOTE:A(**-1) IS IN D2 FROM LAST CALL
C     COMPUTE A:
      NNUMP1=NNUMER+1
      A=Ø.
      DO 1Ø I=1,NNUMP1
 1Ø   A=A+P(I)*THETA(I,NDENOM)
C     COMPUTE AT
      CALL SKLMUL(D1,TRMAT,BT,NDENOM,NDENOM)
      CALL SKLMUL(D3,THETA,-1.,NDENOM,NDENOM)
      CALL MATADD(D1,D1,D3,NDENOM,NDENOM)
C     RECALL A**(-1) IS STORED IN D2 FROM THETAS CALL ABOVE
      CALL MATMUL(D3,D2,D1,NDENOM,NDENOM,NDENOM)
      AT=Ø.
```

```
      DO 20 I=1,NNUMP1
   20 AT=AT+P(I)*D3(I,NDENOM)
    C COMPUTE AT2:
      PARM=BT*BT
      CALL SKLMUL(D1,TRMAT,PARM,NDENOM,NDENOM)
      PARM=-2.*BT
      CALL SKLMUL(D3,D2,PARM,NDENOM,NDENOM)
      CALL MATMUL(ZETA,D3,TRMAT,NDENOM,NDENOM,NDENOM)
      CALL MATADD(D1,D1,ZETA,NDENOM,NDENOM)
      CALL MATMUL(ZETA,D2,THETA,NDENOM,NDENOM,NDENOM)
      CALL SKLMUL(ZETA,ZETA,2.,NDENOM,NDENOM)
      CALL MATADD(D1,ZETA,D1,NDENOM,NDENOM)
      CALL MATMUL(D3,D2,D1,NDENOM,NDENOM,NDENOM)
      AT2=0.
      DO 30 I=1,NNUMP1
   30 AT2=AT2+P(I)*D3(I,NDENOM)
      SWH=AT2/A-(AT/A)*(AT/A)
      IF(SWH.LT. 0.) GO TO 80
      SWH=DSQRT(SWH)
      GO TO 90
   80 SWH=DABS(SWH)
      SWH=-DSQRT(SWH)
   90 SWH=6.25*SWH/TSTEP
    * SWH=DABS(SWH)*SWH
      IF(SWH.LT. 0.)  SWH=-DSQRT(DABS(SWH))
      IF(SWH.GE. 0.)  SWH=DSQRT(SWH)
      SWH=0.6*SWH
    C COMPUTE PROB. DENSITY CURVE
    C COMPUTE TRMAT FOR PROB. COMPUTATION
      CALL MATEXP(TRMAT,P,TSTEP,NDENOM,NNUMER,NPRAM,D1,D2,D3)
      DO 40 I=1,NDENOM
      DO 40 J=1,NDENOM
      D1(I,J)=0.
```

```
40      IF(I.EQ.J) D1(I,J)=1.
        DO 50 K=1,NDATA
        CALL MATMUL(D3,D1,TRMAT,NDENOM,NDENOM,NDENOM)
        DO 60 I=1,NDENOM
        DO 60 J=1,NDENOM
60      D1(I,J)=D3(I,J)
        PROB(K)=0.
        DO 70 I=1,NNUMP1
        PARM=P(I)*D1(I,NDENOM)
70      PROB(K)=PROB(K)+SNGL(PARM)
        PROB(K)=PROB(K)/SNGL(A)
50      CONTINUE
        RETURN
        END
*
```

```
TT:=DK1:DMINV.FOR
      SUBROUTINE MATINV(NR,A1,EPS1,EPS3,B1)
C     MATINV COMPUTES THE INVERSE OF MATRIX A USING CROUT REDUCTION
C     ANSWER RETURNED IN B
C     EPS1=TOLERABLE ERROR OF RESIDUES IN SUBROUTINE CROUT
C     EPS3=TOL. RELATIVE ERROR IN RESIDUES IN SUBROUTINE CROUT
C     NR=NO. OF ROWS IN MATRIX A
      DIMENSION A(13,13),B(13,13),C(13,13),X(12)
      DIMENSION A1(NR,NR),B1(NR,NR)
      DOUBLE PRECISION A1,EPS1,EPS3,B1,A,B,C,X
      DO 1 I=1,NR
      DO 1 J=1,NR
1     A(I,J)=A1(I,J)
      NSTOP=0
      DO 2 J=1,NR
      DO 2 K=1,NR
2     C(J,K)=A(J,K)
      NR1=NR+1
      DO 6 K=1,NR
      DO 4 J=1,NR
4     C(J,NR1)=0.
      C(K,NR1)=1.
      CALL CROUT(NR,C,EPS1,EPS3,X,NSTOP)
      IF (NSTOP.EQ.2) GO TO 7
      DO 5 J=1,NR
5     B(J,K)=X(J)
6     CONTINUE
      GO TO 10
7     WRITE(7,500)
500   FORMAT(////'SINGULAR MATRIX ENCOUNTERED')
10    CONTINUE
      DO 20 I=1,NR
      DO 20 J=1,NR
```

```
 20      B1(I,J)=B(I,J)
         RETURN
         END
         SUBROUTINE CROUT(NR,B,EPS1,EPS3,T,NSTOP)
C        NR,B,EPS1,EPS3 ARE NOT CHANGED BY THIS PROG.
C        CROUT SOLVES FOLLOWING MATRIX EQ.:B(NR,NR)*B(NR+1)
C        B(NR,NR) IS TO BE INVERTED
C        B(NR+1) IS A KNOWN VECTOR
C        SEE MATINV FOR DEFINITION OF EPS1,EPS3
C        INVERTED MATRIX IS RETURNED IN VARIABLE T
C        NSTOP IS FLAG FOR ZERO PIVOT ELEMENT
         DIMENSION A(12,12),B(13,13),X(12),T(12),R(12),C(13)
         DOUBLE PRECISION A,B,X,T,R,C,EPS1,EPS3,Q,XX,RR
         DOUBLE PRECISION TEST
 501     FORMAT(///'MATRIX CANNOT BE INVERTED - SINGULAR' )
         KP=0
         NSTOP=0
         NC=NR+1
         NGO=NC+1
         IF(NR.LE.3) NGO=6
         NN=NR-1
         DO 2 I=1,NR
         R(I)=B(I,NC)
 2       T(I)=0
 3       DO 4 I=1,NR
         DO 4 J=1,NR
 4       A(I,J)=B(I,J)
         DO 5 N=1,NR
         A(N,NC)=R(N)
         C(N)=A(1,N)
 5       CONTINUE
         C(NC)=A(1,NC)
         DO 9 L=1,NN
         LO=L+1
         Q=DABS(A(1,1))-DABS(A(LO,1))
         IF(Q.GT. 0.) GO TO 9
```

```
      IS=1
      IF(A(1,1).EQ. Ø.) GO TO 84
      DO 8 N=1,NC
      A(1,N)=A(LO,N)
      A(LO,N)=C(N)
8     C(N)=A(1,N)
9     CONTINUE
      DO 11 I=1,NR
11    A(1,I+1)=A(1,I+1)/A(1,1)
      DO 5Ø I=1,NN
      IS=I+1
      NI=NR-I
      DO 3Ø K=1,NI
      KI=K+I
      DO 3Ø L=1,I
3Ø    A(KI,IS)=A(KI,IS)-A(KI,L)*A(L,IS)
      DO 31 N=1,NC
31    C(N)=A(IS,N)
      LR=NR-IS
      IF(LR.LE.Ø) GO TO 39
      DO 38 L=1,LR
      LX=IS+L
      Q=DABS(A(IS,IS))-DABS(A(LX,IS))
      IF(Q.GE. Ø.) GO TO 38
      DO 35 N=1,NC
      A(IS,N)=A(LX,N)
      A(LX,N)=C(N)
35    C(N)=A(IS,N)
38    CONTINUE
39    CONTINUE
      IF(A(IS,IS).EQ. Ø.) GO TO 84
      DO 45 J=1,NI
      DO 4Ø M=1,I
      IJ=IS+J
4Ø    A(IS,IJ)=A(IS,IJ)-A(IS,M)*A(M,IJ)
45    A(IS,IJ)=A(IS,IJ)/A(IS,IS)
```

```
50      CONTINUE
        X(NR)=A(NR,NC)
        DO 60 KK=1,NN
        LL=NR-KK
        XX=0.
        II=NR-LL
        DO 55 JJ=1,II
        MM=LL+JJ
55      XX=XX+A(LL,MM)*X(MM)
60      X(LL)=A(LL,NC)-XX
        KTEST=0
        TEST=0.
        DO 68 I=1,NR
        T(I)=T(I)+X(I)
        RR=0.
        DO 64 J=1,NR
64      RR=RR+B(I,J)*X(J)
        R(I)=R(I)-RR
        IF(DABS(X(I)/T(I)).GE.EPS3) KTEST=1
        IF(ABS(R(I)).GE.EPS1) TEST=1
68      CONTINUE
        KP=KP+1
        IF(TEST.LE. 0. .AND.KTEST.EQ.0 .OR.KP.GT.NGO) GO TO 86
        GO TO 3
84      NSTOP=2
        WRITE(7,501)
86      RETURN
        END
*
```

```
.R H13TST

 INPUT NNUM,NDENOM,NINP-FORMAT 3I3
  2  3 16

 INPUT GATE SAMPLES
    .00       .04       .05       .06       .08
    .14       .25       .32       .34       .50
    .68       .82       .85       .84       .85
    .84

 NORMALIZED GATE SAMPLES
-0.0375  0.0025  0.0125  0.0225  0.0425  0.1025  0.2125  0.2825
 0.3025  0.4625  0.6425  0.7825  0.8125  0.8025  0.8125  0.8025
 0.8058  0.8058  0.8058  0.8058  0.8058  0.8058  0.8058  0.8058
 0.8058

 H(S) PARAMETER VECTOR
   60.1756   -7.8903    1.1367   -72.4544   -36.7867    -5.7662
 PROB. DENSITY
    0.2029   -0.0048    0.3686    0.9564    1.4685    1.7331
    1.7007   -1.4187    0.9904    0.5327    0.1432   -0.1195
   -0.2396   -0.2372   -0.1539   -0.0375    0.0708    0.1439
    0.1716    0.1577    0.1155    0.0616    0.0112   -0.0254
   -0.0438
 SWH=,AT2=,AT=,A=:
   9.06788551    0.36741901    0.51712578    0.84016753


RESIDUALS
   -0.0375   -0.0067   -0.0118   -0.0179   -0.0221    0.0029
    0.0534    0.0290   -0.0726   -0.0438    0.0146    0.0575
    0.0225   -0.0205   -0.0179   -0.0190   -0.0005    0.0132
    0.0206    0.0201    0.0130    0.0017   -0.0105   -0.0210
   -0.0283


 SSQER=  0.02094843
STOP --
```

Appendix B

Plateau Region Sea State Behavior

Theoretical analyses have shown that the plateau region, which contains stationary statistics, is characterized by a covariance function which is dependent on sea state [1]. A series of covariance calculations were made under contrasting sea state conditions to test this sensitivity. Figure B.1 shows the results of these calculations; for the cases tested the change in covariance with sea state was found to be less than the uncertainty in the calculation. Based on this result, it is concluded that sea state effects are analogous to a linear system convolution concept only in terms of a mean waveform effect and not in terms of the signal correlation properties.

REFERENCES

1. Berger, T., "Satellite Altimetry Using Ocean Backscatter," IEEE Trans. on Ant. and Prop., Vol. AP 20, May, 1972.

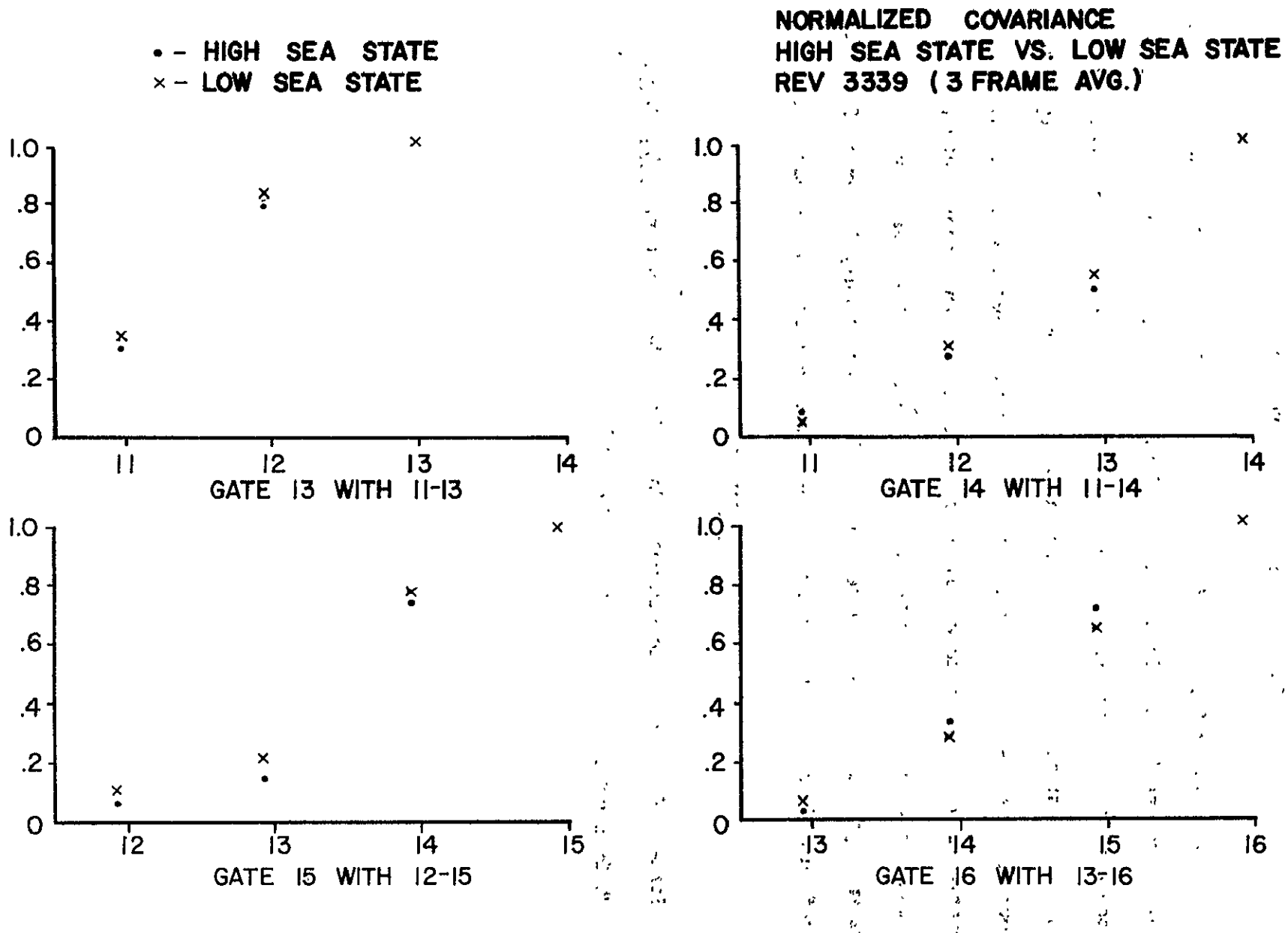

Figure B.1. Gate covariance for low and high sea state cases.

1. Report No.	2. Government Accession No.	3. Recipient's Catalog No.
NASA CR-156846		

4. Title and Subtitle	5. Report Date
AN INVESTIGATION OF THE OBSERVABILITY OF OCEAN-SURFACE PARAMETERS USING GEOS-3 BACKSCATTER DATA	October 1978
	6. Performing Organization Code

7. Author(s)	8. Performing Organization Report No.
L. S. Miller R. W. Priester	
	10. Work Unit No.
9 Performing Organization Name and Address Applied Science Associates, Inc. 105 East Chatham Street Apex, North Carolina 27502	11. Contract or Grant No. NAS6-2621
	13 Type of Report and Period Covered Final Report
12. Sponsoring Agency Name and Address National Aeronautics and Space Administration Wallops Flight Center Wallops Island, Virginia 23337	14. Sponsoring Agency Code

15. Supplementary Notes

16. Abstract

This report presents an evaluation of the degree to which ocean surface roughness can be synoptically observed through use of the information extracted from the GEOS-3 backscattered waveform data. Algorithms are given for use in estimating the radar sensed waveheight distribution or ocean-surface impulse response. Other factors discussed include comparisons between theoretical and experimental radar cross section values, sea state bias effects, spatial variability of significant waveheight data, and sensor-related considerations.

17. Key Words (Suggested by Author(s))		18 Distribution Statement
Remote sensing	Microwave backscatter	Unclassified - unlimited
Radar altimetry	GEOS-3	STAR Category - 17,35,42,46,48
Sea state		
Significant waveheight		

19. Security Classif. (of this report)	20 Security Classif. (of this page)	21. No. of Pages	22. Price*
Unclassified	Unclassified	109	

*For sale by the National Technical Information Service, Springfield, Virginia 22151